공학박사학위논문

Numerical Investigation on Steady/Unsteady Cavitating Flows and Hydrodynamic Forces Around a High-speed Underwater Vehicle With Control Fins

제어판이 장착된 고속 수중운동체 주변의 정상/비정상 공동유동 및 유체력에 대한 수치해석 연구

2021 년 2 월

서울대학교 대학원

기계항공공학부

최 요 한

Numerical Investigation on Steady/Unsteady Cavitating Flows and Hydrodynamic Forces Around a High-speed Underwater Vehicle With Control Fins

제어판이 장착된 고속 수중운동체 주변의 정상/비정상 공동유동 및 유체력에 대한 수치해석 연구

지도교수 김 종 암

이 논문을 공학박사 학위논문으로 제출함

2020 년 12 월

서울대학교 대학원

기계항공공학부

최 요 한

최요한의 공학박사 학위논문을 인준함

2020 년 12 월

위 원 장 : 이 관 중

부위원장 : 김 종 암

위 원 : 김 규 홍

위 원 : 이 신 형

위 원 : 안 병 권

Abstract

This work presents extensive numerical investigations on supercavitating flow behaviors around a high-speed underwater vehicle with control fins and the vehicle's hydrodynamic characteristics. Since the supercavitating flows include water, water vapor, and non-condensable air, the homogeneous mixture model is adopted to efficiently describe such multiphase flows. In order to validate the flow solver used in this work, some experiments of supercaviating flow are simulated in CFD. Firstly, ventilated cavitating flows around a cylinder with disc-shaped cavitator are considered, and then, ventilated cavitation in an unsteady gust flow is computed. The computational results show good agreement with the experiements. After validations, we conduct computations of supercavitating flows around a high-speed underwater vehicle with control fins, and investigate the surrounding flow physics and hydrodynamic characteristics of the vehicle. The computations are performed under various conditions such as freestream velocity, ventilation rate, and angle of attack. Overall, drag decreases as the cavity encloses a greater part of the control fins and the vehicle body. Even though the angle of attack is zero, the horizontal fins generate lift force aided by buoyancy. The computational results confirm that the cavitating flows lead to nonlinear characteristics of hydrodynamic forces compared with single-phase flows.

Keywords: Computational Fluid Dynamics (CFD), Multi-phase Flows, All-speed flows, AUSMPW+_N scheme, RoeM_N scheme, Natural cavitation, Ventilated cavitation, High-speed underwater vehicle, Hydrodynamic force

Student Number: 2014-30359

Contents

List of Figures

List of Tables

Chapter 1

Introduction

1.1 Supercavitating flows around high-speed underwater vehicle

Cavitation is a well-known phenomenon that occurs when the local liquid pressure falls sufficiently below the saturated vapor pressure. In many industrial areas, cavitation is sometimes regarded as a detrimental phenomenon because it causes performance deterioration and structural damage to hydraulic machineries. In contrast, for underwater vehicles traveling at very high speed, cavitation is considerably beneficial for drag reduction. When the cavity encloses the entire vehicle body, the drag can be reduced by as much as 90 % [1] since the body contacts with the cavity instead of water. In the case that the cavity covers the entire vehicle body, it is referred to as supercavitation. Cavitation can be divided into two different types: natural cavitation and ventilated cavitation. The former is a cavitation mentioned above and the latter is a sort of artificial cavitation made by injecting non-condensable gas (e.g. air, exhaust

gas, etc.) into the liquid flow field. Since an underwater vehicle needs very high speed to achieve natural supercavitation, ventilated supercavitation is used at relatively low speed to safely accelerate and achieve natural supercavitation. When the cavity covers too large area of the fins, the vehicle cannot have sufficient controllability due to the insignificant hydrodynamic force. In order to secure sufficient controllability, the fins should partially be exposed to water. Since the hydrodynamic force acting on the fins greatly depends on the area the cavity covers, it is significant to understand the cavitating flow around the control fins.

A lot of efforts in research on natural and ventilated supercavitation have been made both experimentally and numerically for decades. When it comes to experimental studies, Self and Ripken [2] conducted experiments on steady state axisymmetric supercavity around cylinder bodies with cone, hemisphere, and disk-type cavitators in 1955. They examined the cavity shapes by comparing the tendency of the results with some analytic solutions. Song [3] experimentally investigated two-dimensional pulsating ventilated supercavities. Wosnik *et al.* [4] measured ventilated cavitating flows and wake around a ventilated supercavitating vehicle model with disk-shaped cavitator. In this experiment, they reported the requirements of ventilation gas to achieve supercavitation for the body. Ventilated supercavitating flows depending on air-entrainment rate and Froude number were experimentally investigated by Karn and Rosiejka [5], Shao *et al.* [6], Ahn *et al.* [7], and Liu *et al.* [8]. Chung and Cho [9] conducted numerous experimental investigations of ventilated supercavitating flows around a moving body. In this experiment, they observed the cavity shape and the cavitating flow physics depending on Froude number, air-entrainment rate, cavitation number, and also measured drag acting on the test model.

Supercavitating flows have also been addressed numerically. One of the ap-

proaches is use of numerical model for predicting both natural and ventilated cavitating flows. Garabedian [10] developed an asymptotic formula for predicting axisymmetric supercavitating flows. Campbell and Hilborne [11] also developed some theoretical models for air entrainment depending on Froude number and cavitation number, and properly explained their experiemental data with the relation. Song [3] developed a numerical model for the pulsating supercavities. Recently, Kim and Ahn [12] introduced a potential-based panel method for predicting two-dimensional and axi-symmetric natural supercavitating flows with various shapes of cavitator. They also considered the viscous effect, and measured the drag forces acting on a supercavitating body by using the developed method. With the advances in computer science and technology, supercavitating flows have been dealt with by CFD. Kunz *et al.* [13, 14] conducted computations of natural and ventilated cavitating flows around a cylinder with different forebody such as ogive, hemishpere, and conical forebodies. They also computed supercavitating flows over an underwater vehicle [14]. Kinzel *et al.* [15] performed three-dimensional computations of ventilated supercavitating flows around a vehicle model, and showed the behavior of the injected air. Rashidi *et al.* [16] conducted both experimental and computational studies ventilated supercavitating flows around a cylinder body with a disk cavitator. In this study, they showed the detailed flow physics such as re-entrant jet and twin vortex flows and compared the computational results with the experiments.

So far, many studies on supercavitating flow around a high-speed underwater vehicle have been carried out numerically. Some of them focused on the pitching motion of supercavitating vehilces. When the cavity encloses the vehicle, it could descend and/or rotate due to the insufficient buoyant force lifting up the vehicle because the body (or fin) is exposed to the cavity, not water. And

then, the vehicle may suddenly experience substantial pitching moment since the afterbody contacts with water after descending and/or rotating. Thus, for supercavitating vehicles, the pitching motions are usually not avoidable due to the change in buoyant force. Kirschner *et al.* [17] presented control strategies for the highly-coupled nonlinear system including a supercavitating vehicle. In this work, a simple hydrodynamical model was implemented for dynamic simulation of the system. They reported that the behavior of the vehicle is dominated by the change in hydrodynamic forces as the afterbody alters between a planing and a non-planing condition. Yu *et al.* [18] conducted a numerical study of supercavitating vehicles with pitching motion. In this study, they investigated fixed frequency and free pitching motions to obtain some insight for designing supercavitating vehicles. Zou *et al.* [19] also dealt with the pitching motion of supercavitating vehicles. They conducted a further research in the maneuvering supercavity model with gravity, AOA, and inertial force effects. Based on the model, they developed numerical algorithm to simulate pitching motions of controllable vehicle in the high-speed motion. As an another major issue, cavitating flow physics and/or hydrodynamic characteristics of supercaviating vehicles have also been investigated numerically. Yuan and Xing [20] investigated the hydrodynamic forces acting on the after body of a supercavitating vehicle by using CFD. They analyzed the natural cavitating flow patterns and hydrodynamic forces depending on cavitation numbers and angles of attack. Cao *et al.* [21] conducted numerical investigations of pressure distribution inside a ventilated cavity. They used backward truncated cones as cavitators, injecting air behind them, and analyzed characteristics of ventilated supercavitating flow under various amounts of gas, Froude numbers, and cavitator sizes. Zou et al. [22] dealt with high speed ventilated supercavitating flows and gas loss mechanism. Near the cavity closure, the gas-liquid mediums collide and form foamy

cavity structures. Some of the foams leave the cavity due to the collision and thus the cavity loses the gas. In order to understand the gas-leakage mechanism, they established a gas-vapor-water multi-fluid model for ventilated supercavitating flows in CFD. Kim *et al.* [23] numerically investigated the evolution of the natural cavity and the variation of the drag force for an underwater vehicle with control fins, under various body speeds. They conducted steady RANS simulations for the real-scale vehicle that has the body shape like the Russian high-speed torpedo, Shkval.

Most of the previous researches have focused on the maneuverability (and/or controllability) of the vehicles. In spite of the many experimental and numerical studies on supercavitating vehicles mentioned above, numerical investigations on ventilated supercavitating flows and the hydrodynamic characteristics around an underwater vehicle with control fins have not been reported yet. As mentioned earlier, a supercavitating vehicle needs to reduce its drag by ventilated supercavitation at a relatively low speed, even though the vehicle is designed to operate at the natural supercavitating speed. Therefore, it is essential to deal with ventilated supercavitating flow around an underwater vehicle with control fins, and the hydrodynamic characteristics of the vehicle body and the fins.

1.2 Outline of thesis

The goal of this paper is to investigate and understand ventilated supercavitating flows around a high-speed underwater vehicle. To achieve this, we employ a homogeneous mixture model as the governing equations to properly compute water-vapor-air supercavitating flows. AUSMPW+_N and RoeM_N [24], the enhanced convective flux schemes for multiphase real-fluid flows at all speeds,

are also employed with proper system preconditioning. For validations of the flow solver used in this work, we conduct 3D steady and unsteady simulations of some experiments. Finally, we conduct 3D computations of cavitating flows around a high-speed underwater vehicle, and investigate the supercavitating flow physics and hydrodynamic characteristics of the vehicle. The computations are performed under various conditions such as freestream velocity, ventilation rate, and angle of attack.

This thesis is organized as follows. Following the introduction, brief descriptions of the governing equations, EOS, cavitation and turbulence model, and system preconditioning technique are given. Then, basic numerical methods including the enhanced and extended numerical flux schemes, and time integration methods are introduced. Based on these numerical methods, validation of the flow solver is presented with the computation results of three-dimensional steady/unsteady ventilated cavitating flows. Finally, three-dimensional steady/unsteady RANS simulations of a high-speed underwater vehicle are carried out under various flow conditions such as freestream speed, ventilation rate, and angles of attack. Extensive investigations on supercavitating flow physics and hydrodynamic characteristics of the vehicle are presented.

Chapter 2

Computational Modeling

2.1 Governing equations

The homogeneous mixture equations with mass fraction are adopted to describe multi-phase (water, vapor, air) flows. In homogeneous flow theory, the relative motion between phases is not considered; instead, a mixture is treated as a pseudo-fluid whose properties are some averages of each component in the flow. This approach is based on the view that it is sufficient to describe each phase as a continuum obtained from a microscopic description using a suitable averaging process. In this model, continuity, momentum, and energy equations are used to describe the fluid mixture, while a single continuity equation is used for vapor and non-condensable gas phases. To do this, the compressible Reynolds-averaged Navier-Stokes equations are cast in integral, Cartesian tensor form for an arbitrary control volume Ω with control surface $\partial\Omega$ as follows:

$$\frac{\partial}{\partial t}\int_{\Omega} \boldsymbol{W} d\Omega + \oint_{\partial\Omega} \left[(\boldsymbol{F_c} - \boldsymbol{F_v}) \cdot \boldsymbol{n}\right] dS = \int_{\Omega} \boldsymbol{D} d\Omega, \tag{2.1}$$

where $\boldsymbol{n} = (n_x, n_y, n_z)$ is an outward normal vector. The vector of conservative variables $\boldsymbol{W}$ and the convective flux tensor $\boldsymbol{F_c}$ are given by

$$\boldsymbol{W} = [\rho \quad \rho u \quad \rho v \quad \rho w \quad \rho E \quad \rho y_v \quad \rho y_g]^T , \tag{2.2}$$

$$\boldsymbol{F_c} = \begin{bmatrix} \rho u & \rho v & \rho w \\ \rho u^2 + p & \rho uv & \rho uw \\ \rho vu & \rho v^2 + p & \rho vw \\ \rho wu & \rho wv & \rho w^2 + p \\ \rho uH & \rho vH & \rho wH \\ \rho y_v u & \rho y_v v & \rho y_v w \\ \rho y_g u & \rho y_g v & \rho y_g w \end{bmatrix} . \tag{2.3}$$

Here, ρ, p, E, H, y_v, y_g and (u, v, w) are the mixture density, pressure, total energy, total enthalpy, mass fraction of vapor phase, mass fraction of gas phase and velocity vector, respectively. $\boldsymbol{F_v}$ indicates the viscous flux tensor,

$$\boldsymbol{F_v} = \begin{bmatrix} 0 & 0 & 0. \\ \tau_{xx} & \tau_{xy} & \tau_{xz} \\ \tau_{yx} & \tau_{yy} & \tau_{yz} \\ \tau_{zx} & \tau_{zy} & \tau_{zz} \\ \Phi_x & \Phi_y & \Phi_z \\ 0 & 0 & 0 \\ 0 & 0 & 0 \end{bmatrix} , \tag{2.4}$$

with

$$\Phi_x = u\tau_{xx} + v\tau_{xy} + w\tau_{xz} + q_x, \tag{2.5}$$

$$\Phi_y = u\tau_{yx} + v\tau_{yy} + w\tau_{yz} + q_y, \tag{2.6}$$

$$\Phi_z = u\tau_{zx} + v\tau_{zy} + w\tau_{zz} + q_z. \tag{2.7}$$

Here, τ is the viscous stress tensor. With the assumption of Newtonian fluid, the Stokes hypothesis is valid and τ can be expressed as follows:

$$\tau_{ij} = \mu \left(\frac{\partial u_i}{\partial x_j} + \frac{\partial u_j}{\partial x_i} - \frac{2}{3}\frac{\partial u_k}{\partial x_k}\delta_{ij} \right), \tag{2.8}$$

where μ is molecular viscosity coefficient. Based on the *eddy viscosity hypothesis* of Boussinesq, which assumes a linear relationship between the turbulent shear stress and the mean strain rate, the molecular viscosity μ in the viscous stress tensor (2.8) is replaced by the sum of a mixture laminar and a turbulent component

$$\mu = \mu_L + \mu_T. \tag{2.9}$$

Recall that q in Eqs. (2.5), (2.6), and (2.7) is the heat flux, which is defined by Fourier's law,

$$q_i = -k\frac{\partial T}{\partial x_i}, \tag{2.10}$$

where k is the thermal conductivity coefficient and T denotes the absolute static temperature. In analogy, the thermal conductivity coefficient in Eq. (2.10) is evaluated as

$$k = k_L + k_T = k_L + \left.\frac{\partial h}{\partial T}\right|_p \frac{\mu_T}{Pr_T} \tag{2.11}$$

where, h, T and Pr_T are the enthalpy, temperature and turbulent Prandtl number, respectively. The turbulent eddy viscosity μ_T should be evaluated based on a turbulence model.

The mixture density ρ is evaluated from the constitutive relation between each mass fraction, and defined as follows:

$$y_l + y_g + y_v = 1. \tag{2.12}$$

The subscripts (l, v, g) stand for the liquid, vapor, and non-condensable gas phases, respectively.

Finally, $\boldsymbol{D}$ in Eq. (2.1) is the phase change source term vector,

$$\boldsymbol{D} = \begin{pmatrix} 0 \\ 0 \\ 0 \\ 0 \\ 0 \\ \dot{m}_e - \dot{m}_c \\ 0 \end{pmatrix}, \tag{2.13}$$

where $\dot{m}_e$ and $\dot{m}_c$ are the evaporation and condensation source term that will be described in detail at a later section.

2.2 Equation of state (EOS)

The mixture density used in Eq. (2.1) can be expressed as the following form:

$$\frac{1}{\rho} = \frac{(1 - y_v - y_g)}{\check{\rho}_l} + \frac{y_v}{\check{\rho}_v} + \frac{y_g}{\check{\rho}_g}. \tag{2.14}$$

Here, $\check{q}$ indicates a quantity q defined by Amagat's rather than Dalton's law. The mixture density is then expressed in terms of volume fraction as follows:

$$\rho = (1 - \alpha_v - \alpha_g)\,\check{\rho}_l + \alpha_v \check{\rho}_v + \alpha_g \check{\rho}_g. \tag{2.15}$$

Note that the mass fraction and the volume fraction are related as

$$\rho y_g = \alpha_g \check{\rho}_g. \tag{2.16}$$

The mixture enthalpy h is then evaluated as

$$h = h_l\,(1 - y_g - y_v) + h_v y_v + h_g y_g. \tag{2.17}$$

In addition, the mixture laminar viscosity and heat conductivity are computed based on a local volume average,

$$\mu_L = (1 - \alpha_v - \alpha_g)\,\check{\mu}_l + \alpha_v \check{\mu}_v + \alpha_g \check{\mu}_g, \tag{2.18}$$

$$k_L = (1 - \alpha_v - \alpha_g)\,\check{k}_l + \alpha_v \check{k}_v + \alpha_g \check{k}_g. \tag{2.19}$$

The system is then closed with a proper EOS for the constituent phases. All thermodynamic properties of each phase are defined as a function of the local pressure and temperature as follows:

$$\check{\rho}_i = \check{\rho}_i\,(p, T)\,,\ h_i = h_i\,(p, T)\,,\ \check{\mu}_i = \check{\mu}_i\,(p, T)\,,\ \check{k}_i = \check{k}_i\,(p, T)\,. \tag{2.20}$$

The subscript i denotes a quantity (density, enthalpy, viscosity, heat conductivity) of the i-th phase. For each phase, we use various types of relations between the thermodynamic(or transport) properties (ρ, h, μ, k) and independent variables (p, T).

2.2.1 Ideal gas EOS

In this work, air is the non-condensable gas in the governing equations, and thus the ideal gas EOS is used:

$$\check{\rho}_g = \frac{\gamma_g p}{C_{p,g}(\gamma_g - 1)T}, \ h_g = C_{p,g}T, \tag{2.21}$$

where

$$\gamma_g = 1.4, \ C_{p,g} = 1003.64 \text{ J/(kg} \cdot \text{K)}. \tag{2.22}$$

The Sutherland law is used for viscosity calculation

$$\check{\mu}_g = 1.716 \times 10^{-5} \left(\frac{T}{T_0}\right)^{3/2} \frac{T_0 + S}{T + S}, \tag{2.23}$$

where $T_0 = 273$ K and $S = 110.56$ K. The heat conductivity is computed by

$$\check{k}_g = C_{p,g}\frac{\check{\mu}_g}{Pr}, \tag{2.24}$$

where $Pr = 0.72$ is used.

2.2.2 Stiffened gas EOS

The stiffened-gas model [25] can describe the liquid phase of water approximately. In this case, vapor (gas phase of water) is treated as ideal gas. The Stiffened-gas EOS is expressed as

$$\check{\rho}_l = \frac{\gamma_l(p - p_c)}{C_{p,l}(\gamma_l - 1)T}, \ h_l = C_{p,l}T, \tag{2.25}$$

where

$$\gamma_l = 2.8, \ C_{p,l} = 4186 \text{ J/(kg} \cdot \text{K)}, \ p_c = 8.5 \times 10^8 \text{ Pa}. \tag{2.26}$$

In addition, the following formulation is used to compute water viscosity,

$$ln\frac{\check{\mu}_l}{\check{\mu}_{l,0}} = a + b\left(\frac{T_0}{T}\right) + c\left(\frac{T_0}{T}\right)^2, \tag{2.27}$$

where $T_0 = 273$ K, $\check{\mu}_{l,0} = 0.001788$ kg/ (m · s), $a = -1.704$, $b = -5.306$ and $c = 7.003$, respectively. The heat conductivity is computed by

$$\check{k}_l = C_{p,l}\frac{\check{\mu}_l}{Pr}, \tag{2.28}$$

where $Pr = 7$ is used.

2.2.3 IAPWS97 formulation

In the presence of phase change phenomenon (between the gas and the liquid phases), both ideal gas and stiffened EOS are not appropriate since these EOSs do not provide accurate values near the saturated line. In order to properly describe the phase change phenomenon, the IAPWS97 formulation [26] is adopted for both liquid and gas phases of water. The basic equations are expressed using the specific Gibbs free energy, g, in terms of pressure and temperature. For the liquid phase, g is given by

$$\frac{g_l}{RT} = \sum_{i=1}^{34} n_i \left(7.1 - \frac{p}{p_l^*}\right)^{I_i} \left(\frac{T_l^*}{T} - 1.222\right)^{J_i}, \tag{2.29}$$

where $P_l^* = 16.53$ MPa, $T_l^* = 1386$ K and $R = 0.461526$ kJ · kg^{-1} · K^{-1}. The coefficients n_i and exponents I_i and J_j of Eq. (2.29) are listed in Table 2.1.

Here, Eq. (2.29) covers liquid region defined by the following range of temperature and pressure:

$$273.15 \text{ K} \leq T \leq 623.15 \text{ K} \qquad p_s(T) \leq p \leq 100 \text{ MPa}. \tag{2.30}$$

Table 2.1: Coefficients and exponents of the Gibbs free energy in Eq. (2.29)

i	I_i	J_i	n_i	i	I_i	J_i	n_i
1	0	-2	0.14632971213167	18	2	3	$-0.44141845330846\times10^{-5}$
2	0	-1	-0.84548187169114	19	2	17	$-0.72694996297594\times10^{-15}$
3	0	0	$-0.37563603672040\times10^{1}$	20	3	-4	$-0.31679644845054\times10^{-4}$
4	0	1	$0.33855169168385\times10^{1}$	21	3	0	$-0.28270797985312\times10^{-5}$
5	0	2	-0.95791963387872	22	3	6	$-0.85205128120103\times10^{-9}$
6	0	3	0.15772038513228	23	4	-5	$-0.22425281908000\times10^{-5}$
7	0	4	$-0.16616417199501\times10^{-1}$	24	4	-2	$-0.65171222895601\times10^{-6}$
8	0	5	$0.81214629983568\times10^{-3}$	25	4	10	$-0.14341729937924\times10^{-12}$
9	1	-9	$0.28319080123804\times10^{-3}$	26	5	-8	$-0.40516996860117\times10^{-6}$
10	1	-7	$-0.60706301565874\times10^{-3}$	27	8	-11	$-0.12734301741641\times10^{-8}$
11	1	-1	$-0.18990068218419\times10^{-1}$	28	8	-6	$-0.17424871230634\times10^{-9}$
12	1	0	$-0.32529748770505\times10^{-1}$	29	21	-29	$-0.68762131295531\times10^{-18}$
13	1	1	$-0.21841717175414\times10^{-1}$	30	23	-31	$0.14478307828521\times10^{-19}$
14	1	3	$-0.52838357969930\times10^{-4}$	31	29	-38	$0.26335781662795\times10^{-22}$
15	2	-3	$-0.47184321073267\times10^{-3}$	32	30	-39	$-0.11947622640071\times10^{-22}$
16	2	0	$-0.30001780793026\times10^{-3}$	33	31	-40	$0.18228094581404\times10^{-23}$
17	2	1	$0.47661393906987\times10^{-4}$	34	32	-41	$-0.93537087292458\times10^{-25}$

Table 2.2: Coefficients and exponents of the ideal-gas part of the Gibbs free energy in Eq. (2.31)

i	J_i^0	n_i^0	i	J_i^0	n_i^0
1^a	0	$-0.96927686500217\times10^1$	6	-2	$0.14240819171444\times10^1$
2^a	1	$0.10086655968018\times10^2$	7	-1	$-0.43839511319450\times10^1$
3	-5	$-0.56087911283020\times10^{-2}$	8	2	-0.28408632460772
4	-4	$0.71452738081455\times10^{-1}$	9	3	$0.21268463753307\times10^{-1}$
5	-3	-0.40710498223928			

[a] If Eq. (2.37) is used, instead of the values for n_1^0 and n_2^0 given above, the following values for these coefficients must be used: $n_1^0 = -0.96937268393049 \times 10^1$, $n_2^0 = 0.10087275970096 \times 10^2$.

Eq. (2.29) yields reasonable values not only in the stable single-phase liquid region, but also in the metastable superheated-liquid region close to the saturated liquid line.

For the vapor phases, g is given by

$$\frac{g_v}{RT} = \ln\frac{p}{p_v^*} + \sum_{i=1}^{9} n_i^0 \left(\frac{T_v^*}{T}\right)^{J_i^0} + \sum_{i=1}^{43} n_i^v \left(\frac{p}{p_v^*}\right)^{I_i^v} \left(\frac{T_v^*}{T} - 0.5\right)^{J_i^v}, \tag{2.31}$$

where $P_v^* = 1$ MPa, $T_v^* = 540$ K and $R = 0.461526$ kJ $\cdot$ kg^{-1} $\cdot$ K^{-1}. In Eq. (2.31), the values of n_i^0 and J_i^0 are listed in Table 2.2, and the values of n_i^v, I_i^v, and J_i^v are in Table 2.3.

Here, Eq. (2.31) covers vapor region defined by the following range of temperature and pressure:

$$\begin{aligned} &273.15\ \mathrm{K} \le T \le 623.15\ \mathrm{K} && 0 < p \le p_s(T), \\ &623.15\ \mathrm{K} < T \le 863.15\ \mathrm{K} && 0 < p \le p_{b23}(T), \\ &863.15\ \mathrm{K} < T \le 1073.15\ \mathrm{K} && 0 < p \le 100\ \mathrm{MPa}. \end{aligned} \tag{2.32}$$

Table 2.3: Coefficients and exponents of the residual part of the Gibbs free energy in Eq. (2.31)

i	I_i^v	J_i^v	n_i^v	i	I_i^v	J_i^v	n_i^v
1	1	0	$-0.17731742473213\times10^{-2}$	23	7	0	$-0.59059564324270\times10^{-17}$
2	1	1	$-0.17834862292358\times10^{-1}$	24	7	11	$-0.12621808899101\times10^{-5}$
3	1	2	$-0.45996013696365\times10^{-1}$	25	7	25	$-0.38946842435739\times10^{-1}$
4	1	3	$-0.57581259083432\times10^{-1}$	26	8	8	$0.11256211360459\times10^{-10}$
5	1	6	$-0.50325278727930\times10^{-1}$	27	8	36	$-0.82311340897998\times10^{1}$
6	2	1	$-0.33032641670203\times10^{-4}$	28	9	13	$0.19809712802088\times10^{-7}$
7	0	4	$-0.16616417199501\times10^{-1}$	29	10	4	$0.10406965210174\times10^{-18}$
8	2	4	$-0.39392777243355\times10^{-2}$	30	10	10	$-0.10234747095929\times10^{-12}$
9	2	7	$-0.43797295650573\times10^{-1}$	31	10	14	$-0.10018179379511\times10^{-8}$
10	1	36	$-0.26674547914087\times10^{-4}$	32	16	29	$-0.80882908646985\times10^{-10}$
11	3	0	$0.20481737692309\times10^{-7}$	33	16	50	0.10693031879409
12	3	1	$0.43870667284435\times10^{-6}$	34	18	57	-0.33662250574171
13	3	3	$-0.32277677238570\times10^{-4}$	35	20	20	$0.89185845355421\times10^{-24}$
14	3	6	$-0.15033924542148\times10^{-2}$	36	20	35	$0.30629316876232\times10^{-12}$
15	3	35	$-0.40668253562659\times10^{-1}$	37	20	48	$-0.42002467698208\times10^{-5}$
16	4	1	$-0.78847309559367\times10^{-9}$	38	21	21	$-0.59056029685639\times10^{-25}$
17	4	2	$0.12790717852285\times10^{-7}$	39	22	53	$0.37826947613457\times10^{-5}$
18	4	3	$0.48225372718507\times10^{-6}$	40	23	39	$-0.12768608934681\times10^{-14}$
19	5	7	$0.22922076337661\times10^{-5}$	41	24	26	$0.73087610595061\times10^{-28}$
20	6	3	$-0.16714766451061\times10^{-10}$	42	24	40	$0.55414715350778\times10^{-16}$
21	6	16	$-0.21171472321355\times10^{-2}$	43	24	58	$-0.94369707241210\times10^{-6}$
22	6	35	$-0.23895741934104\times10^{2}$				

Table 2.4: Coefficients for the dimensionless saturation pressure (Eqs. (2.34) and (2.35))

i	n_i^s	i	n_i^s
1	$0.11670521452767\times10^4$	6	$0.14915108613530\times10^2$
2	$-0.72421316703206\times10^6$	7	$-0.48232657361591\times10^4$
3	$-0.17073846940092\times10^2$	8	$0.40511340542057\times10^6$
4	$0.12020824702470\times10^5$	9	-0.23855557567849
5	$-0.32325550322333\times10^7$	10	$0.65017534844798\times10^3$

In Eqs. (2.30) and (2.32), the saturation pressure, $p_s(T)$ is given by

$$\frac{p_s(T)}{p^*} = \left[\frac{2C}{-B + (B^2 - 4AC)^{1/2}}\right]^4, \tag{2.33}$$

where $p^* = 1$ MPa and

$$\begin{aligned} A &= \Theta^2 + n_1^s\Theta + n_2^s \\ B &= n_3^s\Theta^2 + n_4^s\Theta + n_5^s \\ C &= n_6^s\Theta^2 + n_7^s\Theta + n_8^s \end{aligned} \tag{2.34}$$

with Θ according to

$$\Theta = T + \frac{n_9^s}{T - n_{10}^s}. \tag{2.35}$$

The coefficients n_i of Eqs. (2.34) and (2.35) are listed in Table 2.4.

In Eq. (2.32), $p_{b23}(T)$ is a simple quadratic pressure-temperature relation, so-called B23-equation:

$$\frac{p_{b23}(T)}{p^*} = n_1^{b23} + n_2^{b23}\frac{T}{T^*} + n_3^{b23}\frac{T}{T^*}, \tag{2.36}$$

Table 2.5: Coefficients of the B23-equation (Eq. (2.36))

i	n_i^{b23}
1	$0.34805185628969\times10^{3}$
2	$-0.11671859879975\times10^{1}$
3	$0.10192970039326\times10^{-2}$

where $T^* = 1$ K. The coefficients n_1^{b23} to n_3^{b23} of Eq. (2.36) are listed in Table 2.5.

As Eq. (2.29), Eq. (2.31) also yields reasonable values both in the stable single-phase vapor region and in the metastable-vapor region for pressure above 10 Mpa. However, Eq. (2.31) is not valid in the metastable-vapor region at pressures $p \leq 10$ MPa; for this part of the metastable-vapor region see following relation:

$$\frac{g_v}{RT} = \ln\frac{p}{p_v^*} + \sum_{i=1}^{9} n_i^0 \left(\frac{T_v^*}{T}\right)^{J_i^0} + \sum_{i=1}^{13} n_i^v \left(\frac{p}{p_v^*}\right)^{I_i^v} \left(\frac{T_v^*}{T} - 0.5\right)^{J_i^v}. \tag{2.37}$$

In the above equation, first and second terms are identical with Eq. (2.31) except for the values of the two coefficients n_1^0 and n_2^0, see Table 2.2. The coefficients n_i and exponents I_i^v and J_i^v of Eq. 2.37 are listed in Table 2.6.

The relations between the derivatives of the specific Gibbs free energy and the relevant thermodynamic properties are

$$\check{\rho}_l = 1/\left.\frac{\partial g_l}{\partial p}\right|_T, \quad \check{\rho}_v = 1/\left.\frac{\partial g_v}{\partial p}\right|_T, \quad h_l = g_l - T\left.\frac{\partial g_l}{\partial T}\right|_p, \quad h_v = g_v - T\left.\frac{\partial g_v}{\partial T}\right|_p. \tag{2.38}$$

For the viscosity and heat conductivity, we use the IAPS formulation [27].

Table 2.6: Coefficients and exponents of the residual part γ^r of the Gibbs free energy for the metastable-vapor region (Eq. (2.37))

i	I_i^v	J_i^v	n_i^v	i	I_i^v	J_i^v	n_i^v
1	1	0	$-0.73362260186506\times10^{-2}$	8	3	4	$-0.63498037657313\times10^{-2}$
2	1	2	$-0.88223831943146\times10^{-1}$	9	3	16	$-0.86043093028588\times10^{-1}$
3	1	5	$-0.72334555213245\times10^{-1}$	10	4	7	$0.75321581522770\times10^{-2}$
4	1	11	$-0.40813178534455\times10^{-2}$	11	4	10	$-0.79238375446139\times10^{-2}$
5	2	1	$0.20097803380207\times10^{-2}$	12	5	9	$-0.22888160778447\times10^{-3}$
6	2	7	$-0.53045921898642\times10^{-1}$	13	5	10	$-0.26456501482810\times10^{-2}$
7	2	16	$-0.76190409086970\times10^{-2}$				

2.3 Cavitation model

Physically, the cavitation process is governed by thermodynamics and kinetics of the phase change process. The liquid-vapor conversion associated with the cavitation process is modeled through $\dot{m}_e$ and $\dot{m}_c$ terms in Eq. (2.13), which respectively represent condensation and evaporation. The term $\dot{m}_e$ is the evaporation rate of vapor being generated from liquid at a region in which the local pressure is less than the vapor pressure. Conversely, $\dot{m}_c$ is the condensation rate for reconversion of vapor back to liquid regions in which the local pressure exceeds the vapor pressure. The particular form of these phase transformation rates forms the basis of the cavitation model. Here, the model proposed by Merkle [28] is employed. The Merkle cavitation model was derived primarily based on dimensional arguments for large-bubble clusters instead of individual bubbles. Consequently, the source and sink terms for the Merkle are directly related to the pressure difference, $p - p_v$.

2.4 Turbulence Model

Turbulence effect can be described by computing the eddy viscosity μ_T. Hence, proper turbulence model to evaluate the eddy viscosity is essential for predicting turbulent flows. In this work, from the large variety of first-order closure models, we chose $K-\omega$ SST (Shear-Stress Transport) two-equation model proposed by Menter [29, 30].

2.4.1 SST two-equation model of Menter

The $K-\omega$ SST model of Menter [29, 30] merges the $K-\omega$ model of Wilcox [31], with a high Reynolds number $K-\epsilon$ model (transformed in the $K-\omega$ formulation) to combine the positive features of both models. In this model, the $K-\omega$ approach is employed in the inner part of the boundary layer since the model needs no damping function. This leads, for similar accuracy, to significantly higher numerical stability in comparison to the $K-\epsilon$ model. Furthermore, the $K-\omega$ model is also utilised in logarithmic layer. On the other hand, the $K-\epsilon$ model is employed in the wake region of the boundary layer because the $K-\omega$ model is strongly sensitive to the freestream value of ω [32]. The $K-\epsilon$ approach is also used in free shear layers such as wakes, jets, and mixing layers.

The transport equations for the turbulent kinetic energy and the specific dissipation of turbulence read in integral form for a control volume Ω with a surface element $\mathrm{d}S$:

$$\frac{\partial}{\partial t}\int_{\Omega} \boldsymbol{W_T} d\Omega + \oint_{\partial\Omega} \left[(\boldsymbol{F_{c,T}} - \boldsymbol{F_{v,T}}) \cdot \boldsymbol{n}\right] dS = \int_{\Omega} \boldsymbol{D_T} d\Omega. \tag{2.39}$$

The vector of the conservative variables takes the form

$$\boldsymbol{W_T} = \begin{bmatrix} \rho K \\ \rho\omega \end{bmatrix}. \tag{2.40}$$

The convective flux tensor is defined

$$\boldsymbol{F_{c,T}} = \begin{bmatrix} \rho K u & \rho K v & \rho K w \\ \rho\omega u & \rho\omega v & \rho\omega w \end{bmatrix}. \tag{2.41}$$

The tensor of the viscous flux is given by

$$\boldsymbol{F_{v,T}} = \begin{bmatrix} (\mu_L + \sigma_K \mu_T)\frac{\partial K}{\partial x} & (\mu_L + \sigma_K \mu_T)\frac{\partial K}{\partial y} & (\mu_L + \sigma_K \mu_T)\frac{\partial K}{\partial z} \\ (\mu_L + \sigma_\omega \mu_T)\frac{\partial \omega}{\partial x} & (\mu_L + \sigma_\omega \mu_T)\frac{\partial \omega}{\partial y} & (\mu_L + \sigma_\omega \mu_T)\frac{\partial \omega}{\partial z} \end{bmatrix}. \tag{2.42}$$

The source term is evaluated from

$$\boldsymbol{D_T} = \begin{bmatrix} \tilde{P} - \beta_T^* \rho\omega K \\ \frac{C_\omega \rho}{\mu_T}\tilde{P} - \beta_T \rho\omega^2 + 2\left(1 - f_1\right)\frac{\rho\sigma_{\omega 2}}{\omega}\frac{\partial K}{\partial x_i}\frac{\partial \omega}{\partial x_i} \end{bmatrix}. \tag{2.43}$$

A production limiter is used in the SST model to prevent the build-up of turbulence in stagnation regions:

$$\tilde{P} = \min\left(\tau_{ij}^F S_{ij}, 10\beta_T^* \rho K \omega\right), \tag{2.44}$$

where τ_{ij}^F is the turbulent stress based on the Boussinesq eddy-viscosity hypothesis:

$$\tau_{ij}^F = 2\mu_T S_{ij} - \frac{2}{3}\mu_T \frac{\partial u_i}{\partial x_i}\delta_{ij} - \frac{2}{3}\rho K \delta_{ij}. \tag{2.45}$$

Here, the strain rate tensor is given by

$$S_{ij} = \frac{1}{2}\left(\frac{\partial u_i}{\partial x_j} + \frac{\partial u_j}{\partial x_i}\right). \tag{2.46}$$

The turbulent eddy viscosity is

$$\mu_T = \frac{a_1 \rho K}{\max\left(a_1 \omega, f_2 \sqrt{2 S_{ij} S_{ij}}\right)}. \tag{2.47}$$

Note that the SST-2003 version [30] uses the strain invariant rather than magnitude of vorticity in its definition.

The function f_1 in Eq. (2.43), which blends the model coefficients of the $K-\omega$ model in boundary layers with the transformed $K-\epsilon$ model in free shear layers and freestream zones, is defined as

$$\begin{aligned} f_1 &= \tanh\left(arg_1^4\right) \\ arg_1 &= \min\left[\max\left(\frac{\sqrt{K}}{0.09\omega d}, \frac{500\mu_L}{\rho\omega d^2}\right), \frac{4\rho\sigma_{\omega 2} K}{CD_{K\omega} d^2}\right], \end{aligned} \tag{2.48}$$

where d stands for the distance to the nearest wall and $CD_{K\omega}$ is the positive part of the cross-diffusion term in Eq. (2.43), i.e.,

$$CD_{K\omega} = \max\left(2\frac{\rho\sigma_{\omega 2}}{\omega}\frac{\partial K}{\partial x_i}\frac{\partial \omega}{\partial x_i}, 10^{-10}\right). \tag{2.49}$$

The auxiliary function f_2 in Eq. (2.47) is given by

$$\begin{aligned} f_2 &= \tanh\left(arg_2^2\right) \\ arg_2 &= \max\left(\frac{2\sqrt{K}}{0.09\omega d}, \frac{500\mu_L}{\rho\omega d^2}\right). \end{aligned} \tag{2.50}$$

The model constants are as follows:

$$a_1 = 0.31, \quad \beta_T^* = 0.09, \quad \kappa = 0.41. \tag{2.51}$$

Finally, the coefficients of the SST turbulence model β_T, C_ω, σ_K, and σ_ω are obtained by blending the coefficients of the $K-\omega$ model, denoted as ϕ_1^T, with those of the transformed $K-\epsilon$ model (ϕ_2^T). The corresponding relation is

$$\phi^T = f_1\phi_1^T + (1-f_1)\,\phi_2^T. \tag{2.52}$$

The coefficients of the inner model ($K-\omega$) are given by

$$\sigma_{K1} = 0.85, \quad \sigma_{\omega 1} = 0.5, \quad \beta_1^T = 0.075, \quad C_{\omega 1} = 5/9. \tag{2.53}$$

The coefficients of the outer model ($K-\epsilon$) are defined as

$$\sigma_{K2} = 1.0, \quad \sigma_{\omega 2} = 0.856, \quad \beta_2^T = 0.0828, \quad C_{\omega 2} = 0.44. \tag{2.54}$$

2.5 System preconditioning

In general, numerical methods for compressible flows provide good stability and convergence characteristics for the regime of transonic and supersonic flows. At low speeds, however, system stiffness resulting from disparate convective and acoustic velocities leads to deterioration of the convergence rates. By altering the acoustic speed of the system, the convergence rates can be independent of the Mach number such that all system eigenvalues are of the same order. The governing equations (Eqs. (2.1) and (2.39)) are preconditioned by premultiplying the time derivative term using the preconditioning matrix introduced by Weiss and Smith [33] as follows:

$$\boldsymbol{\Gamma}\frac{\partial}{\partial\tau}\int_\Omega \boldsymbol{Q}d\Omega + \oint_{\partial\Omega}\left[(\boldsymbol{F_c}-\boldsymbol{F_v})\cdot\boldsymbol{n}\right]dS = \int_\Omega \boldsymbol{D}d\Omega + \int_\Omega \boldsymbol{D_T}d\Omega, \tag{2.55}$$

where Q indicates the primitive variable vector given by

$$\boldsymbol{Q} = [p \quad u \quad v \quad w \quad T \quad y_v \quad y_g \quad K \quad \omega]^T, \tag{2.56}$$

and the preconditioning matrix $\mathbf{\Gamma}$ is

$$\begin{bmatrix} \frac{1}{\beta} & 0 & 0 & 0 & \frac{\partial\rho}{\partial T} & \frac{\partial\rho}{\partial y_v} & \frac{\partial\rho}{\partial y_g} & 0 & 0 \\ \frac{u}{\beta} & \rho & 0 & 0 & \frac{\partial\rho}{\partial T}u & \frac{\partial\rho}{\partial y_v}u & \frac{\partial\rho}{\partial y_g}u & 0 & 0 \\ \frac{v}{\beta} & 0 & \rho & 0 & \frac{\partial\rho}{\partial T}v & \frac{\partial\rho}{\partial y_v}v & \frac{\partial\rho}{\partial y_g}v & 0 & 0 \\ \frac{w}{\beta} & 0 & 0 & \rho & \frac{\partial\rho}{\partial T}w & \frac{\partial\rho}{\partial y_v}w & \frac{\partial\rho}{\partial y_g}w & 0 & 0 \\ H^* & \rho u & \rho v & \rho w & \frac{\partial\rho}{\partial T}H+\rho\frac{\partial h}{\partial T} & \frac{\partial\rho}{\partial y_v}H+\rho\frac{\partial h}{\partial y_v} & \frac{\partial\rho}{\partial y_g}H+\rho\frac{\partial h}{\partial y_g} & 0 & 0 \\ \frac{y_v}{\beta} & 0 & 0 & 0 & \frac{\partial\rho}{\partial T}y_v & \frac{\partial\rho}{\partial y_v}y_v+\rho & \frac{\partial\rho}{\partial y_g}y_v & 0 & 0 \\ \frac{y_g}{\beta} & 0 & 0 & 0 & \frac{\partial\rho}{\partial T}y_g & \frac{\partial\rho}{\partial y_v}y_g & \frac{\partial\rho}{\partial y_g}y_g+\rho & 0 & 0 \\ \frac{K}{\beta} & 0 & 0 & 0 & \frac{\partial\rho}{\partial T}K & \frac{\partial\rho}{\partial y_v}K & \frac{\partial\rho}{\partial y_g}K & \rho & 0 \\ \frac{\omega}{\beta} & 0 & 0 & 0 & \frac{\partial\rho}{\partial T}\omega & \frac{\partial\rho}{\partial y_v}\omega & \frac{\partial\rho}{\partial y_g}\omega & 0 & \rho \end{bmatrix} \tag{2.57}$$

with

$$H^* = \frac{H}{\beta} + \rho\frac{\partial h}{\partial p} - 1. \tag{2.58}$$

If $1/\beta = \frac{\partial\rho}{\partial p}$, $\mathbf{\Gamma}$ goes back to $\frac{\partial \boldsymbol{W}}{\partial \boldsymbol{Q}}$, resulting in a non-preconditioned system in the primitive form. The eigenvalues of the preconditioned system in Eq. (2.55) are given by

$$\lambda\left(\mathbf{\Gamma^{-1}}\frac{\partial \boldsymbol{F}}{\partial \boldsymbol{Q}}\right) = U, U, U, U, U, U, U, U' - D, U' + D, \tag{2.59}$$

where

$$U' = \frac{1}{2}\left(1 + \frac{c'^2}{c^2}\right)U, \tag{2.60}$$

$$D = \frac{1}{2}\sqrt{\left(1 - \frac{c'^2}{c^2}\right)^2 U^2 + 4c'^2}. \tag{2.61}$$

Here, $U\,(\equiv n_x u + n_y v + n_z w)$ is the contravariant velocity component normal to the surface element dS.

The speed of sound c is

$$c^2 \equiv \left.\frac{\partial p}{\partial \rho}\right|_s = \frac{\rho\frac{\partial h}{\partial T}}{\rho\frac{\partial\rho}{\partial p}\frac{\partial h}{\partial T} + \frac{\partial\rho}{\partial T}\left(1 - \rho\frac{\partial h}{\partial p}\right)}. \tag{2.62}$$

The relation between $1/\beta$ and c' is

$$\frac{1}{\beta} = \frac{1}{c'^2} - \frac{\frac{\partial \rho}{\partial T}\left(1 - \rho\frac{\partial h}{\partial p}\right)}{\rho\frac{\partial h}{\partial T}}. \tag{2.63}$$

The preconditioned speed of sound c' is then given by

$$c' = \min\left(c, \max\left(\sqrt{u^2 + v^2 + w^2}, V_{co}\right)\right). \tag{2.64}$$

In Eq. (2.64), V_{co} is a cut-off value that is typically used to prevent the preconditioned speed of sound from becoming zero in the vicinity of stagnation region (where the local velocity magnitude is zero). The cut-off parameter V_{co} is generally specified as $V_{co} = kV_\infty$, where V_∞ is a freestream velocity and k is set to one in this work. The cut-off parameter V_{co} should have non-zero value, or the preconditioned speed of sound becomes zero as mentioned above, and could lead to a floating point error. For supersonic flows, the preconditioned speed of sound becomes the local speed of sound, turning off the system preconditioning.

Since the system preconditioning destroys the temporal accuracy of the governing equations, Eq. (2.55) is restricted to steady-state calculations with the pseudo-time τ. For unsteady computations, the dual time-stepping method is employed in which the preconditioned pseudo-time derivative term is introduced in addition to the physical time derivative in Eq. (2.1):

$$\boldsymbol{\Gamma}\frac{\partial}{\partial \tau}\int_\Omega \boldsymbol{Q} d\Omega + \frac{\partial}{\partial t}\int_\Omega \boldsymbol{W} d\Omega + \oint_{\partial\Omega}\left[(\boldsymbol{F_c} - \boldsymbol{F_v})\cdot \boldsymbol{n}\right] dS = \int_\Omega \boldsymbol{D} d\Omega + \int_\Omega \boldsymbol{D_T} d\Omega, \tag{2.65}$$

where t denotes the physical time and τ is the pseudo-time used in the sub-iteration procedure. In this way, the physical time-step size is not affected by the stiffness of the system, whereas convergence of the inner iterations in the pseudo-time is optimized by judicious selection of the preconditioning method

(or design of the preconditioned speed of sound, c'). For calculating unsteady flows with a large physical time step Δt, Eq. (2.64) is an optimal choice. However, it is sub-optimal for intermediate and small time steps, causing unsatisfactory convergence behavior. In order to overcome this, Venkateswaran and Merkle [34] proposed a preconditioning method that takes the effect of the Strouhal number into account through von Neumann stability analysis of the dual time-stepping method. The resulting unsteady preconditioning parameter is given by

$$V_{un} = \frac{L}{\pi \Delta t} = \frac{L}{\pi \Delta t V} \times V = Str \times V, \tag{2.66}$$

where L is a characteristic length scale and Δt is the physical time step size. The characteristic length scale is typically taken as the problem domain size, a representative scale of the lowest wave number. Though Eq. (2.66) was derived for single-phase gas flows, it can be applicable to two-phase flows because two-phase effects described the homogeneous mixture equations simply change the magnitude of the speed of sound. Considering Eq. (2.66), the preconditioned speed of sound c' for unsteady flows is given by

$$c'_{un} = \min\left(c, \max\left(\sqrt{u^2 + v^2 + w^2}, V_{co}, V_{un}\right)\right). \tag{2.67}$$

For steady flows or low Strouhal number flows with a large time step, V_{co} is larger than V_{un}; consequently, the preconditioned speed of sound is the same as in Eq. (2.64). For an intermediate time step, the unsteady velocity (V_{un}) can be larger than the local velocity ($\sqrt{u^2 + v^2 + w^2}$) and unsteady preconditioning takes effect. As the time step becomes small for high Strouhal number flows, the unsteady velocity can completely turn off the system preconditioning, thus reverting the preconditioned speed of sound c' to the original speed of sound c. This corresponds to a physical situation where pressure wave propagate with respect to the original speed of sound. Thus, Eq. (2.67) may promise an optimal

convergence for inner iterations at all flow speeds and for all values of time step sizes.

Chapter 3

Computational Methods

In finite volume method, the governing equation (Eq. (2.1)) is integrated on the each computational cell Ω_i,

$$\frac{\partial}{\partial t}\int_{\Omega_i} \boldsymbol{W} d\Omega + \oint_{\partial\Omega_i} \left[(\boldsymbol{F_c} - \boldsymbol{F_v}) \cdot \vec{n}\right] dS = \int_{\Omega_i} \boldsymbol{D} d\Omega. \tag{3.1}$$

Depending on the location of physical variables, one may use either a cell-centered or a cell-vertex approach. A cell-centered approach is adopted in the present work. With the second-order accurate spatial discretization and numerical flux function, the semi-discrete form of Eq. (3.1) can be written as follows:

$$\frac{\partial \bar{\boldsymbol{W}}}{\partial t} + \frac{1}{|\Omega_i|}\sum_{e_{ik}\in\Omega_i} \left\{\boldsymbol{H_c}\left(\bar{\boldsymbol{Q}}_{ik}, \bar{\boldsymbol{Q}}_{ki}, \boldsymbol{n}\right) - \boldsymbol{H_v}\left(\bar{\boldsymbol{Q}}, \nabla\bar{\boldsymbol{Q}}, \boldsymbol{n}\right)\right\} |e_{ik}| = \boldsymbol{D}\left(\bar{\boldsymbol{Q}}\right), \tag{3.2}$$

where $\bar{\boldsymbol{W}}$, $\bar{\boldsymbol{Q}}$ denote the cell-averaged conservative and primitive variable vector, respectively. Here, $\bar{\boldsymbol{Q}}_{ik}$ is the cell interface state vector of the direction from cell Ω_i to the cell Ω_i. $|\Omega_i|$ is the volume of the cell Ω_i. e_{ik} denotes the face between

Ω_i and Ω_k, $|e_{ik}|$ is its area. $\boldsymbol{H_c}$ and $\boldsymbol{H_v}$ are the numerical inviscid and viscous flux tensor, respectively.

In order to solve Eq. (3.2), following elements are needed.

- Robust and accurate numerical flux $\boldsymbol{H_c}$ and $\boldsymbol{H_v}$.
- Interpolation of $\bar{\boldsymbol{Q}}_{ik}$.
- Time integration methods.

In this chapter, these elements are discussed.

3.1 Inviscid flux schemes

We begin with briefly introducing the baseline schemes for homogeneous two-phase flows at all speeds. The AUSMPW+ and RoeM schemes, which were originally developed for compressible gas flows, have been extended to air-water two-phase flows. Both schemes have been proven to be robust and accurate without compromising the accuracy of the original schemes. A detailed derivation and discussion on the features of these schemes can be found in Ref. [35].

3.1.1 Two-phase AUSMPW+ scheme

The numerical flux of two-phase AUSMPW+ at a cell-interface is written as follows:

$$\boldsymbol{H_c}^{\text{AUSMPW+}}\left(\bar{\boldsymbol{Q}}_L, \bar{\boldsymbol{Q}}_R, \boldsymbol{n}\right) = \bar{\mathscr{M}}_L^+ c_{1/2}^* \boldsymbol{\psi}_L + \bar{\mathscr{M}}_R^- c_{1/2}^* \boldsymbol{\psi}_R + \boldsymbol{p}_{1/2}, \tag{3.3}$$

where

$$\boldsymbol{\psi} = [\rho \quad \rho u \quad \rho v \quad \rho w \quad \rho H \quad \rho y_v \quad \rho y_g]^T, \tag{3.4}$$

$$\boldsymbol{p}_{1/2} = [0 \quad n_x p_{1/2} \quad n_y p_{1/2} \quad n_z p_{1/2} \quad 0 \quad 0 \quad 0]^T. \tag{3.5}$$

The pressure flux is

$$p_{1/2} = \mathscr{P}_L^+ p_L + \mathscr{P}_R^- p_R. \tag{3.6}$$

In order to prevent unwanted oscillations near wall and overshoots behind a strong shock, AUSMPW+ uses pressure-based weighting functions which provide a numerical dissipation proportional to local pressure difference. The pressure-based weighting functions f and ω are defined as

$$f_{L,R} = \left(\frac{\bar{p}_{L,R}}{\bar{p}_s} - 1\right)(1-\omega)\frac{\min(\rho_L, \rho_R)}{\rho_{L/R}}, \tag{3.7}$$

$$\omega = \max(\omega_1, \omega_2) \tag{3.8}$$

with $\omega_1 = 1 - \Pi_{1/2}^3$ and

$$\omega_2 = 1 - \min_{e_{mn} \in \Omega_L \cup \Omega_R, mn \neq LR} \left(\frac{\bar{p}_m}{\bar{p}_n}, \frac{\bar{p}_n}{\bar{p}_m}\right)^2, \tag{3.9}$$

where

$$()_{L/R} = \begin{cases} ()_L & M_{1/2} \geq 0 \\ ()_R & M_{1/2} < 0 \end{cases}. \tag{3.10}$$

In above weighting functions, a shock-discontinuity-sensing term $\Pi_{1/2}$ is introduced to capture two-phase shock discontinuity. The shock-discontinuity-sensing term, Π, and modified pressure $\bar{p}$ in the above equations will be described in greater detail at a later section.

$\bar{\mathscr{M}}_{L,R}^{\pm}$ in Eq. (3.3) are defined as follows:

(i) if $M_{1/2}^* \geq 0$,

$$\bar{\mathscr{M}}_L^+ = \mathscr{M}_L^+ + \mathscr{M}_R^-[(1-\omega)(1+f_R^*) - f_L^*], \tag{3.11}$$

$$\bar{\mathscr{M}}_R^- = \mathscr{M}_R^- \omega(1+f_R^*). \tag{3.12}$$

(ii) if $M^*_{1/2} < 0$,

$$\bar{\mathscr{M}}_L^+ = \mathscr{M}_L^+ \omega(1 + f_L^*), \tag{3.13}$$

$$\bar{\mathscr{M}}_R^- = \mathscr{M}_R^- + \mathscr{M}_L^+[(1-\omega)(1+f_L^*) - f_R^*]. \tag{3.14}$$

For all-speed flow calculations, the scaling technique by Edwards and Liou [36] has been adopted. The scaled Mach number is defined as

$$M^*_{L,R} = \frac{1+\theta^2_{1/2}}{2} \times \frac{M_{L,R}}{\phi_{1/2}} + \frac{1-\theta^2_{1/2}}{2} \times \frac{M_{R,L}}{\phi_{1/2}}, \tag{3.15}$$

where

$$\theta = \frac{c'}{c}. \tag{3.16}$$

The function $\phi_{1/2}$ is introduced to reflect the preconditioned eigenvalues in the following form:

$$\phi_{1/2} = \frac{\sqrt{(1-\theta^2_{1/2})M^2_{1/2} + 4\theta^2_{1/2}}}{1+\theta^2_{1/2}}. \tag{3.17}$$

The preconditioned speed of sound c' in Eq. (3.16) is the same as in Eq. (2.64). In addition, the pressure-difference term in f is scaled using θ to prevent the odd-even decoupling problem in the low Mach number regime as follows:

$$f^* = f \times \frac{1}{\theta^2}. \tag{3.18}$$

Referring to Eq. (3.3), the Mach number and pressure splitting functions $\mathscr{M}^{\pm}_{L,R}$ and $\mathscr{P}^{\pm}_{L,R}$ at a cell-interface are obtained using the above scaled Mach number M^* as follows:

$$\mathscr{M}^{\pm} = \begin{cases} \pm\frac{1}{4}\left(M^* \pm 1\right)^2 & |M^*| \le 1 \\ \frac{1}{2}\left(M^* \pm |M^*|\right) & |M^*| > 1 \end{cases}, \tag{3.19}$$

$$\mathscr{P}^{\pm} = \begin{cases} \pm\frac{1}{4}\left(M^* \pm 1\right)^2 (2 \mp M^*) \pm \alpha M^* \left(M^{*2} - 1\right)^2 & |M^*| \le 1 \\ \frac{1}{2}\left(1 \pm \operatorname{sign}(M^*)\right) & |M^*| > 1 \end{cases}. \tag{3.20}$$

The choice of the numerical speed of sound at a cell-interface is crucial to accurate capturing of shock discontinuity in AUSM-type schemes. Unlike gas dynamics, there is no Prandtl-like relation for general two-phase flows, and thus the speed of sound in the original AUSMPW+ scheme is not used for two-phase flows. Instead, the two-phase AUSMPW+ uses the Roe-averaged enthalpy and mass fraction for calculating the interfacial speed of sound $c_{1/2}$, which is consistent with the physical speed of sound for mixture flows. Finally, the scaled interfacial speed of sound in Eq. (3.3) becomes

$$c^*_{1/2} = c_{1/2} \times \phi_{1/2}. \tag{3.21}$$

3.1.2 Two-phase RoeM scheme

The RoeM scheme for two-phase flows at a cell-interface is expressed as follows:

$$\begin{aligned}\boldsymbol{H_c}^{\mathrm{RoeM}}\left(\bar{\boldsymbol{Q}}_L, \bar{\boldsymbol{Q}}_R, \boldsymbol{n}\right) = \frac{1}{b_1^* - b_2^*}\Bigg[& b_1^* \boldsymbol{F_c}\left(\bar{\boldsymbol{Q}}_L\right) - b_2^* \boldsymbol{F_c}\left(\bar{\boldsymbol{Q}}_R\right) \\ & + b_1^* b_2^* (\Delta \boldsymbol{W'} - \frac{g}{1+|\tilde{M}^*|} \boldsymbol{B} \Delta \boldsymbol{W'})\Bigg],\end{aligned} \tag{3.22}$$

where

$$\Delta \boldsymbol{W'} = [\Delta(\rho) \quad \Delta(\rho u) \quad \Delta(\rho v) \quad \Delta(\rho w) \quad \Delta(\rho H) \quad \Delta(\rho y_v) \quad \Delta(\rho y_g)]^T \tag{3.23}$$

and

$$\boldsymbol{B}\Delta \boldsymbol{W'} = \left(\Delta\rho - \frac{f\Delta p}{\hat{D}^2}\right) \begin{pmatrix} 1 \\ \hat{u} \\ \hat{v} \\ \hat{w} \\ \hat{H} \\ \hat{y}_v \\ \hat{y}_g \end{pmatrix} + \hat{\rho} \begin{pmatrix} 0 \\ \Delta u - n_x \Delta U \\ \Delta v - n_y \Delta U \\ \Delta w - n_z \Delta U \\ \Delta H \\ \Delta y_v \\ \Delta y_g \end{pmatrix}. \tag{3.24}$$

In Eq. (3.22), $\tilde{M}^* = sign(\hat{M}^*) \times \min(1, |\hat{M}^*|)$ and $\hat{M}^* = \hat{U}'/\hat{D}$, where the asterisk designates scaled values and the caret designates Roe-averaged values. Thus, $\hat{U}'$ and $\hat{D}$ have the same form as U' and D in Eqs. (2.60) and (2.61) but with Roe-averaged values. Recall that U' and D use the preconditioned speed of sound in Eq. (2.64). To prevent expansion shock without compromising the capturing of contact discontinuity, the following signal velocities are introduced:

$$b_1^* = \max\left(\hat{U}' + \hat{D}, U_R' + \hat{D}, 0\right), \tag{3.25}$$

$$b_2^* = \min\left(\hat{U}' - \hat{D}, U_L' - \hat{D}, 0\right). \tag{3.26}$$

In the above description, the HLLC-type preconditioning strategy from Luo *et al.* [37] is employed; therefore, the Mach number and eigenvalues are simply replaced by preconditioned values.

The Mach-number-based control functions f and g are then defined as follows:

$$f = \begin{cases} 1 & \hat{u}^2 + \hat{v}^2 + \hat{w}^2 = 0 \\ |\hat{M}^*|^h & \text{elsewhere} \end{cases}, \tag{3.27}$$

$$g = \begin{cases} 1 & \hat{M}^* = 0 \\ |\hat{M}^*|^{1-\Pi_{1/2}} & \hat{M}^* \neq 0 \end{cases}, \tag{3.28}$$

where

$$h = 1 - \min_{e_{mn} \in \Omega_L \cup \Omega_R} \left(\frac{\bar{p}_m}{\bar{p}_n}, \frac{\bar{p}_n}{\bar{p}_m}\right). \tag{3.29}$$

As in case of the AUSMPW+ scheme, $\Pi_{1/2}$ is a shock-discontinuity-sensing term. Based on linear perturbation analysis, f is designed to damp out the feeding rate of pressure perturbation into the density field, and g is designed to control the damping rate of density and pressure perturbation. As a result, the

multi-dimensional dissipation provided by f and g prevents the shock instability triggered by the pressure-difference term in the mass flux of the original Roe scheme.

3.1.3 Shock-discontinuity-sensing term for real fluid flows

The two-phase AUSMPW+ and RoeM schemes have sensing functions ($\Pi_{1/2}$ in Eqs. (3.8), (3.29)) that check pressure distribution around a cell-interface. The amount of numerical dissipation is then controlled by designing weighting functions (Eqs. (3.7), (3.8) for AUSMPW+, and Eqs. (3.27), (3.28) for RoeM), which provide the enhanced stability and accuracy compared with the original AUSM-type or Roe-type schemes.

The original shock-discontinuity-sensing term for gas dynamics uses the ratio of the left and right pressure values across a cell-interface as follows:

$$\Pi^o_{1/2} = \min\left(\frac{p_L}{p_R}, \frac{p_R}{p_L}\right). \tag{3.30}$$

This shock-discontinuity-sensing term is designed to be close to zero at a region where a shock is present and near one in smooth regions. Unlike in gas dynamics, the pressure field of two-phase flows can change drastically near the liquid phase, even in subsonic regions. This is because the liquid phase typically has a large density and a high speed of sound compared with the gas phase. Thus, despite the drastic change in pressure, the pressure field can be smooth without the presence of a shock wave. The shock-discontinuity-sensing term in Eq. (3.30) does not recognize this physical situation and grossly misinterprets such physically non-shock regions as shock regions.

To overcome this difficulty, a shock-discontinuity-sensing term based on the

derivative of the mixture density was introduced in the previous research [35]:

$$\Pi_{1/2} = \min\left(\frac{\bar{p}_L}{\bar{p}_R}, \frac{\bar{p}_R}{\bar{p}_L}\right) \tag{3.31}$$

with

$$\bar{p}_{L,R} = \frac{1}{\frac{\alpha_{1/2}}{p_{L,R}} + \frac{1-\alpha_{1/2}}{p_{L,R}+p_c}}, \tag{3.32}$$

where $\alpha_{1/2}$ is the volume fraction of the gas phase. In Eq. (3.32), the term of interest is p_c, which originates from the stiffened EOS for liquid water. The role of p_c can be understood by rewriting Eq. (3.31), with $\alpha_{1/2} = 0$ and $p_L < p_R$, as follows:

$$\Pi_{1/2} = \frac{p_L + p_c}{p_R + p_c}. \tag{3.33}$$

If the pressure difference at a cell-interface $(p_R - p_L)$ is sufficiently lower than p_c, $\Pi_{1/2}$ essentially remains near one and the cell-interface is not recognized as a shock region. If the pressure difference becomes substantially greater than p_c, $\Pi_{1/2}$ is close to zero and the cell-interface is recognized as a shock region. Thus, p_c acts as a threshold value that determines a proper amount of the pressure difference to capture a shock wave.

In cases of other EOSs, such as the Tait's EOS, van der Waals EOS, and Peng-Robinson EOS, Eq. (3.31) is still applicable and a term similar to p_c can be derived. In cases of real fluids such as IAPWS97 database, however, it is impossible to obtain a term similar to p_c. It is thus essential to derive a shock-discontinuity-sensing term that does not contain a term dependent on a specific form of EOS. From this perspective, the basic idea is to derive a term similar to p_c without involving a specific form of EOS, and the starting point is the

steady one-dimensional normal shock relations.

$$\rho_1 u_1 = \rho_2 u_2, \tag{3.34}$$

$$p_1 + \rho_1 u_1^2 = p_2 + \rho_2 u_2^2, \tag{3.35}$$

$$h_1 + \frac{1}{2}u_1^2 = h_2 + \frac{1}{2}u_2^2, \tag{3.36}$$

where the subscripts 1 and 2 indicate before- and after-shock values, respectively. Combining Eq. (3.35) and Eq. (3.34), we can obtain the pressure difference across a shock wave as follows:

$$p_2 - p_1 = \rho_1 c_1^2 \frac{u_1}{c_1}\frac{(u_1 - u_2)}{c_1} = \rho_1 c_1^2 \left(\breve{M}_1^2 - \breve{M}_1\breve{M}_2\right), \tag{3.37}$$

where $\breve{M}_1$ and $\breve{M}_2$ stand, respectively, for the before- and after-shock Mach numbers based on the before-shock speed of sound. If we consider a weak normal shock case where u_1 is slightly greater than c_1, the pressure difference would be bounded by $\rho_1 c_1^2$ because $u_1 - u_2$ in Eq. (3.37) cannot exceed c_1. As a result, $\breve{M}_1^2 - \breve{M}_1\breve{M}_2$ would be bounded by unity. As $\breve{M}_1$ increases (or the shock strength becomes higher), $\breve{M}_1^2 - \breve{M}_1\breve{M}_2$ would increase rapidly since $\breve{M}_1^2 - \breve{M}_1\breve{M}_2 = \breve{M}_1(\breve{M}_1 - \breve{M}_2) >> \breve{M}_1$. Thus, the pressure difference becomes much larger than $\rho_1 c_1^2$. In case of subsonic flows ($\breve{M}_1 < 1$ and $p_1 < p_2$), $\breve{M}_1^2 - \breve{M}_1\breve{M}_2 = \breve{M}_1(\breve{M}_1 - \breve{M}_2) << \breve{M}_1$. Therefore, it is reasonable to estimate the threshold value similar to p_c as $k\rho_1 c_1^2$ with $k < 1$, and a new shock-discontinuity-sensing term is designed as follows:

$$\Pi_{1/2}^* = \min\left(\frac{\bar{p}_L^*}{\bar{p}_R^*}, \frac{\bar{p}_R^*}{\bar{p}_L^*}\right) \tag{3.38}$$

with

$$\bar{p}^*_{L,R} = p_{L,R} + 0.1 \times \min\left(\rho_L c_L^2, \rho_R c_R^2\right), \tag{3.39}$$

where the subscripts L and R indicate the left and right cell-interface value, respectively. It is noted that the newly introduced $\bar{p}^*_{L,R}$ only requires the mixture density and speed of sound across a cell-interface which can be defined without a specific form of EOS.

For the detailed information about the shock-discontinuity-sensing term, see Ref. [24]. In this study, Eq. (3.38) with Eq. (3.39) is applied for all computations.

3.1.4 Scaling of numerical fluxes

In Section 2.5, system preconditioning was discussed primarily as a convergence enhancement method. The other important aspect of system preconditioning is its effect on accuracy through the scaling of numerical dissipation. In the previous research [35], the numerical dissipation of the RoeM and AUSMPW+ schemes was scaled by employing HLLC-type [37] and AUSM-type [36] preconditioning strategies, respectively. Although these scaling methods have been applied with much success to steady low Mach number flows, they perform poorly for unsteady low Mach number computations, particularly for the cases of small time scales or high Strouhal numbers. For unsteady flows, evaluating the terms in Eqs. (2.60) and (2.61) by using the steady preconditioned speed of sound (Eq. (2.64)) results in excessive numerical dissipation associated with the pressure-difference term, while that related to the velocity-difference term can be optimally scaled. On the other hand, when the unsteady preconditioned speed of sound (Eq. (2.67)) is used to evaluate the terms (Eqs. (2.60) and (2.61)), the numerical dissipation related to the pressure-difference term can be controlled optimally but that related to the velocity-difference term becomes

excessive. This suggests that the independent scaling of the two dissipation terms is necessary [38, 39, 40]. In order to implement this observation to two-phase AUSMPW+ and RoeM schemes, we firstly apply the scaling function of AUSM$^+$-up scheme [41] to the pressure-difference dissipation term as follows:

$$\phi_p = \theta_p \left(2 - \theta_p\right), \tag{3.40}$$

where

$$\theta_p = \min\left(1, \max\left(\frac{\sqrt{u_{1/2}^2 + v_{1/2}^2 + w_{1/2}^2}}{c_{1/2}}, \frac{V_{co}}{c_{1/2}}, \frac{V_{un}}{c_{1/2}}\right)\right). \tag{3.41}$$

This means that the unsteady preconditioned speed of sound is only used to scale the dissipation associated with the pressure-difference term. For the dissipation related to the velocity-difference term, the scaling based on local velocity is considered as follows:

$$\phi_v = \theta_v \left(2 - \theta_v\right), \tag{3.42}$$

where

$$\theta_v = \min\left(1, \max\left(\frac{\sqrt{u_{1/2}^2 + v_{1/2}^2 + w_{1/2}^2}}{c_{1/2}}, \frac{V_{co}}{c_{1/2}}\right)\right). \tag{3.43}$$

In order to scale the numerical dissipation consistently along the boundaries of a cell, we use the magnitude of local velocity ($\sqrt{u_{1/2}^2 + v_{1/2}^2 + w_{1/2}^2}$) rather than the normal velocity component ($u_{1/2}n_x + v_{1/2}n_y + w_{1/2}n_z$).

From here on, Eqs. (3.40) and (3.42) are used for scaling the numerical dissipation of two-phase AUSMPW+ and RoeM schemes.

3.1.5 Scaling of two-phase AUSMPW+ scheme

As discussed in Subsection 3.1.1, the previous two-phase AUSMPW+ scheme uses the relatively complicated scaled Mach number M^* (Eq. (3.15)) to calculate

the Mach number and pressure splitting functions at a cell-interface, $\mathscr{M}^{\pm}_{L,R}$ and $\mathscr{P}^{\pm}_{L,R}$. For efficient all-speed scaling, we abandon this scaled Mach number approach and instead employ the simple scaling method of AUSM^{+}-up scheme. We do this by adding the velocity-difference flux term p_u given in Ref. [41] into the pressure flux of the original two-phase AUSMPW+ scheme as follows:

$$p_{1/2} = \mathscr{P}^{+}_{L} p_L + \mathscr{P}^{-}_{R} p_R + p_u, \tag{3.44}$$

where

$$p_u = -2K_u \mathscr{P}^{+}_{L} \mathscr{P}^{-}_{R} \rho_{1/2} c_{1/2} \left(U_R - U_L\right), \tag{3.45}$$

with $0 \leq K_u \leq 1$. In all calculations, we set $K_u = 0.5$. It is noteworthy that the added velocity diffusion term was inspired by approximating the characteristic relation $\mathrm{d}p \pm \rho c \mathrm{d}u = 0$. Since AUSMPW+ already contains a pressure-difference term through the weighting function (Eq. (3.7)), additional pressure diffusion is not necessary.

A newly scaled two-phase AUSMPW+ scheme for real fluids can then be obtained by using the scaling functions given in Eqs. (3.40) and (3.42). Firstly, the Mach number and pressure splitting functions $\mathscr{M}^{\pm}_{L,R}$ and $\mathscr{P}^{\pm}_{L,R}$ across a cell-interface are obtained using the Mach number M as follows:

$$M_{L,R} = \frac{U_{L,R}}{c_{1/2}}. \tag{3.46}$$

The velocity-difference pressure flux (Eq. (3.45)) is then scaled using the velocity scaling function (Eq. (3.42)) as follows:

$$p_u = -2K_u \mathscr{P}^{+}_{L} \mathscr{P}^{-}_{R} \phi_v \rho_{1/2} c_{1/2} \left(U_R - U_L\right) \tag{3.47}$$

with α given by

$$\alpha = \frac{3}{16}\left(-4 + 5\phi_v^2\right) \in \left[-\frac{3}{4}, \frac{3}{16}\right]. \tag{3.48}$$

Next, the pressure-difference term (Eq. (3.7)) is scaled by the pressure scaling function (Eq. (3.40)) and the new two-phase shock-discontinuity-sensing term (Eq. (3.38) with Eq. (3.39)) as follows:

$$f^*_{L,R} = \left(\frac{p_{L,R} + \rho_{1/2} c^2_{1/2}}{\rho_{1/2} c^2_{1/2}} - 1 \right) (1 - \omega^*) \frac{\rho_{1/2}}{\rho_{L/R}} \frac{1}{\phi_p}, \tag{3.49}$$

$$\omega^* = \max(\omega^*_1, \omega^*_2), \tag{3.50}$$

where $\omega^*_1 = 1 - \Pi^{*3}_{1/2}$ and

$$\omega^*_2 = 1 - \min_{e_{mn} \in \Omega_L \cup \Omega_R, mn \neq LR} \left(\frac{\bar{p}^*_m}{\bar{p}^*_n}, \frac{\bar{p}^*_n}{\bar{p}^*_m} \right)^2. \tag{3.51}$$

3.1.6 Scaling of two-phase RoeM scheme

Similar to the scaling of the two-phase AUSMPW+ scheme, it is necessary to treat the velocity- and pressure-difference diffusion terms separately in the two-phase RoeM scheme. First, the two-phase RoeM scheme without preconditioning can be written in the following form:

$$\begin{aligned} \boldsymbol{H_c}^{\mathrm{RoeM}} \left(\bar{\boldsymbol{Q}}_L, \bar{\boldsymbol{Q}}_R, \boldsymbol{n} \right) = \frac{1}{2} \Big[& \boldsymbol{F_c} \left(\bar{\boldsymbol{Q}}_L \right) + \boldsymbol{F_c} \left(\bar{\boldsymbol{Q}}_R \right) - \tilde{M} \Delta \boldsymbol{F_c} + \left(\tilde{M} \hat{U} - \tilde{c} \right) \Delta \boldsymbol{W'} \\ & + g \left(\tilde{c} - |\hat{U}| \right) \boldsymbol{B} \Delta \boldsymbol{W'} \Big], \end{aligned} \tag{3.52}$$

where

$$\boldsymbol{B} \Delta \boldsymbol{W'} = \left(\Delta \rho - \frac{f \Delta p}{\hat{c}^2} \right) \begin{pmatrix} 1 \\ \hat{u} \\ \hat{v} \\ \hat{w} \\ \hat{H} \\ \hat{y}_v \\ \hat{y}_g \end{pmatrix} + \hat{\rho} \begin{pmatrix} 0 \\ \Delta u - n_x \Delta U \\ \Delta v - n_y \Delta U \\ \Delta w - n_z \Delta U \\ \Delta H \\ \Delta y_v \\ \Delta y_g \end{pmatrix}. \tag{3.53}$$

In Eq. (3.52), $\tilde{M}$ and $\tilde{c}$ are given by

$$\tilde{M} = \frac{1}{2\hat{c}} \left(\left| \max\left(\hat{U} + \hat{c}, U_R + \hat{c}\right) \right| - \left| \min\left(\hat{U} - \hat{c}, U_L - \hat{c}\right) \right| \right), \tag{3.54}$$

$$\tilde{c} = \frac{1}{2} \left(\left| \max\left(\hat{U} + \hat{c}, U_R + \hat{c}\right) \right| + \left| \min\left(\hat{U} - \hat{c}, U_L - \hat{c}\right) \right| \right), \tag{3.55}$$

respectively. The pressure-difference term in Eq. (3.53) is then modified using the pressure scaling function (Eq. (3.40)) as follows:

$$\boldsymbol{B}\Delta\boldsymbol{W}'^{*} = \left(\Delta\rho - \frac{f\Delta p}{\phi_p \hat{c}^2} \right) \begin{pmatrix} 1 \\ \hat{u} \\ \hat{v} \\ \hat{w} \\ \hat{H} \\ \hat{y}_v \\ \hat{y}_g \end{pmatrix} + \hat{\rho} \begin{pmatrix} 0 \\ \Delta u - n_x \Delta U \\ \Delta v - n_y \Delta U \\ \Delta w - n_z \Delta U \\ \Delta H \\ \Delta y_v \\ \Delta y_g \end{pmatrix}. \tag{3.56}$$

The velocity-difference term in Eq. (3.53) is also modified by adding the following term:

$$\boldsymbol{D}_u = g\hat{\rho}\Delta U \left(\tilde{c} - \tilde{c}^*\right) \begin{pmatrix} 0 \\ n_x \\ n_y \\ n_z \\ 0 \\ 0 \\ 0 \end{pmatrix}, \tag{3.57}$$

where

$$\tilde{c}^* = \frac{1}{2} \left(\left| \max\left(\hat{U} + \phi_v \hat{c}, U_R + \phi_v \hat{c}\right) \right| + \left| \min\left(\hat{U} - \phi_v \hat{c}, U_L - \phi_v \hat{c}\right) \right| \right). \tag{3.58}$$

The newly scaled two-phase RoeM scheme for real fluids is then given by

$$\boldsymbol{H_c}^{\text{RoeM\_N}}\left(\bar{\boldsymbol{Q}}_L, \bar{\boldsymbol{Q}}_R, \boldsymbol{n}\right) = \frac{1}{2}\Big[\boldsymbol{F_c}\left(\bar{\boldsymbol{Q}}_L\right) + \boldsymbol{F_c}\left(\bar{\boldsymbol{Q}}_R\right) - \tilde{M}\Delta\boldsymbol{F_c} + \left(\tilde{M}\hat{U} - \tilde{c}\right)\Delta\boldsymbol{W'} + g\left(\tilde{c} - |\hat{U}|\right)\boldsymbol{B}\Delta\boldsymbol{W'}^{*} + \boldsymbol{D}_u\Big]. \quad (3.59)$$

In Eq. (3.59), the Mach number-based weighting functions f and g are calculated with the new two-phase shock-discontinuity-sensing term (Eq. (3.38) with Eq. (3.39)) as follows:

$$f = \begin{cases} 1 & \hat{u}^2 + \hat{v}^2 + \hat{w}^2 = 0 \\ |\hat{M}|^{h^*} & \text{elsewhere} \end{cases}, \quad (3.60)$$

$$g = \begin{cases} 1 & \hat{M} = 0 \\ |\hat{M}|^{1-\Pi^*_{1/2}} & \hat{M} \neq 0 \end{cases}, \quad (3.61)$$

where

$$h^* = 1 - \min_{e_{mn}\in\Omega_L\cup\Omega_R}\left(\frac{\bar{p}^*_m}{\bar{p}^*_n}, \frac{\bar{p}^*_n}{\bar{p}^*_m}\right). \quad (3.62)$$

From these flux scaling processes discussed above, AUSMPW+_N and RoeM_N numerical flux schemes are introduced for all-speed multi-phase flows. For the detailed derivation and discussion on the features of these schemes, see Ref. [24].

3.2 Compact scheme for viscous flux

In order to evaluate the viscous flux $\boldsymbol{H_v}$ in Eq. (3.2), a second order central differencing is adopted. This method applies a local transformation from Cartesian coordinates (x, y, z) to the curvilinear coordinates (ξ, η, ζ), e.g,

$$\frac{\partial q}{\partial x} = \frac{\partial q}{\partial \xi}\frac{\partial \xi}{\partial x} + \frac{\partial q}{\partial \eta}\frac{\partial \eta}{\partial x} + \frac{\partial q}{\partial \zeta}\frac{\partial \zeta}{\partial x}, \quad \text{etc}, \quad (3.63)$$

where q denotes the primitive variable component of primitive vector $\boldsymbol{Q}$. The derivatives q_ξ, q_η and q_ζ are obtained from finite difference approximations. For example, the non-cross derivative components are differenced by using a compact three-point formula. In addition, the cross derivative components are differenced by using nine-point formula.

3.3 Multi-dimensional limiting process (MLP)

Most oscillation-free schemes have been largely based on the mathematical analysis of on-dimensional convection equation, and applied to multi-dimensional applications with dimensional splitting. They are successful in many cases, but quite often, it is insufficient or almost impossible to control oscillations near shock discontinuity in multiple dimensions. This manifests the necessity to design oscillation control method for multi-dimensional flow physics. By extending the one-dimensional monotonic condition to two- and three-dimensional flows, the multi-dimensional limiting condition is proposed, and with this limiting condition, the multi-dimensional limiting process (MLP) [42, 43] is can be formulated. The starting point is the observation that the dimensional splitting extension does not possess any information on property distribution at cell vertex points, whose information is essential when property gradient is not aligned with local grid lines. In order to derive the multi-dimensional limiting function, the vertex point value is expressed in terms of variations across cell-interface. And then, the variation is determined to satisfy the multi-dimensional limiting condition using the limiting coefficient α. The coefficient α possesses the information of multi-dimensionally distributed physical property. With the coefficient α, the multi-dimensional limiting function can be formulated. Finally, a new family of limiters to control oscillations in multi-dimensional flows can be

developed. In order to calculate $\bar{\boldsymbol{Q}}_{ik}$ and $\bar{\boldsymbol{Q}}_{ki}$ of Eq. (3.2) in three-dimensional flow,

$$\begin{aligned}
\bar{\boldsymbol{Q}}_{ik} : \Phi^{L}_{i+1/2,j,k} &= \bar{\Phi}_{i,j,k} + 0.5\phi\left(r^{\xi}_{L,i,j,k}, \alpha_L, \beta_L\right)\Delta\Phi_{i-1/2,j,k}, \\
\bar{\boldsymbol{Q}}_{ki} : \Phi^{R}_{i+1/2,j,k} &= \bar{\Phi}_{i,j,k} - 0.5\phi\left(r^{\xi}_{R,i,j,k}, \alpha_R, \beta_R\right)\Delta\Phi_{i+3/2,j,k},
\end{aligned} \tag{3.64}$$

where α is the multi-dimensional restriction coefficient which determines the baseline region of MLP, and β is the local slope evaluated by a higher order polynomial interpolation. The interpolated values $\Phi^{L}_{i+1/2,j,k}$ and $\Phi^{R}_{i+1/2,j,k}$ are based on the final form of MLP. In Eq. (3.64), the coefficient α is introduced as follows

Along the ξ-direction, if $\Delta\Phi^{p}_{\xi} \geq 0$,

$$\begin{aligned}
\alpha_L &= g\left(\frac{2\max\left(1, r^{\xi}_{L,i,j,k}\right)\left(\bar{\Phi}^{\max}_{p,q,r} - \bar{\Phi}_{i,j,k}\right)}{\left(1 + \frac{\Delta\Phi^{q}_{\eta}}{\Delta\Phi^{p}_{\xi}} + \frac{\Delta\Phi^{r}_{\zeta}}{\Delta\Phi^{q}_{\xi}}\right)_{i,j,k}\Delta\Phi_{i+1/2,j,k}}\right), \\
\alpha_R &= g\left(\frac{2\max\left(1, r^{\xi}_{R,i,j,k}\right)\left(\bar{\Phi}^{\max}_{p,q,r} - \bar{\Phi}_{i,j,k}\right)}{\left(1 + \frac{\Delta\Phi^{q}_{\eta}}{\Delta\Phi^{p}_{\xi}} + \frac{\Delta\Phi^{r}_{\zeta}}{\Delta\Phi^{p}_{\xi}}\right)_{i+1,j,k}\Delta\Phi_{i+3/2,j,k}}\right),
\end{aligned} \tag{3.65}$$

where, $r^{\xi}_{L,i,j,k} = \frac{\Delta\Phi_{i+1/2,j,k}}{\Delta\Phi_{i-1/2,j,k}}$, $r^{\xi}_{R,i,j,k} = \frac{\Delta\Phi_{i+1/2,j,k}}{\Delta\Phi_{i+3/2,j,k}}$ and $g(x) = \max(1, \min(2, x))$. Along the η- and ζ-direction, the left and right values at the cell-interface can be calculated in the same way. With the β in the form of a third order polynomial and a fifth order polynomial, we finally obtain MLP3 and MLP5, respectively. For detailed explanation, see Ref. [42, 43].

3.4 Time integration methods

The semi-discretized form of the governing equations is considered as following form:

$$|\Omega_{i,j,k}|\frac{\partial \bar{\boldsymbol{W}}_{i,j,k}}{\partial t} = -\boldsymbol{R}_{i,j,k}\left(\bar{\boldsymbol{Q}}, t\right), \tag{3.66}$$

where $\boldsymbol{R}$ denote the residual vector,

$$\boldsymbol{R}_{i,j,k} = \sum_{m=1}^{6}\left\{\boldsymbol{H_c}\left(\bar{\boldsymbol{Q}}_{m,L}, \bar{\boldsymbol{Q}}_{m,R}, \boldsymbol{n}_m\right) - \boldsymbol{H_v}\left(\bar{\boldsymbol{Q}}_m, \nabla\bar{\boldsymbol{Q}}_m, \boldsymbol{n}_m\right)\right\}|e_m| - |\Omega_{i,j,k}|\boldsymbol{D}_{i,j,k}\left(\bar{\boldsymbol{Q}}_m\right). \tag{3.67}$$

Applying 2nd order backward Euler time integration method to Eq. (2.65) and rewrite governinig equation like a following form:

$$\frac{|\Omega_{i,j,k}|}{\Delta t}\left(\frac{3}{2}\Delta\left(\bar{\boldsymbol{W}}^{n+1}_{i,j,k}\right)_\tau - 2\bar{\boldsymbol{W}}^{n}_{i,j,k} + \frac{1}{2}\bar{\boldsymbol{W}}^{n-1}_{i,j,k}\right) + \frac{|\Omega_{i,j,k}|}{\Delta\tau}\boldsymbol{\Gamma}\Delta\left(\bar{\boldsymbol{Q}}_{i,j,k}\right)_\tau = -\boldsymbol{R}_{i,j,k}\left(\bar{\boldsymbol{Q}}^{n+1,m+1}, t^{n+1}, \tau^{m+1}\right), \tag{3.68}$$

where, $\Delta\left(\right)_\tau = \left(\right)^{m+1} - \left(\right)^{m}$. Here, n and m denote physical (t) and pseudo (τ) time step, respectively. Approximating $m+1$ step residual vector, Eq. (3.68) can be written as follows:

$$\frac{|\Omega_{i,j,k}|}{\Delta t}\frac{3}{2}\Delta\left(\bar{\boldsymbol{W}}^{n+1}_{i,j,k}\right)_\tau + \frac{|\Omega_{i,j,k}|}{\Delta\tau}\boldsymbol{\Gamma}\Delta\left(\bar{\boldsymbol{Q}}_{i,j,k}\right)_\tau + \frac{\partial\boldsymbol{R}_{i,j,k}}{\partial Q}\left(\bar{\boldsymbol{Q}}^{n+1,m}, t^{n+1}, \tau^{m}\right)\Delta\left(\bar{\boldsymbol{Q}}_{i,j,k}\right)_\tau = -\boldsymbol{R}_{i,j,k}\left(\bar{\boldsymbol{Q}}^{n+1,m}, t^{n+1}, \tau^{m}\right) - \frac{|\Omega_{i,j,k}|}{\Delta t}\left(\frac{3}{2}\bar{\boldsymbol{W}}^{n+1,m}_{i,j,k} - 2\bar{\boldsymbol{W}}^{n}_{i,j,k} + \frac{1}{2}\bar{\boldsymbol{W}}^{n-1}_{i,j,k}\right). \tag{3.69}$$

Defining right hand side of above equation as $\boldsymbol{R}^*$ and rearranging left hand side of above euqtion, Eq. (3.69) can be written as follows:

$$\left[\frac{3}{2}\frac{|\Omega_{i,j,k}|}{\Delta t}\frac{\partial\boldsymbol{W}}{\partial\boldsymbol{Q}} + \frac{|\Omega_{i,j,k}|}{\Delta\tau}\boldsymbol{\Gamma} + \frac{\partial\boldsymbol{R}_{i,j,k}}{\partial Q}\left(\bar{\boldsymbol{Q}}^{n+1,m}, t^{n+1}, \tau^{m}\right)\right]\Delta\left(\bar{\boldsymbol{Q}}_{i,j,k}\right)_\tau = -\boldsymbol{R}^*_{i,j,k}\left(\bar{\boldsymbol{Q}}^{m}, t^{n+1}, \tau^{m}\right), \tag{3.70}$$

where,

$$\boldsymbol{R}^{*}_{i,j,k}\left(\bar{\boldsymbol{Q}}^{m}, t^{n+1}, \tau^{m}\right) = \boldsymbol{R}_{i,j,k}\left(\bar{\boldsymbol{Q}}^{n+1,m}, t^{n+1}, \tau^{m}\right) + \frac{|\Omega_{i,j,k}|}{\Delta t}\left(\frac{3}{2}\bar{\boldsymbol{W}}^{n+1,m}_{i,j,k} - 2\bar{\boldsymbol{W}}^{n}_{i,j,k} + \frac{1}{2}\bar{\boldsymbol{W}}^{n-1}_{i,j,k}\right). \quad (3.71)$$

Note that $\Delta\left(\bar{\boldsymbol{W}}^{n+1}_{i,j,k}\right)_{\tau} = \frac{\partial \boldsymbol{W}}{\partial \boldsymbol{Q}}\Delta\left(\bar{\boldsymbol{Q}}_{i,j,k}\right)_{\tau}$. In case of steady calculation, Eq. (3.70) can be written by dropping physical time term;

$$\left[\frac{|\Omega_{i,j,k}|}{\Delta\tau}\boldsymbol{\Gamma} + \frac{\partial \boldsymbol{R}_{i,j,k}}{\partial Q}\left(\bar{\boldsymbol{Q}}^{m}, \tau^{m}\right)\right]\Delta\left(\bar{\boldsymbol{Q}}_{i,j,k}\right)_{\tau} = -\boldsymbol{R}_{i,j,k}\left(\bar{\boldsymbol{Q}}^{m}, \tau^{m}\right). \quad (3.72)$$

From the equations 3.70 or 3.72, we can calculate the difference of the primitive variable vector $\Delta\left(\bar{\boldsymbol{Q}}_{i,j,k}\right)$ by forward and backward sweeps.

Chapter 4

Validations

In this chapter, numerical simulations of some experiments are presented as a validation. Firstly, numerical simulations of steady cavitating flows around a cylinder mounted with a disk-shaped cavitator are carried out. And then we conduct an unsteady computation of ventilated cavitation in a gust flow. From the computations, we validate the flow solver used in this work by comparing the results with the experiments. As mentioned in section 2.2.3, both ideal gas and stiffened EOS are not appropriate since these EOSs do not generate accurate values near the saturated line. However, in the experiments presented here, the flow conditions are determined not to generate natural cavity for pure ventilated cavitating flows. Hence, in this chapter, we adopt the stiffened-gas model [25] for air-water two-phase flows, in order to save computational cost. Also, we employ the RoeM_N numerical flux scheme, the MLP5 interpolation for second-order spatial accuracy, the dual-time stepping method for unsteady computations, the LU-SGS for sub-iteration, and the $k - \omega$ SST model for turbulence effects.

4.1 Ventilated cavitating flows around a cylidnrical body with cavitator

We firstly simulate the ventilated cavitating flows around a cylindrical pipe with a cavitator. The computional results are compared with the experiment by Chungnam National University (CNU) [44, 7, 6].

4.1.1 Problem description

Figure 4.1 shows the test model used in the experiment, boundary conditions, and the grid system. As shown in the figure, a backward-truncated cone is adopted as a cavitator and connected to the cylindrical pipe with the diamter of 10 mm. For ventilation, the air is supplied through the pipe and injected into the water though the four holes in the experiment. To simulate the experiment in CFD, we determine the flow conditions based on the experiments, and summarize them in table 4.1. Air entrainment coefficient, C_Q and ventilated cavitation number, σ_c, the key parameters of ventilated cavitating flows, are defined as follows:

$$C_Q = \frac{\dot{Q}}{V_\infty d_c^2}, \tag{4.1}$$

$$\sigma_c = \frac{P_\infty - P_c}{1/2\rho_\infty V_\infty^2}, \tag{4.2}$$

where, $\dot{Q}$ and P_c are volumetric flow rate (m^3/s) and the pressure inside the ventilated cavity, respectively. For constant air-entrainment coefficient C_Q, the air-injection velocity is determined in the ventilation boundary condition to maintain constant volumetric flow rate $\dot{Q}$.

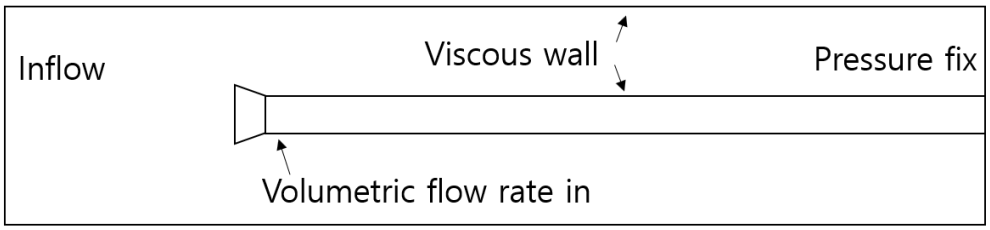

(a) Computational domain and boundary conditions

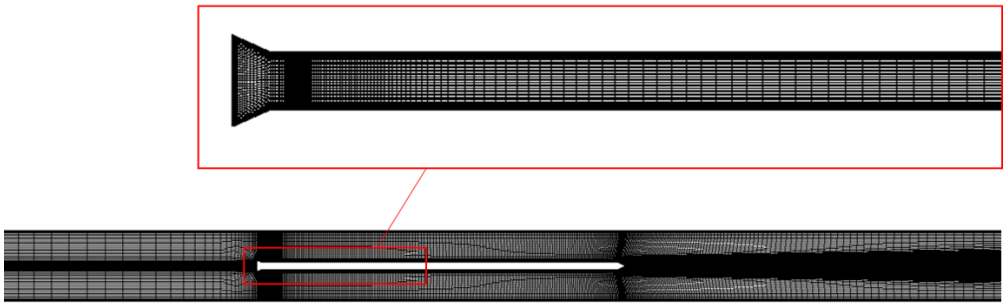

(b) Computational mesh

Figure 4.1: Boundary conditions and computational mesh.

Table 4.1: Flow conditions for ventilated cavitation.

Prameter	Value
Test section size	100 mm × 100 mm
Cavitator diamter, d_c	15.8 mm
Hole diamter, d_h	3 mm
Inflow velocity, V_∞	6 m/s
Inflow pressure, P_∞	85,000 Pa
Inflow density, ρ_∞	999 kg/m^3
Air entrainment coefficient, C_Q	0.2 to 1.2

Table 4.2: Comparison of results with diffrerent types of ventilation hole.

Hole & mesh types	Cav. number (σ_c)	P_{c1} (Pa)	P_{c2} (Pa)
Circular hole	0.598	74,236	82,546
Square hole	0.603	74,077	82,393
Band: Fine (2.61 M cells)	0.598	74,200	82,477
Band: Medium (1.77 M cells)	0.608	73,581	82,424
Band: Coarse (1.29 M cells)	0.601	73,974	82,438
Experiment (CNUCT)	0.600	73,800	81,900

4.1.2 Numerical results

Figure 4.2 shows the grid systems with different types of ventilation hole, and the corresponding volume fraction contours of air. As mentioned earlier, the test model used in the experiment has four circular holes for ventilation. Cao *et al.* [21] simplified the six circular holes to an annular band for the quality of the structured grid used in their computations. Ahn *et al.* [7] tested the effects of air injection position and direction in their experiment. They reported that the position and direction has a marginal effect on the formation of supercavity, provided that the air is injected close enough to the cavitator. Taking these into consideration, we test three different types of ventilation hole shown in Fig. 4.2, and perform the grid refinement test. The test results are summarize in table 4.2. As shown in the table, whole types of ventilation hole yield almost identical cavitation number and cavity pressure. It is very difficult to implement circular geometries in stuructred mesh. Therefore, in this paper, we adopt the annular band type of ventilation hole for mesh quality and computational efficiency. Also, we adopt the medium mesh thoughout computations since it provides a sufficiently accurate result.

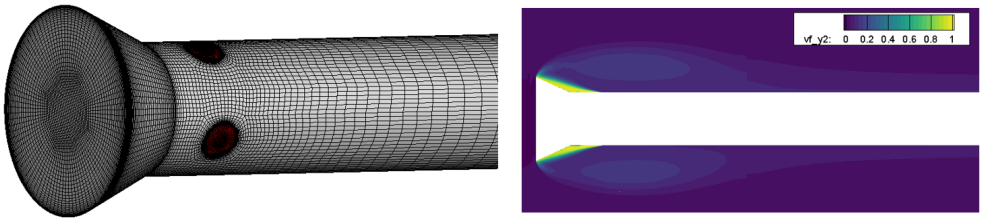

(a) Circular holes ($\sigma_c = 0.598$)

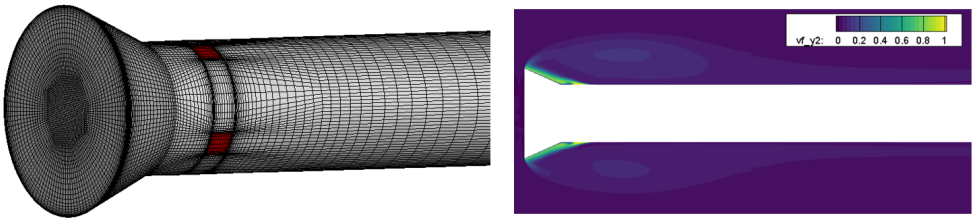

(b) Square holes ($\sigma_c = 0.603$)

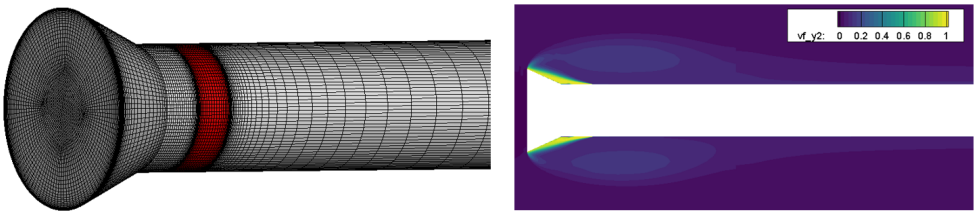

(c) Annular band ($\sigma_c = 0.608$)

Figure 4.2: Grid systems and volume fraction of air with different types of ventilation hole ($C_Q = 0.04$).

Figure 4.3 shows the computational results and compares those with the experiment by CNUCT [44, 7, 6]. Due to the limitation of RANS simulation, the cavity shedding is not properly captured by the computation until $C_Q = 0.12$, and the results show steady re-entrant jet flow only, as shown in Fig. 4.4. When the air-entrainment coefficient is 0.12, the re-entrant jet flow vanishes and the cavity turns into clear supercavity with twin-vortex flow shown in Fig. 4.4. In this case, the computational result shows similar cavity shape to the experiment except the small-scale flow physics. Figure 4.6 shows the ventilated cavity pressure along the cavitation number. The cavity pressure measured by the sensor 1 (P_{c1}) is gradually increased as the cavitation number decreases (or the air-entrainment coefficient, C_Q, increases). On the other hand, the pressure measured by sensor 2 is almost identical until the cavitation number is lower than 0.47 (or C_Q is greater than 0.08), since the sensor is located outside the cavity. When the cavitation number is about 0.4 (or $C_Q = 0.10$), the cavity shedding occurs in front of the pressure sensor 2. In other words, locally high-pressure fluid behind the cavity closure is shedded and influences the sensor. This may a cause of the high-pressure value at $C_Q = 0.10$. Figure 4.7 compares the normalized geometric parameters (cavity length and maximum cavity thickness) between the computational results and the analytic solution. The analytic solution is obtained from the experimental data by CNUCT [44, 7, 6] and the potential-based panel method developed by Kim and Ahn [12]. The figure confirms that the geometric parameters from computational result and analytic solution are in good agreement.

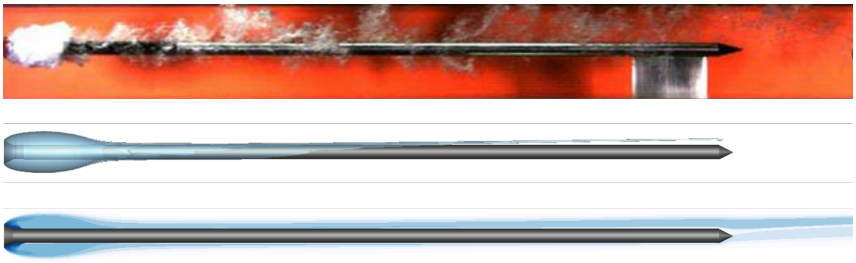

(a) $C_Q = 0.06$

(b) $C_Q = 0.08$

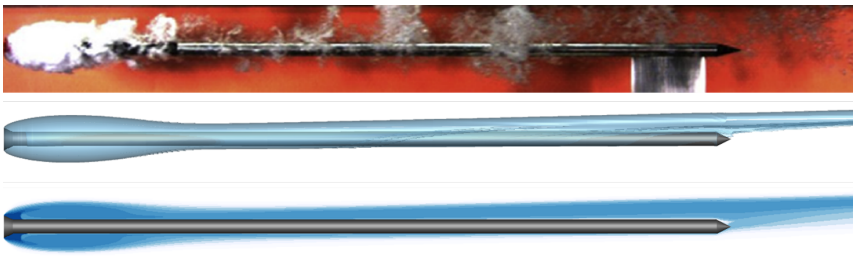

(c) $C_Q = 0.10$

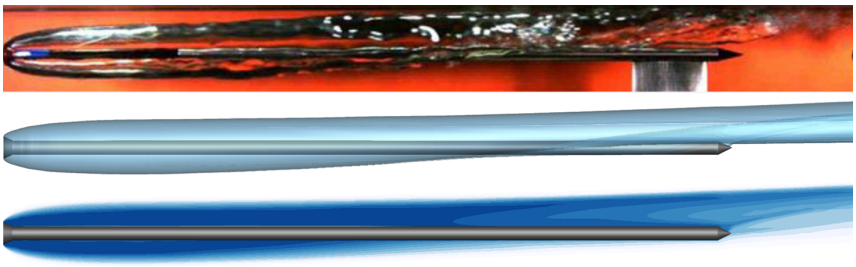

(d) $C_Q = 0.12$

Figure 4.3: Cavity shapes corresponding to air-entrainment coefficient C_Q (air volume fraction is 0.5 for each iso-surface).

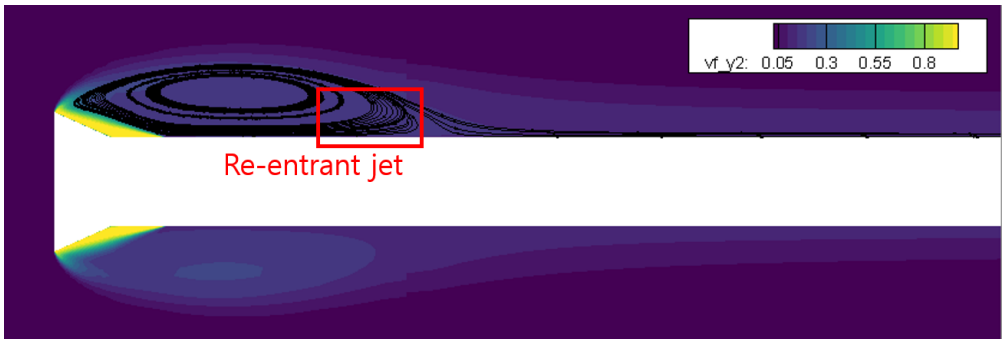

Figure 4.4: Re-entrant jet flow.

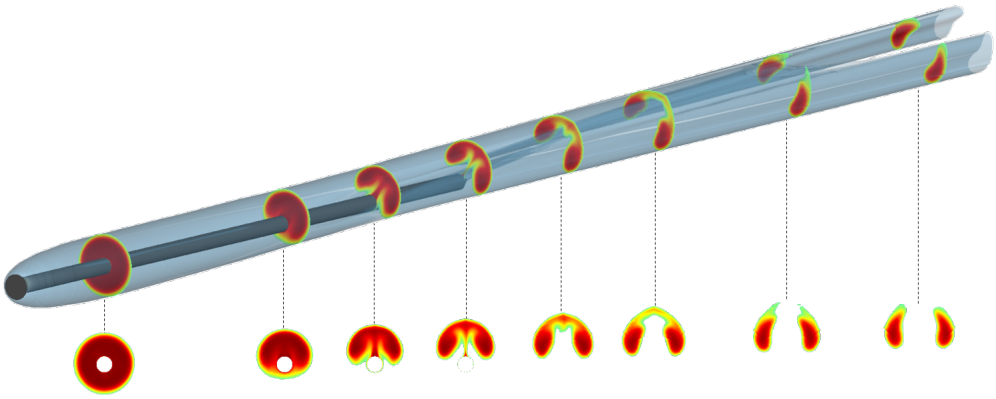

Figure 4.5: Clear supercavity with twin-vortex flow.

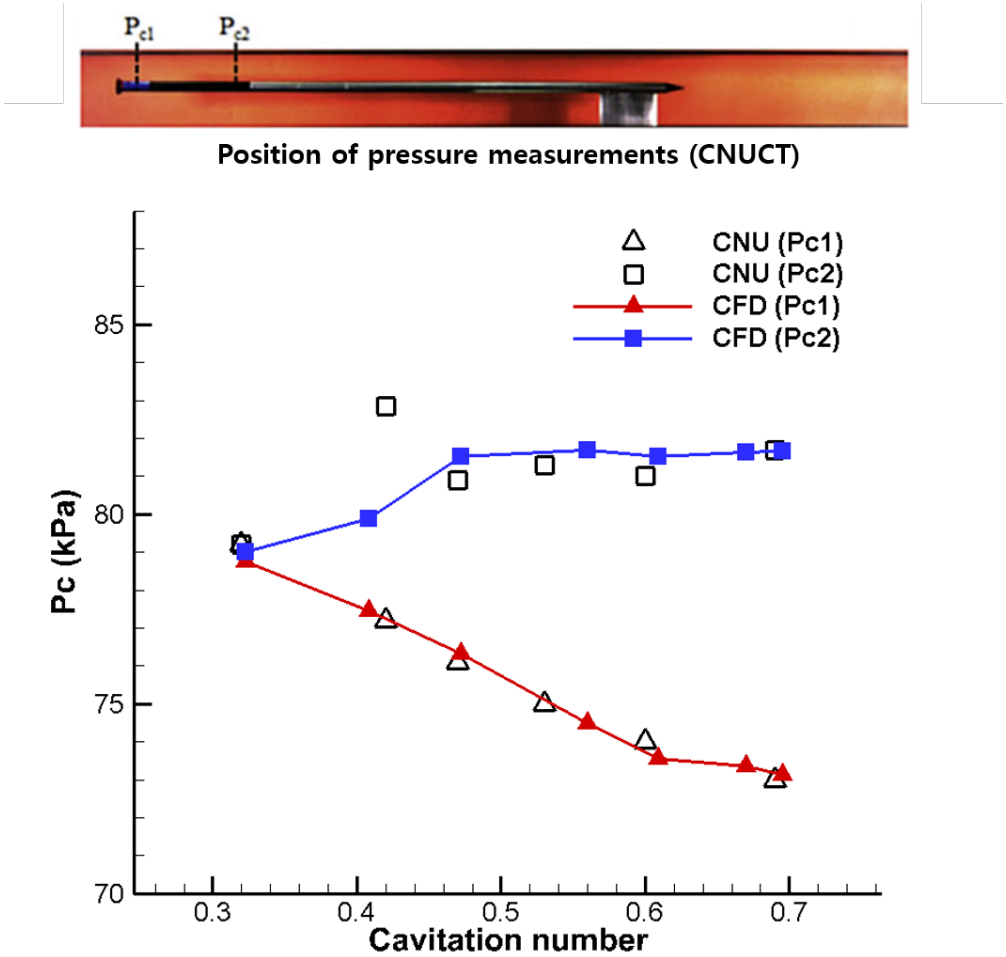

Figure 4.6: Comparison of cavity pressures along the cavitation number.

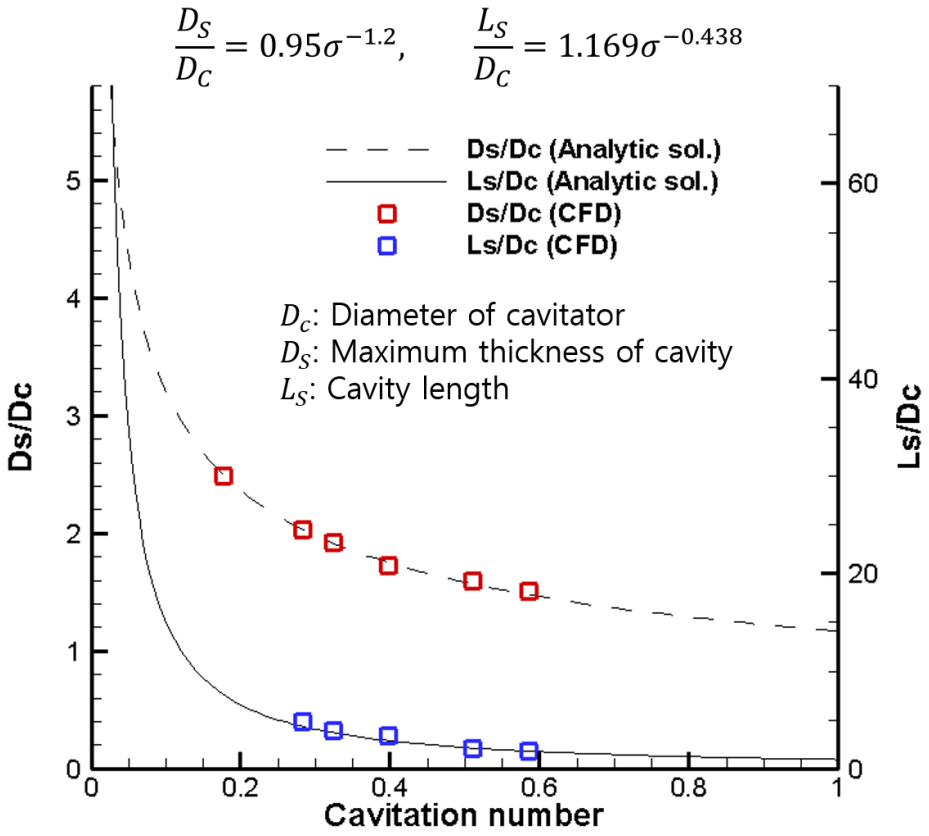

Figure 4.7: Comparison of geometric parameters of supercavity.

Overall, the computation results show a good agreement with the experiment [44, 7, 6]. However, the detailed flow physics is quite different between the computation and the experiment as mentioned above. Since the computations perfromed in this work are based on the Reynolds-Averaged Navier-Stokes (RANS) equation, detailed flow structures such as shedding vortices and toroidal cavities are not observed. Detached Eddy Simulation (DES) or Large Eddy Simulation (LES) might be a possible candidate to overcome this weak capability problem, thus we plan to perform DES computations as a future work.

4.2 Ventilated cavitation in unsteady gust flow

As another validation, ventilated cavitation in a gust flow is considered. The computional results are also compared with the experiment by Saint Anthony Falls Laboratory (SAFL) at University of Minnesota [6, 45, 46, 47]. Underwater vehicles traveling near the water surface can encounter unsteady flows under waves [47]. This unsteady flows might cause unwanted planing forces to the vehicles. Therefore, experiments have been conducted to investigate the effects of a periodic gust flow on supercavities.

4.2.1 Problem description

Figure 4.8 presents a schematic view of the computational domain, boundary conditions, and the mesh system. The forward-facing cavitator with the diameter of 20 mm is connected to the cylinder. Due to the lack of detailed information about the target geometry, we generate the computational mesh by referring to the geometry in the experiment [6]. In the experiment, two oscillating NACA0020 hydrofoils are placed to generate periodical gust flows. It is very difficult to implement the gust generator in CFD, thus Huang *et al.,* [46] employed an inflow boundary condition in which a vertical velocity component fitted to a sinusoidal function is added to the freestream velocity. The vertical velocity component $V_g(t)$ is defined as

$$V_{\mathrm{g}}(t) = V_{\mathrm{gmax}} \sin(2\pi f_{\mathrm{g}} t), \tag{4.3}$$

where V_{gmax} is the maximum vertical velocity (or amplitude), and f_g is the frequency of the gust flow. For ventilation, air is supplied through the ventilation holes covered by a shroud [6]. Based on the experiment by SAFL, we determine the flow conditions summarize them in table 4.3.

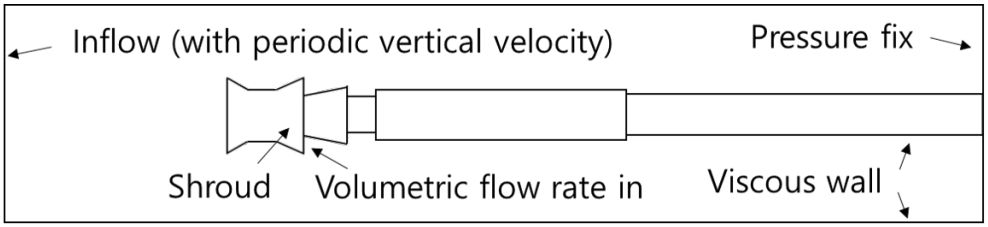

(a) Computational domain and boundary conditions

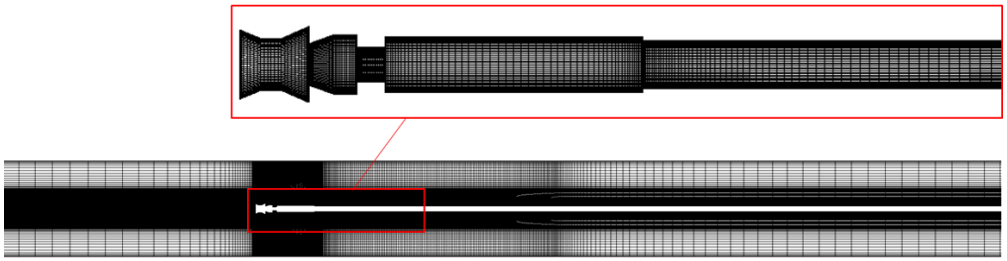

(b) Computational mesh

Figure 4.8: Boundary conditions and computational mesh.

Table 4.3: Flow conditions for ventilated cavitation in gust flow.

Prameter	Value
Test section size	190 mm × 190 mm
Cavitator diamter, d_c	20 mm
Inflow velocity, V_∞	8.5 m/s
Maximum vertical velocity, V_{gmax}	0.448 m/s
Gust frequency, f_{g}	10 Hz
Inflow pressure, P_∞	65,500 Pa
Inflow density, ρ_∞	997 kg/m^3
Air entrainment coefficient, C_Q	0.15

Table 4.4: Grid refinement test for steady ventilation.

Grid	# of cells	σ_{steady}	err_σ, %	$L_{1/2}$	err_L, %	D_{max}	err_D, %
EXP		0.2	-	204 mm	-	62 mm	-
G1	1.52 M	0.208	4	195.8 mm	4	59.0 mm	4.8
G2	1.74 M	0.191	4.5	199.2 mm	2.4	60.8 mm	1.9
G3	2.10 M	0.194	3	202.4 mm	1.3	61.4 mm	1.5
G4	2.52 M	0.204	2	202.7 mm	0.6	61.2 mm	1.3

4.2.2 Numeriacl results

We first carry out a grid refinement study by computing a vertilated cavitation in a steady flow, not an unsteady gust flow (i.e. the vertical component of freestream velocity $V_\mathrm{g}(t) = 0$). From the test results, for each mesh, the cavitation number, σ_steady, the maximum cavity thickness, and the half length of the cavity shown in Fig. 4.9 are compared with those in the experiment [46], and summarized in table 4.4. From the grid refinement study, we adopt G3 grid throughout computations for reliable and accurate computations. Figure 4.10 shows snap shots of the ventilated cavity oscillating during the gust cycle. The geometric parameters of the cavity defined in Fig. 4.9 are normalized by the wavelength $\lambda_\mathrm{g} = V_\infty/f_\mathrm{g}$. The normalized parameters are then compared with the experiment as shown in Fig. 4.11. The comparison result confirms that that the computational results show a good agreement with the experiment.

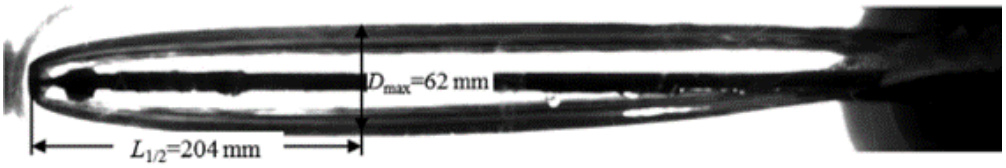

(a) EXP (SAFL)

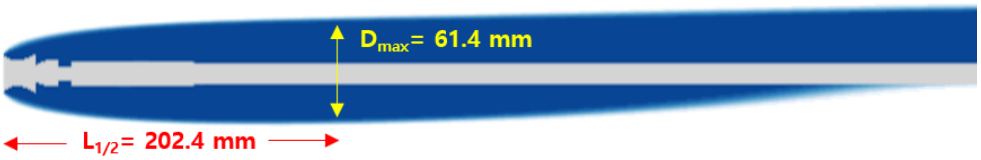

(b) CFD

(c) Geometric parameters

Figure 4.9: Ventilated cavity in steady flow and geometric parameters.

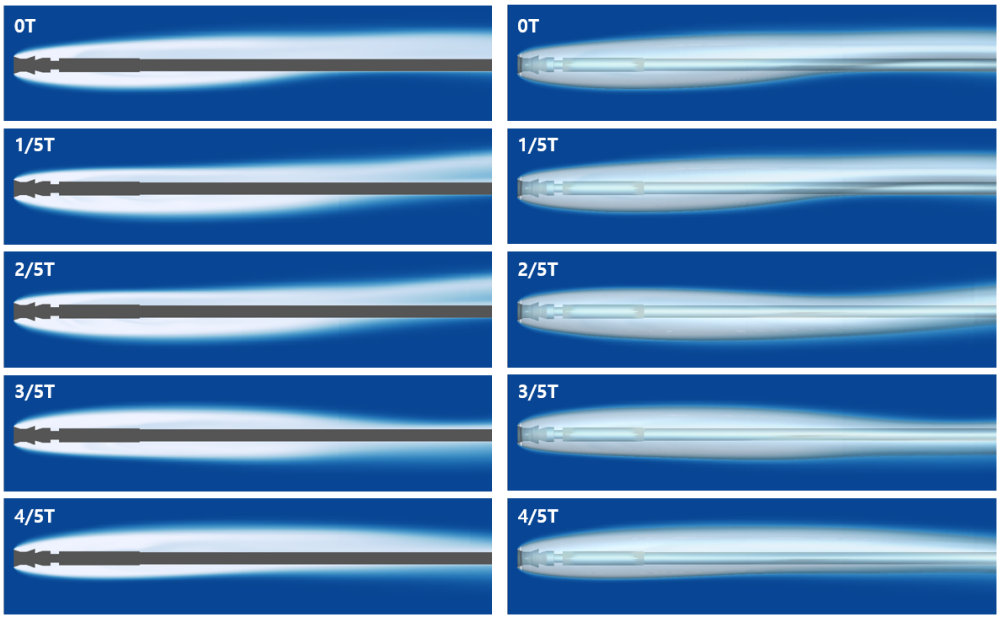

Figure 4.10: Volume fraction of ventilated air during the gust cycle.

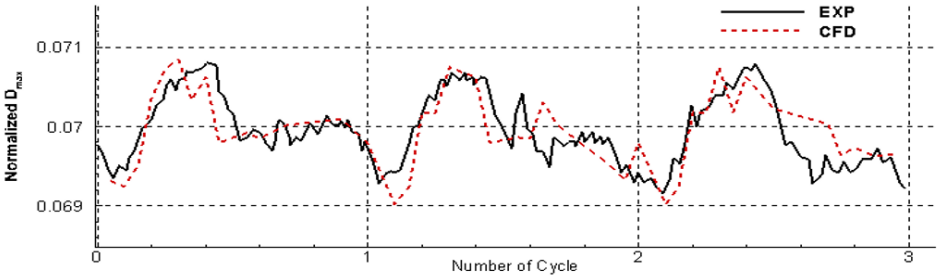

(a) Normalized D_{max} (RMS error 0.3%)

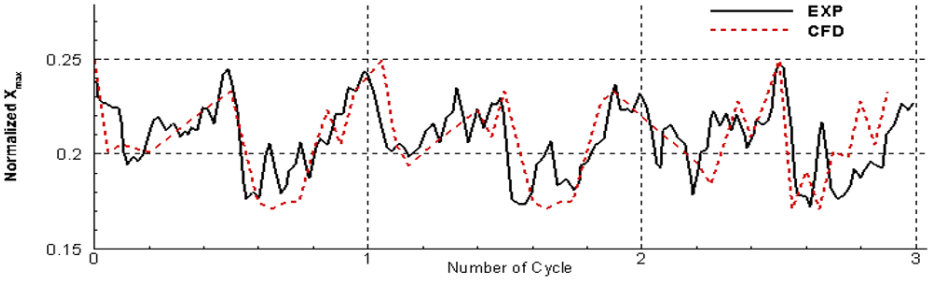

(b) Normalized X_{max} (RMS error 1.7%)

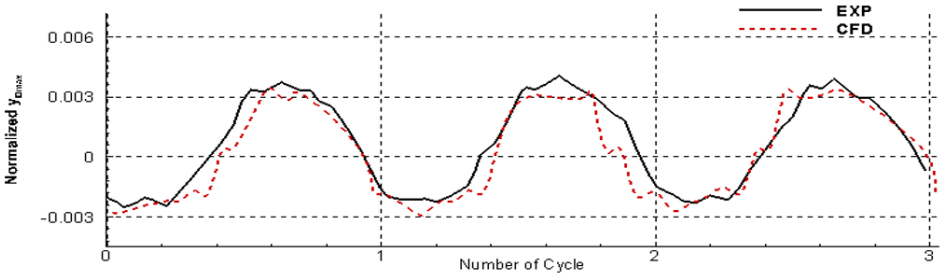

(c) Normalized Y_{max} (RMS error 0.7%)

Figure 4.11: Geometric parameters of the cavity during the gust cycles.

Chapter 5

Supercavitating Flows Around an Underwater Vehicle

In this chapter, computations of ventilated supercavitating flows around a three-dimensional underwater vehicle are carried out. Based on the computational results, we investigate the flow and hydrodynamic characteristics of the vehicle including the control fins. Unlike the cavitating flows presented in the validation chapter, the vehicle is sufficienctly fast to generate natural cavities behind the control fins and the base. Hence, we should employ the IAPWS97 formulation [26] for water since the stiffened EOS are not appropriate near the saturated line. Also, in this chapter we employ the AUSMPW+_N [24] numerical flux scheme, the MLP5 interpolation for second-order spatial accuracy, the dual-time stepping method for unsteady computations, the LU-SGS for sub-iteration, and the $k - \omega$ SST model for turbulence effects.

Table 5.1: Normalized geometric parameters of the vehicle.

Normalized prameter	Value
Body length, L/D_C	45.7
Maximum body diamter, D/D_C	3.3
Control fin span, L_F/D_C	2.35

5.1 Problem description

Figure 5.1 shows the grid system and boundary conditions applied. The target vehicle geometry, presented in Fig. 5.1a, is selected by referring a study by Kim *et al.* [23]. As shown in the figure, the vehicle has the disc-shaped cavitator and the four control fins with their own number. Some geometric parameters normalized by the cavitator diameter D_C are shown in Fig. 5.2, and summarized in table 5.1. For more detailed information of the geometry, see [23]. In order to obtain a reliable grid system, we conduct a grid refinement test with three different grid system, namely, coarse, medium, and fine meshes. Figure 5.3 shows the cavity interface for each mesh at $V_\infty = 70m/s$ and $\mathrm{C_Q} = 0.8$. Each interface is compared with that of fine mesh as in table 5.2. From the grid refinement test, we adopt the medium one throughout compurations since the mesh can yiled reliable solution. The computations are performed under various freestream velocities, air-entrainment coefficients ($\mathrm{C_Q}$), and angles of attack. For each computation, hydrodynamic characteristics are also considered to show the effects of cavitating flow on the hydrodynamic forces. Steady computations are performed firstly, and then unsteady computations are followed to show the time-dependent characteristics of the cavitating flow and the hydrodynamic forces.

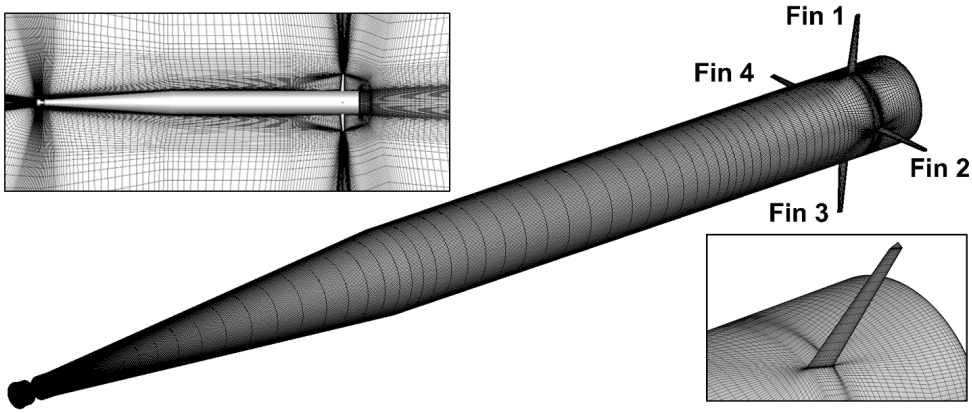

(a) Grid system

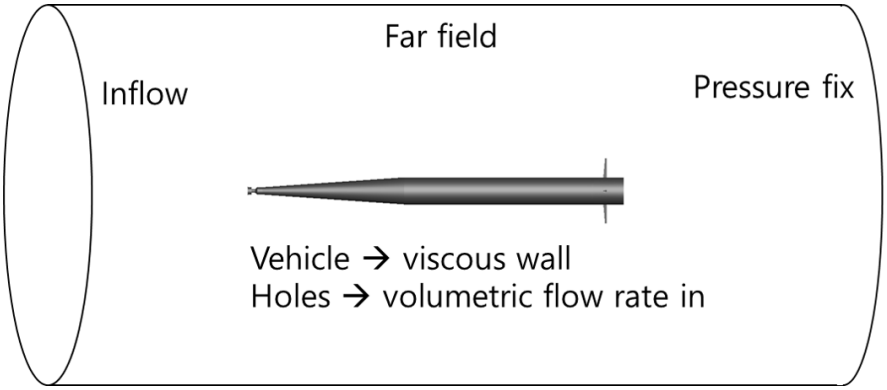

(b) Boundary conditions

Figure 5.1: Grid system and boundary conditions.

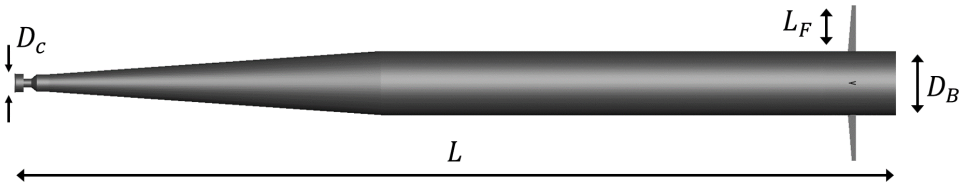

Figure 5.2: Geometric parameters of the vehicle.

(a) Cavity shape (medium mesh)

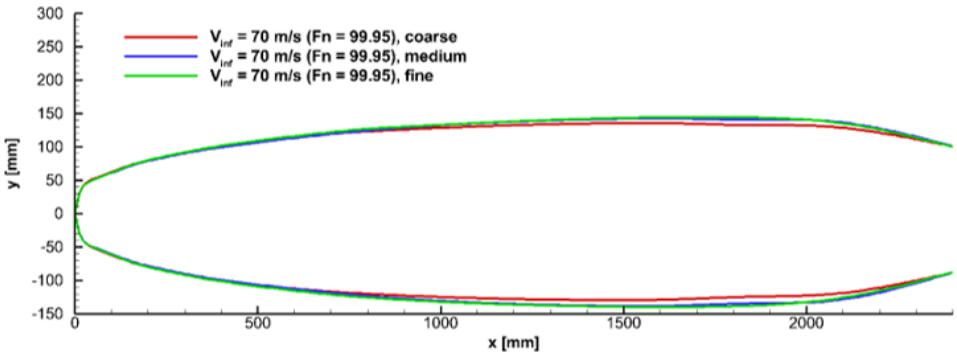

(b) Comparison of the cavity interfaces (cavity volume fraction is 0.5)

Figure 5.3: Grid refinement test ($V_\infty = 70m/s$ and $C_Q = 0.8$).

Table 5.2: Grid refinement test for underwater vehicle.

*Err $= \frac{1}{n}\Sigma\lvert\frac{Y_{fine}-Y}{Y_{fine}}\rvert$	Coarse grid (2.28 M cells)	Medium grid (4.77 M cells)	Fine grid (5.65 M cells)
Error (%)	3.75	1.25	-

5.2 Effects of freestream velocity

Firstly, computations of supercavitating flows around the vehicle are performed under various freestream velocity (or vehicle speed) V_∞. As in the Eq. 4.1, the air-entrainment coefficient C_Q depends on the freestream velocity. Hence, to keep the ventilation rate constant, the air-entrainment coefficient should be varied slightly according to the velocity. Taking this into consideration, we determine the flow conditions and summarize some of them in table 5.3.

As mentioned earlier, natural cavitation occurs around the body, the control fins and the base, due to sufficiently high speed. As a result, the cavity covering the vehicle body and the control fins consists of the natural and ventilated cavities. Since the homogeneous mixture model with mass fraction of air is adopted for the governing equations, these three-phase mixture flows can be described as shown in Fig. 5.4.

As the freestream velocity increases, the cavity evolves from the partial cavitation state to the supercavitation state as shown in Fig. 5.5. Due to the gravity, the buoyant force lifts the cavity upward, causing asymetric cavity shapes at relatively low freestream velocities. However, the influence of the buoyant force is weakened with increasing freestream velocity, and thus the cavity shape gradually becomes axi-symmetric. The cavity length around the afterbody (the control fins and the base) is gradually increased with the freestream valocity, and suddenly shortened as the partial cavity grows and passes through the afterbody. After the cavity covers entire body, the cavity gradually becomes longer again as the freestream speed increases.

While the ventilated cavity passes through the afterbody, the flow physics change significantly as shown in Fig. 5.6. In the partial cavitation state (i.e. $V_\infty < 65$ m/s), the ventilated cavity breaks up near the cavity closure and

Table 5.3: Freestream velocities and corresponding air-entrainment coefficients.

Freestream vel., V_∞	Air-entrainment coeff., C_Q	Angle of attack, α
30 m/s	1.870	
50 m/s	1.120	
60 m/s	0.933	0°
70 m/s	0.800	
80 m/s	0.700	

flows along the body surface. As the water and ventilation air passes through a control fin, the water pressure falls much more than the air pressure, causing the air to be lifted up behind the fin. Some fraction of the ventilated cavity is then bifurcating side by side along the separation region behind the fin, but the other fraction is lifted up behind the separation region, as if it is spouted. This situation is depicted in Fig. 5.7. At the freestream velocity of 65 m/s, however, the ventilated cavity lifted up behind the fin is detached from the cavity behind the base, causing separated ventilated cavity closures as shown in Fig. 5.6. Ventilated gas loss occurs from the each cavity closure. This separated closures make the cavity behind the base short.

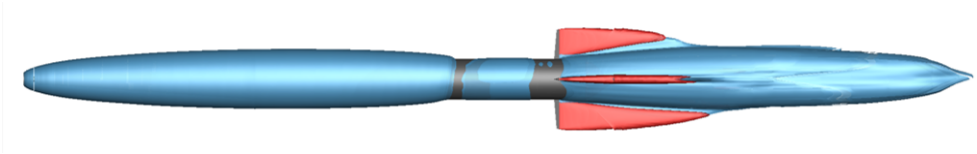

(a) Natural (red) and ventilated (blue) cavities

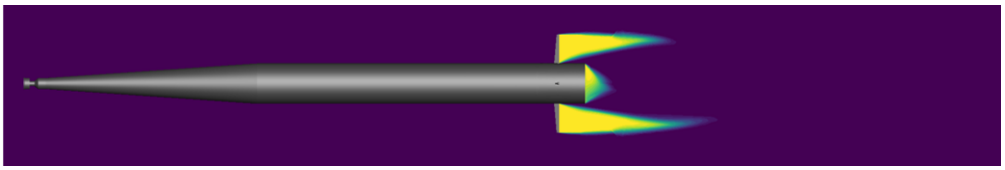

(b) Natural cavity

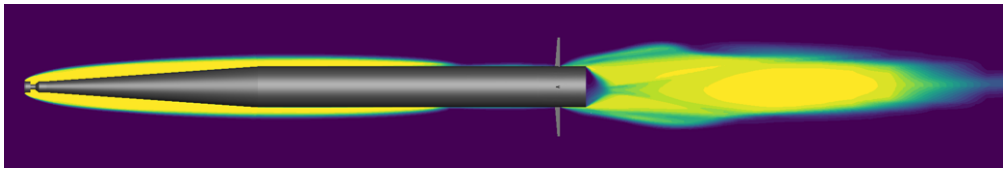

(c) Ventilated cavity

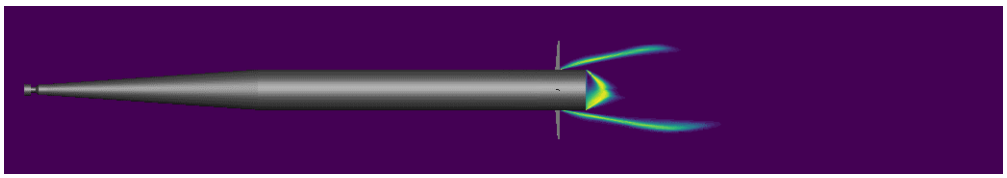

(d) Mixing zone (where both cavities coexist.)

Figure 5.4: Example of cavitating flow around the vehicle ($V_\infty = 60m/s$).

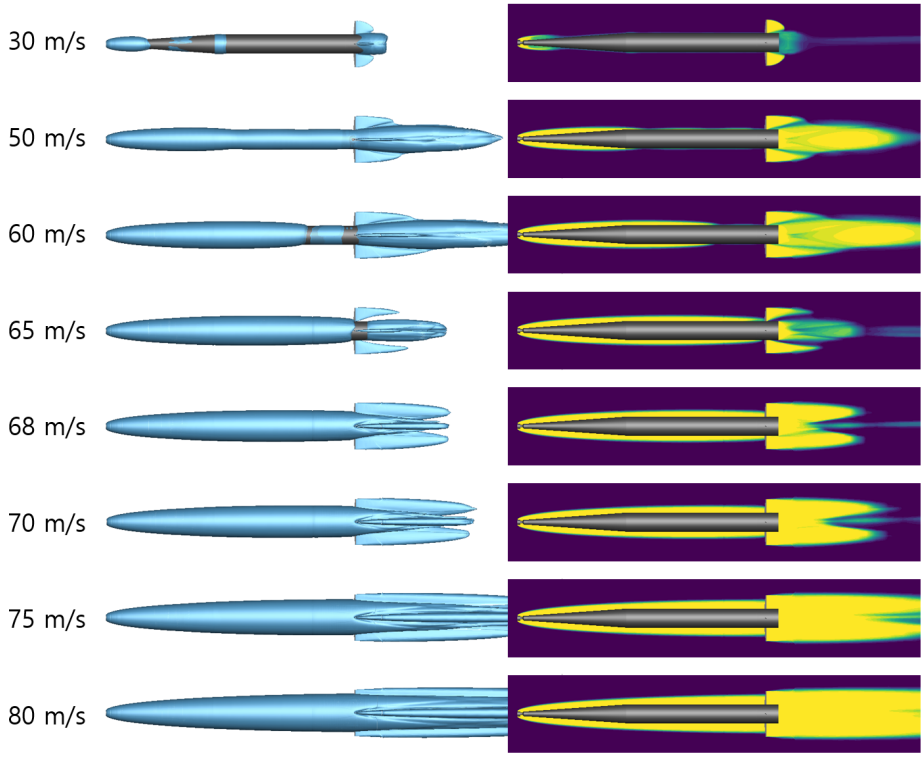

Figure 5.5: Cavitating flows around the vehicle under different freestream speeds.

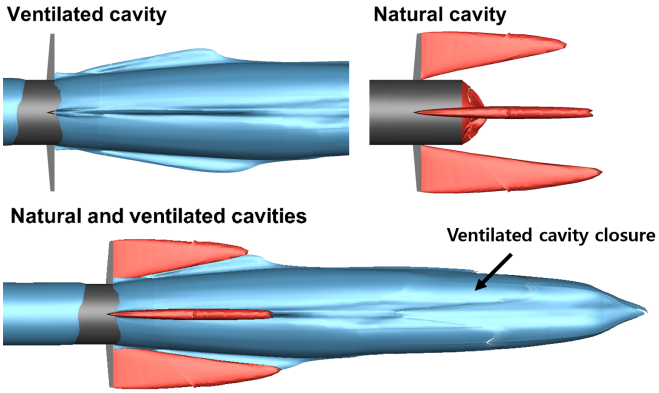

(a) $V_\infty = 55$ m/s

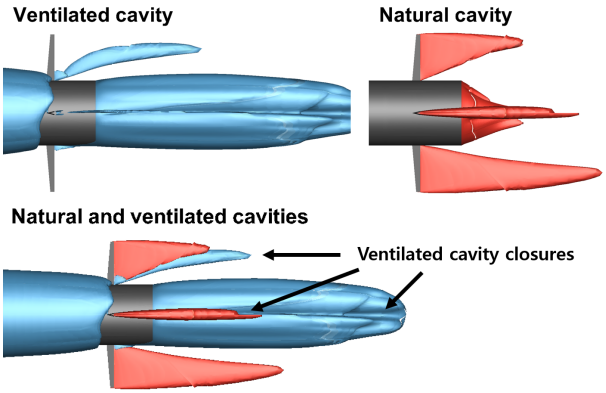

(b) $V_\infty = 65$ m/s

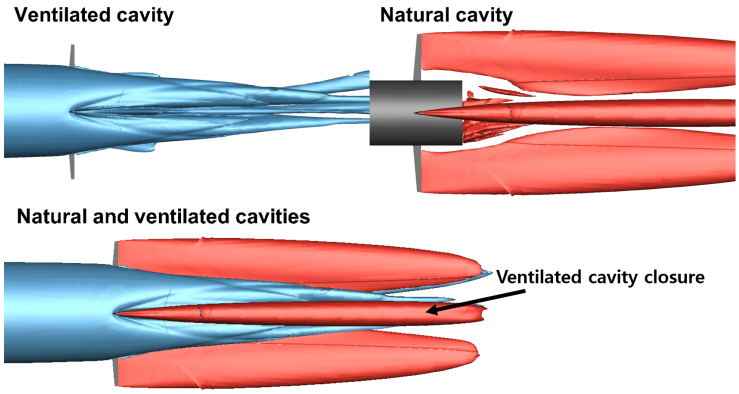

(c) $V_\infty = 70$ m/s

Figure 5.6: Natural and ventilated cavities depending on freestream velocity.

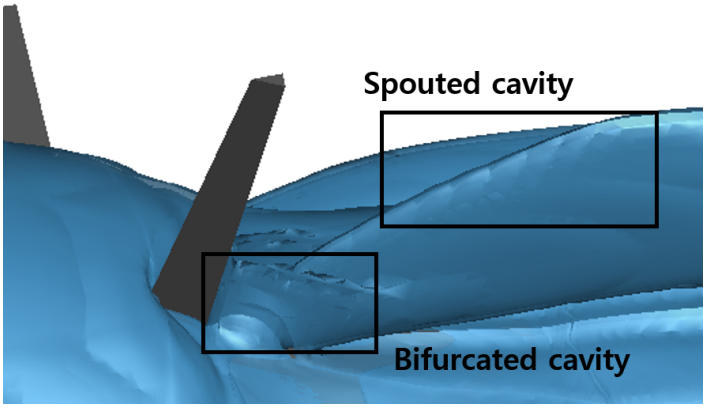

(a) Bifurcated and spouted cavity

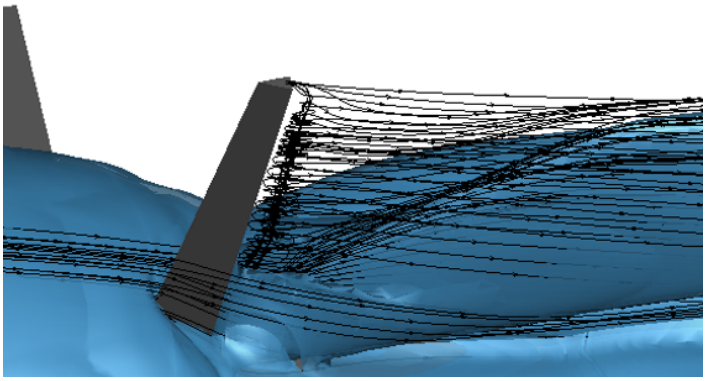

(b) Cavity and streamlines

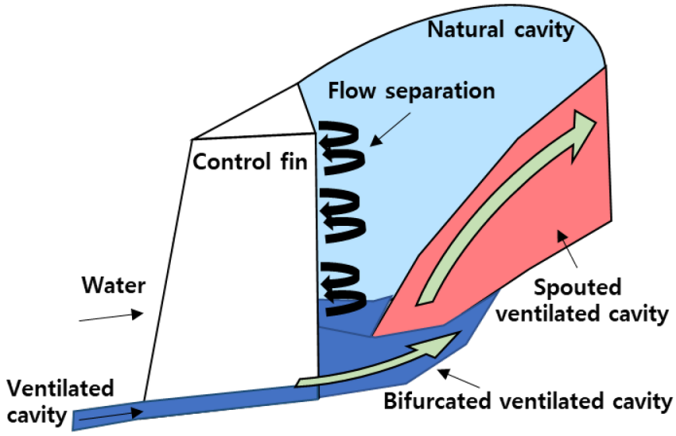

(c) Schematic view

Figure 5.7: Ventilated cavity around a control fin

5.2.1 Hydrodynamic characteristics: drag

Figure 5.8 summarizes the drag coefficients of the control fins and the body with different freestream velocities. The drag coefficient C_D is defined as

$$C_D = \frac{\text{Drag}}{1/2\rho_\infty V_\infty^2 S}, \tag{5.1}$$

where S denotes the planform area for the control fins and the maximum cross-sectional area for the body including the cavitator. As shown in the figure, the drag coefficients of the control fins decrease drastically when the cavity passes through the fins (from 64 m/s to 68 m/s), and then gradually decrease since the cavity covers a greater part of the fin surface. The coefficient of the body gradually decreases as the cavity covers a greater part of the body surface. Due to the buoyant force, the cavity is shifted upward as mentioned above, covering a greater part of the fin 1 than that of the fin 3. Thus, the fin 1 yields slightly lower drag coefficient than the fin 3, the lower vertical fin.

Figure 5.9 shows the drag behavior of the vehicle with different freestream velocities. Overall, the drag increases with the freestream velocity. When the velocity is lower than 50 m/s, a part of the head is contacted to the water, causing relatively high pressure acting on the head. As shown in the Fig. 5.10, the pressure acting on the head induces drag force, and the drag suddenly falls since the head is enclosed by the ventilated cavity at $V_\infty = 50$ m/s. Without the control fins, the drag acting on the body gradually increases with the freestream velocity. When the velocity reaches 70 m/s, the friction drag (difference between the red and the blue lines in Fig. 5.9) becomes insignificant since the body is contacted to the cavity (air), not water. The total drag of the vehicle falls again when the freestream velocity is 68 m/s, since the cavity reaches the control fins and encloses a part of the fin. Also, the fin drag (difference between the black and the red lines in Fig. 5.9) is gradually decreased for $V_\infty > 65$ m/s because

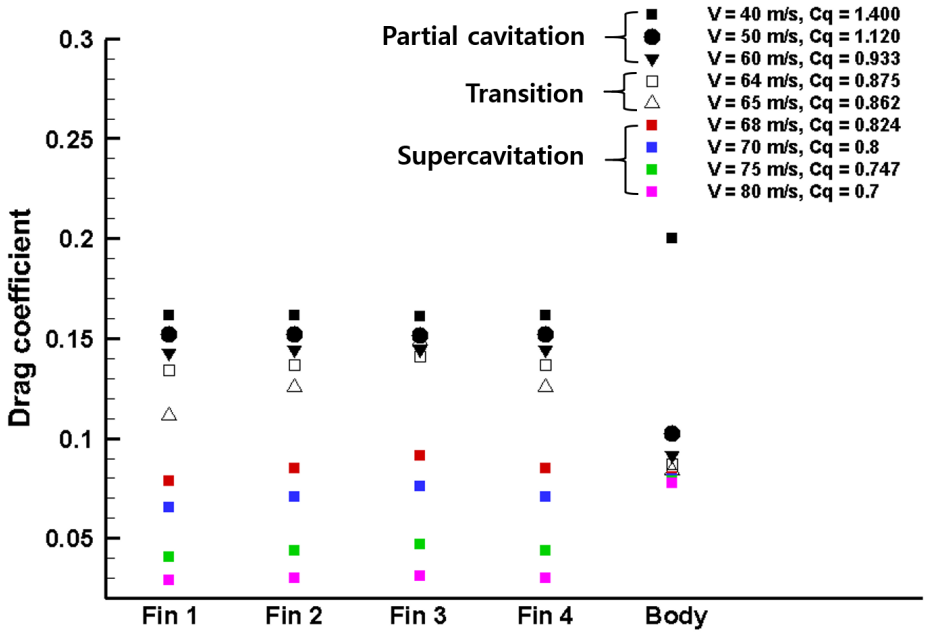

Figure 5.8: Drag coefficients of the control fins and the body depending on the freestream velocity.

the cavity covers a greater part of the fins with increasing velocity. If it was a single phase flow, the drag should be proportional to cubic of the freestream velocity (due to the change of dynamic pressure into static pressure in front of the cavitator and the fins). However, the characteristics of multi-phase flow cause this non-linear features of the drag force acting on the vehicle. The results confirm that the proper computation of the cavitating flow around a vehicle is essential for predicting the vehicle's behavior.

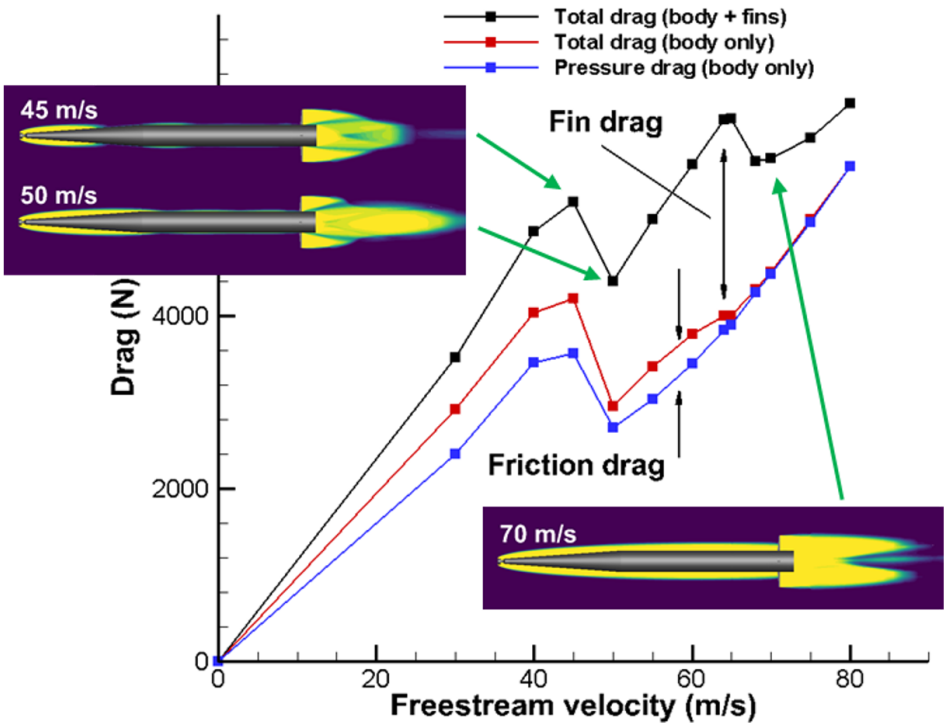

Figure 5.9: Drag force acting on the vehicle depending on the freestream velocity.

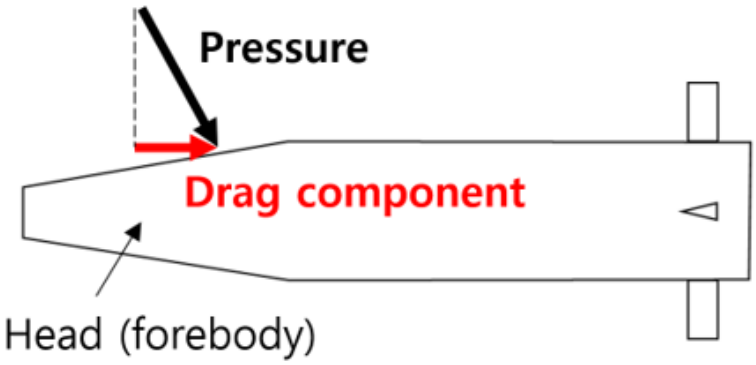

Figure 5.10: Schematic view of the pressure acting on the head.

5.2.2 Hydrodynamic characteristics: lift

Figure 5.11 summarizes the lift coefficients of the control fins and the body, with different freestream velocities. The lift coefficient $\mathrm{C_L}$ is defined as

$$\mathrm{C_L} = \frac{\mathrm{Lift}}{1/2\rho_\infty \mathrm{V}_\infty^2 \mathrm{S}}, \tag{5.2}$$

where S, like in the definition of the drag coefficient (Eq. 5.1), denotes the planform area for the control fins and the maximum cross-sectional area for the body including the cavitator. For sufficiently low speeds ($V_\infty < 70$ m/s), as shown in Fig. 5.11, lift force is generated by the control fins and the body due to the cavity being lifted up by the buoyant force, even though the angle of attack is zero. For the horizontal fins (fin 2 and 4), as shown in Fig. 5.12, vertical flow induced by the shifted cavity generates the lift force as if there is non-zero angle of attack. Far from the body, the influence of the cavity is weakened and the local flow direction becomes almost identical to the flow direction. In the case of the vehicle body, the asymmetric cavity covers a greater area of the upper surface of the body. Thus the local pressure at a part of the lower surface exposed to water increases significantly, generating the lift force acting to the body. When the freestream velocity increases, the buoyant effect becomes insignificant as mentioned earlier, and thus the lift coefficient decreases as shown in Fig. 5.11.

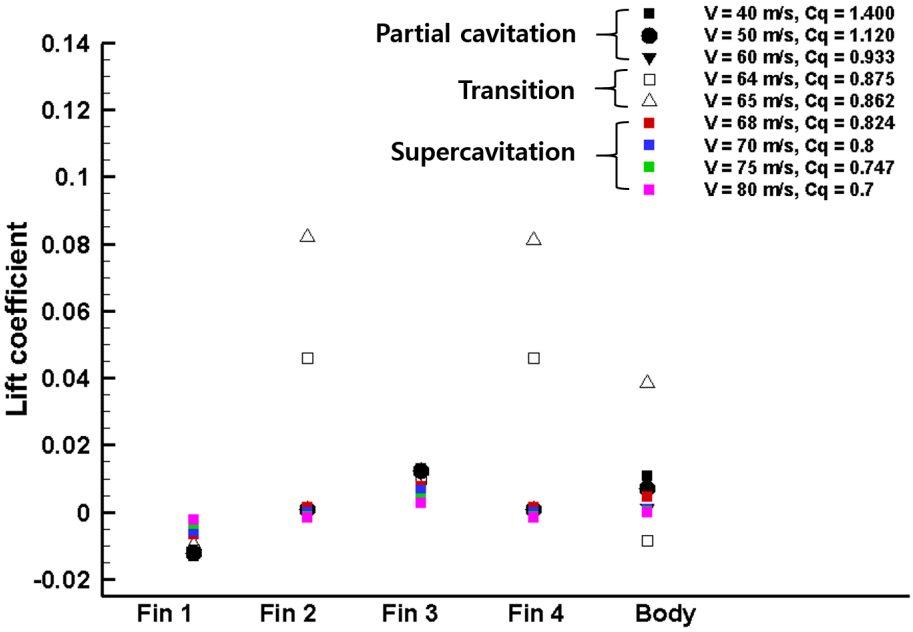

Figure 5.11: Lift coefficients of the control fins and the body depending on the freestream velocities.

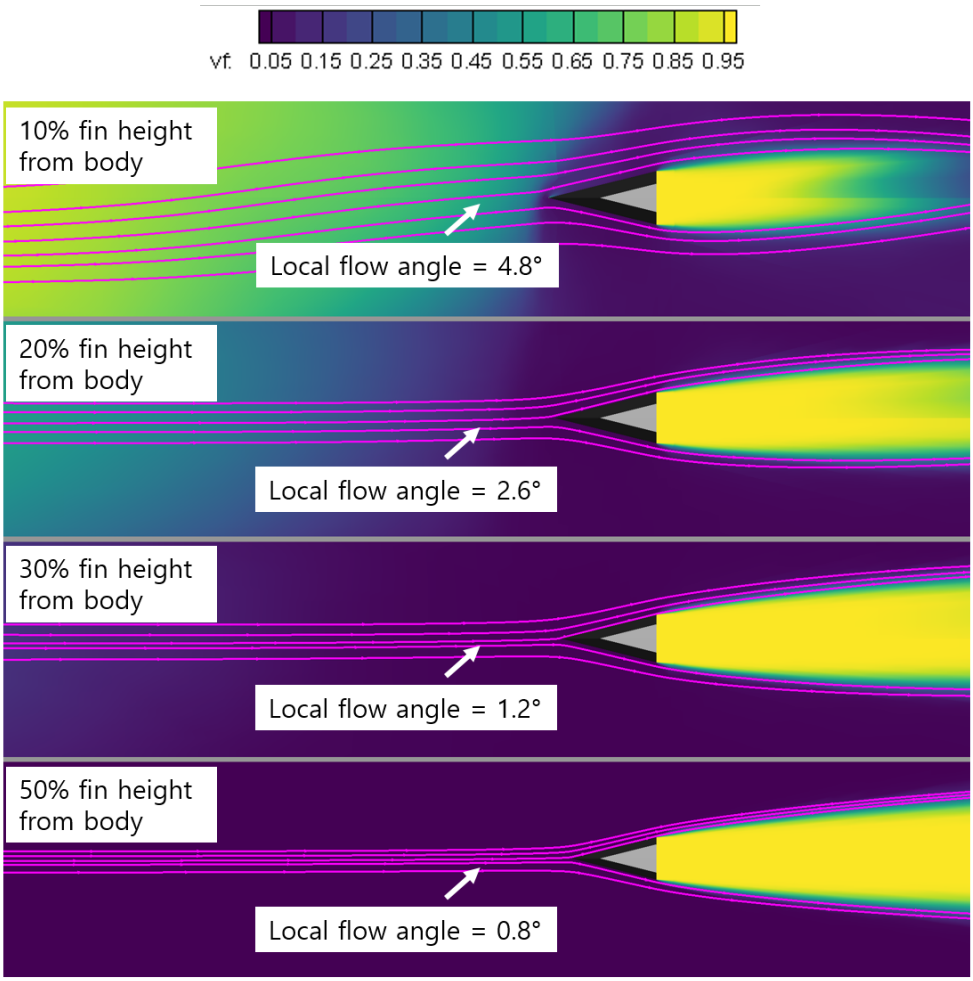

Figure 5.12: Local flow angles induced by the ventilated cavity.

5.2.3 Hydrodynamic characteristics: pitching moment

Figure 5.13 presents the pitching moment coefficient of the control fins, the body, and the entire vehicle. The pitching moment coefficient is calculated based on the center of gravity by assuming uniform mass for the entire vehicle. The center of gravity is located about 57% of the body length from the cavitator. The positive value of the coefficient denotes nose up, and the negative one nose down. As mentioned above, the horizontal fins generate positive lift force in spite of zero AOA. Since the fins are located downstream from the center of gravity, the fins cause nose down moment. And the nose down moment caused by the horizontal fins is substantial in the transition state (where the cavity passes through the control fins) because the fins generate substantial positive lift force in this state as mentioned earlier. For the underwater vehicle, however, the effect of the horizontal fins on the pitching moment is insignificant, since the hydrodynamic force acting on the body is substantial compared with the force acting on the fins.

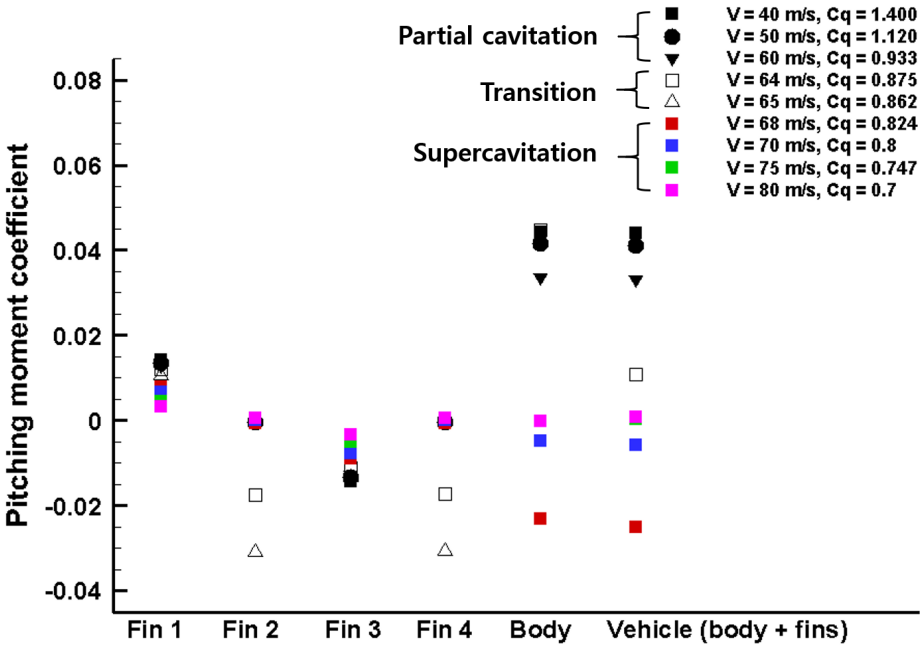

Figure 5.13: Pitching moment coefficients of the vehicle depending on the freestream velocities.

Table 5.4: Flow and ventilation conditions.

Freestream vel., V_∞	Air-entrainment coeff., C_Q	Angle of attack, α
65 m/s	0.40	0°
	0.80	
	0.86	
	1.00	
	1.50	
	2.00	

5.3 Effects of ventilation rate

Next, investigation on the effects of ventilation rate is presented. Computations of supercavitating flows around the vehicle are performed under various air-entrainment coefficients C_Q. The flow conditions are summarized in table 5.4. As in the case of freestream velocity, Fig. 5.14 shows that the cavity evolves from partial cavitation state to supercavitation state as the ventilation rate increases. As addressed in 5.2, the cavity behind the fins and the base is shortened as the cavity passes through the fins and the base (the after body). After achieving supercavitation state, the cavity length gradually increases with the ventilation rate.

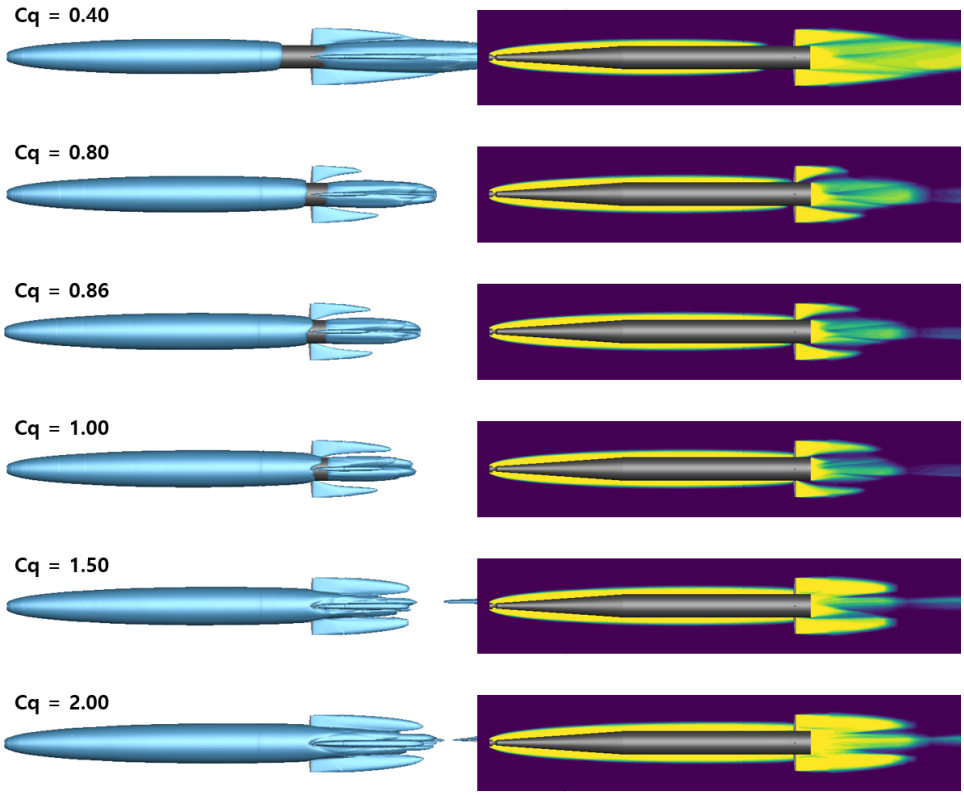

Figure 5.14: Cavity volume fraction under different ventilation rate ($V_\infty = 65$ m/s).

5.3.1 Hydrodynamic characteristics: drag

As discussed in 5.2.1, the drag coefficient of the control fins and the body decreases drastically when supercavitation is realized, as shonwn in Fig. 5.15. After achieving supercavitation, the drag coefficient gradually decreases as the cavity encloses a greater part of the fins and the body. The coefficient of the body gradually decreases as the cavity covers a greater part of the body surface. Due to the buoyant force, the cavity is shifted upward as mentioned above, covering a greater part of the fin 1 than that of fin 3. Thus, the fin 1 yields slightly lower drag coefficient than the fin 3, the lower vertical fin.

Figure 5.16 shows the drag behavior of the vehicle with different air-entrainment coefficients. Since the freestream velocity is maintained, the drag tends to decrease as the ventilation rate increases due to the change in enclosed area by the cavity. When the coefficient varies from 0.4 to 0.8, the fin drag (difference between the black and the red lines in Fig. 5.16) slightly increases since the locally high pressure region behind the cavity closure is in front of the control fins. As the coefficient increases further ($C_Q > 0.8$), the cavity encloses a part of the fins, decreasing the fin drag. As in the case of varying freestream velocity, the friction drag (difference between the red and the blue lines in Fig. 5.16) becomes insignificant since the body is contacted to the cavity (air), not water.

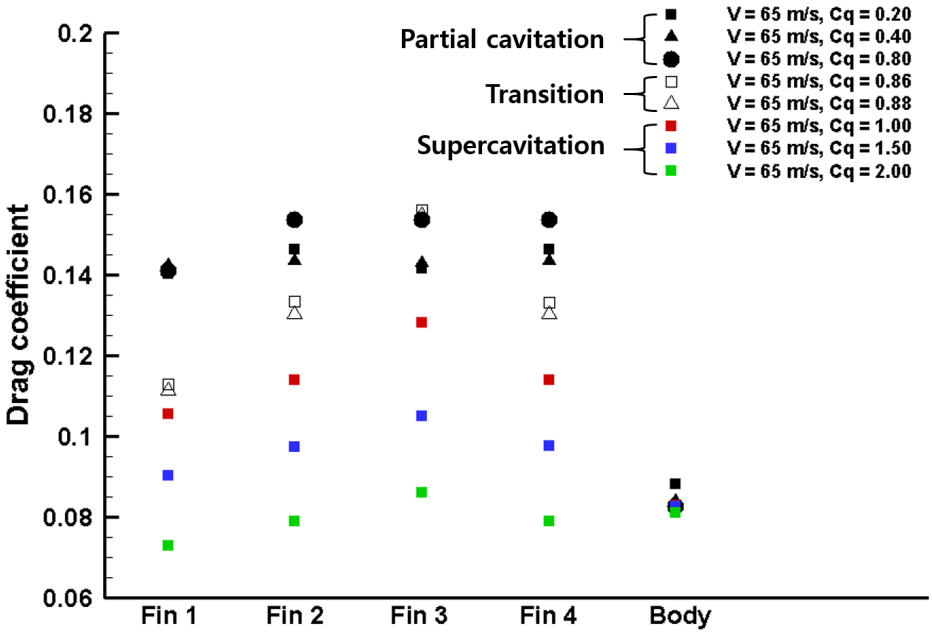

Figure 5.15: Drag coefficients of the control fins and the body depending on the ventilation rate.

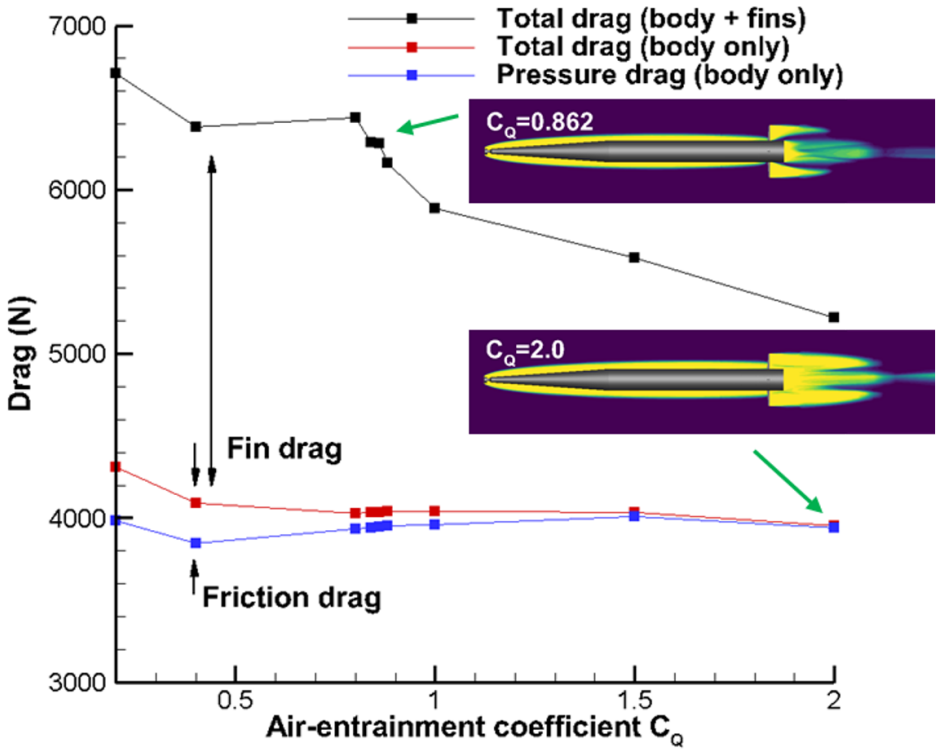

Figure 5.16: Drag force depending on the ventilation rate.

5.3.2 Hydrodynamic characteristics: lift

Figure 5.17 summarizes the lift coefficients of the control fins and the body under various ventilation rate. As mentioned earlier, the vertical fins generate the lift force in spite of zero angle of attack. For the partial cavitation state ($C_Q < 1.50$), the lift coefficient of the horizontal fins substantially increases as the cavity closure reaches the fins. After achieving the supercavitation state ($C_Q \geq 1.50$), the lift coefficient slightly and gradually decreases since the buoynat effect on the fins becomes weak due to the increased cavity length. Since the fins has taper ratio, even the vertical fins generate extremely weak lift force.

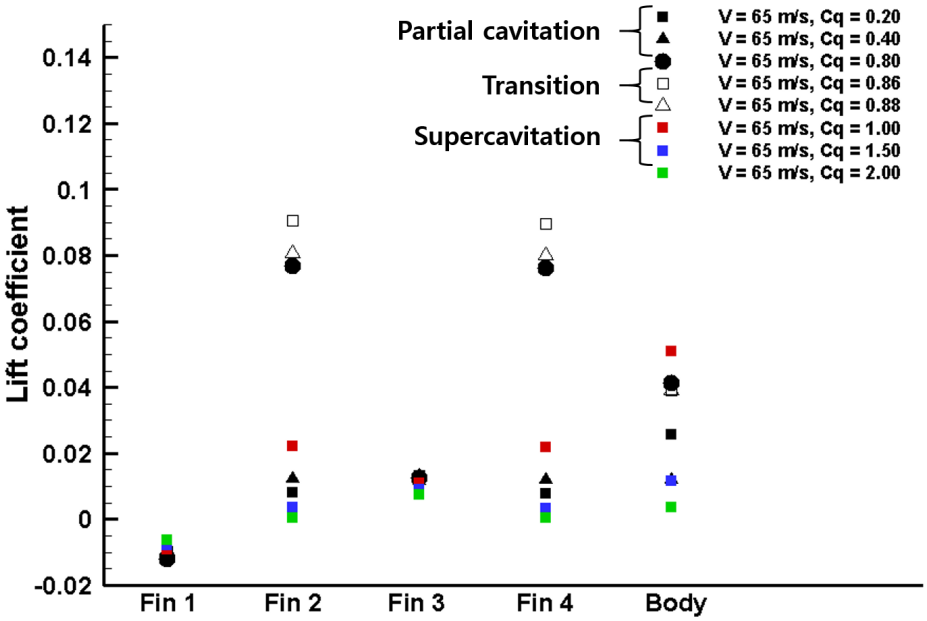

Figure 5.17: Lift coefficients of the control fins and the body depending on the ventilation rate.

5.3.3 Hydrodynamic characteristics: pitching moment

Figure 5.18 presents the pitching moment coefficient for different ventilation rates. Similar to the case of varying freestream velocity, the horizontal fins generate nose down moment due to the positive lift force acting on the fins. As the cavity passes through the after body (control fins and the base), the body causes substantial nose down moment since significant lift force is generated due to the asymmetric cavity closure near the base. In supercavitation state, the nose down moment gradually decreases (the value of the pitching moment increases because the nose down moment has negative value of the moment coefficient) with increasing ventilataion rate since the buoyancy effect on the lift force is weakened.

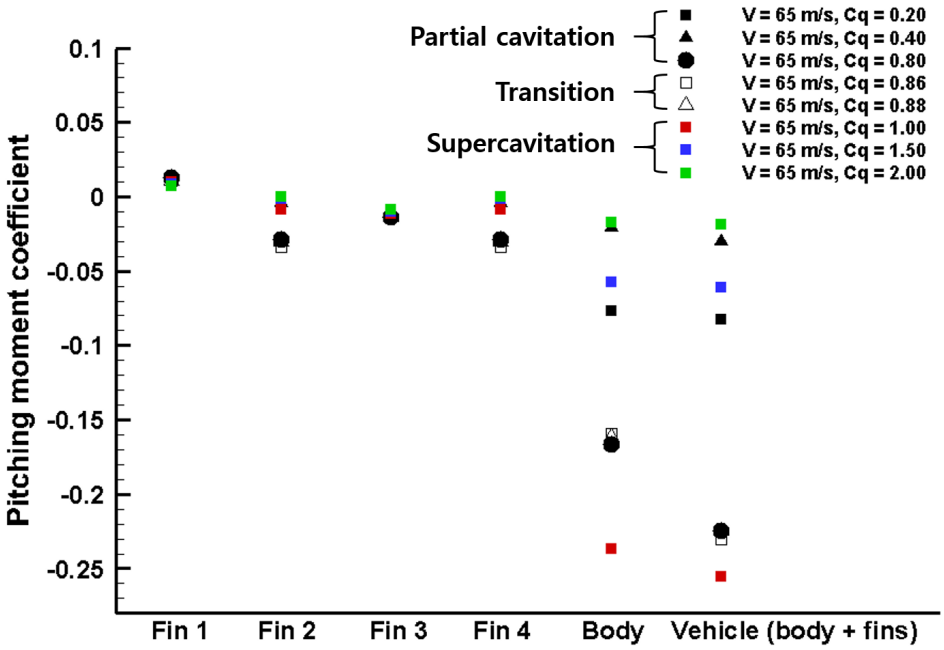

Figure 5.18: Pitching moment coefficients of the vehicle depending on the ventilation rate.

5.3.4 Unsteady hydrodynamic characteristics

Figures 5.19 and 5.20 show the cavities around the vehicle over time. As shown in the figure, no distinct flow unsteadiness is observed. However, Fig. 5.21 shows the lift coefficient oscillations of the horizontal fins and the vehicle body. Near the cavity closure, the local pressure increases and the pressure influences the horizontal fin, resulting in the substantial lift force, even zero angle of attack. Despite the indistinct change in the cavity shape, therefore, the lift force varies significantly (with amplitudes of 100 N for each horizontal fin and 300 N for the vehicle body) and periodically (about 20 Hz).

Next, we suppose a situation that an underwater vehicle injects substantial amount of gas to rapidly realize supercavitation state at relatively low speed. Figure 5.22 shows the evolution of supercavitation over time when the air-entrainment coefficient rapidly increases from 0.2 to 2.0. As the cavity evolve from the partial cavitation to supercavitation states, the two types of ventilated cavity (bifurcated and spoted cavities) can be clearly seen in Fig. 5.23. Figure 5.24 presents drag and lift forces acting on the control fins and the vehicle body over time. As shown in the figure, drastic changes in the forces observed. As shown in the figure, the total drag of all control fins accounts for about 37% of the vehicle drag when the drag is maxium (near 0.3 second). The Lift force substantially increases and then decreases (about 300 N for the horizontal fins and 2000 N for the vehicle body) for a very short time (less than 0.02 second). The results implies this drastic changes in hydrodynamic force for a very short time can lead to loss of controllability and/or structural damages. As shown in the results, the hydrodynamic forces acting on the control fins could be fatal when the vehicle is in the partial caviataion or transition (intermidiate state between partial cavitation and supercavitation) state. For this reason,

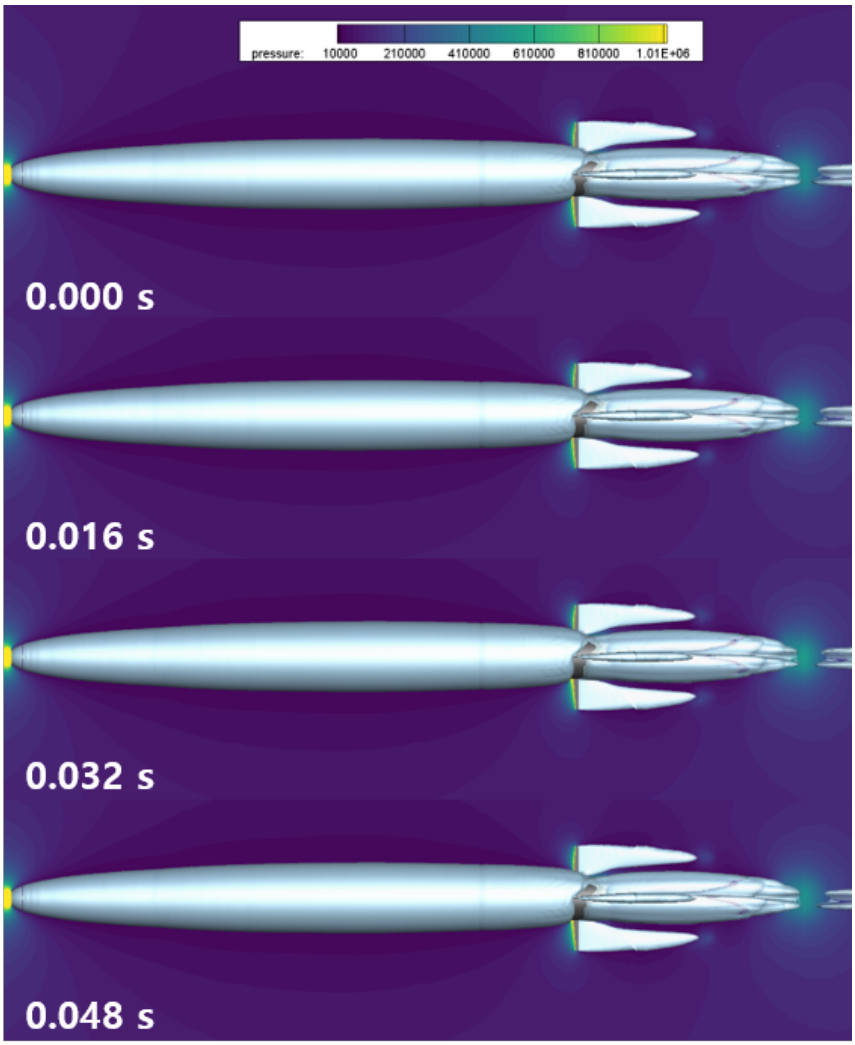

Figure 5.19: Cavities around the vehicle over time (C_Q=0.86)

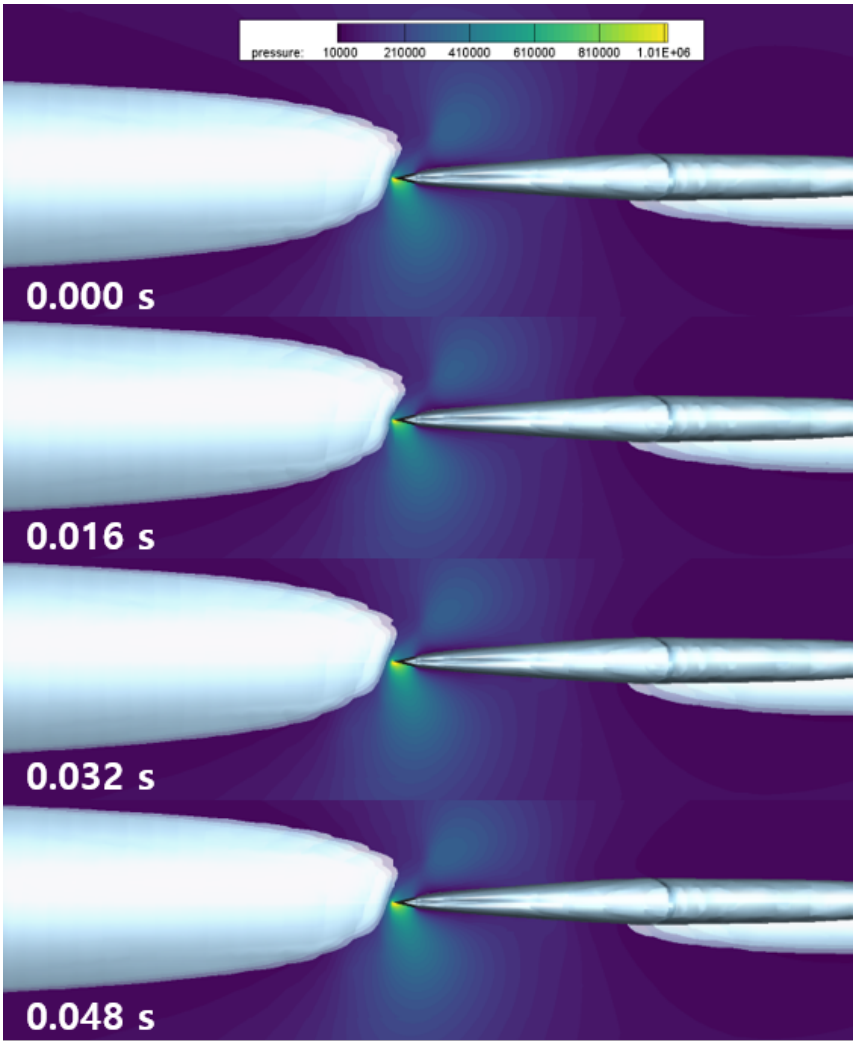

Figure 5.20: Cavities around a horizontal fin over time (C_Q=0.86)

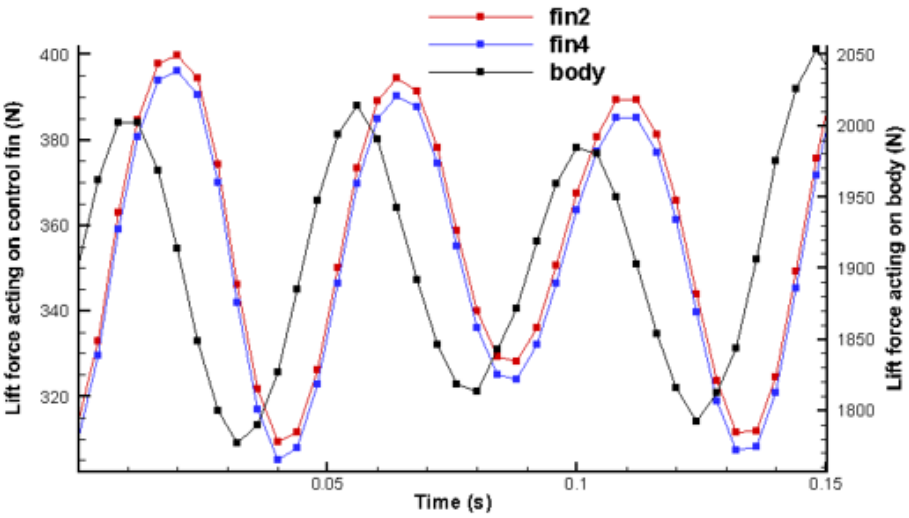

Figure 5.21: Oscillation of lift coefficient over time.

most of the underwater projectile launches with control fins embedded in the vehicle body, and unfolds the fins when the vehicle achieves supercavitation state. Also, design of a control fin (span, taper ratio, etc.) can also be essential for underwater vehicles.

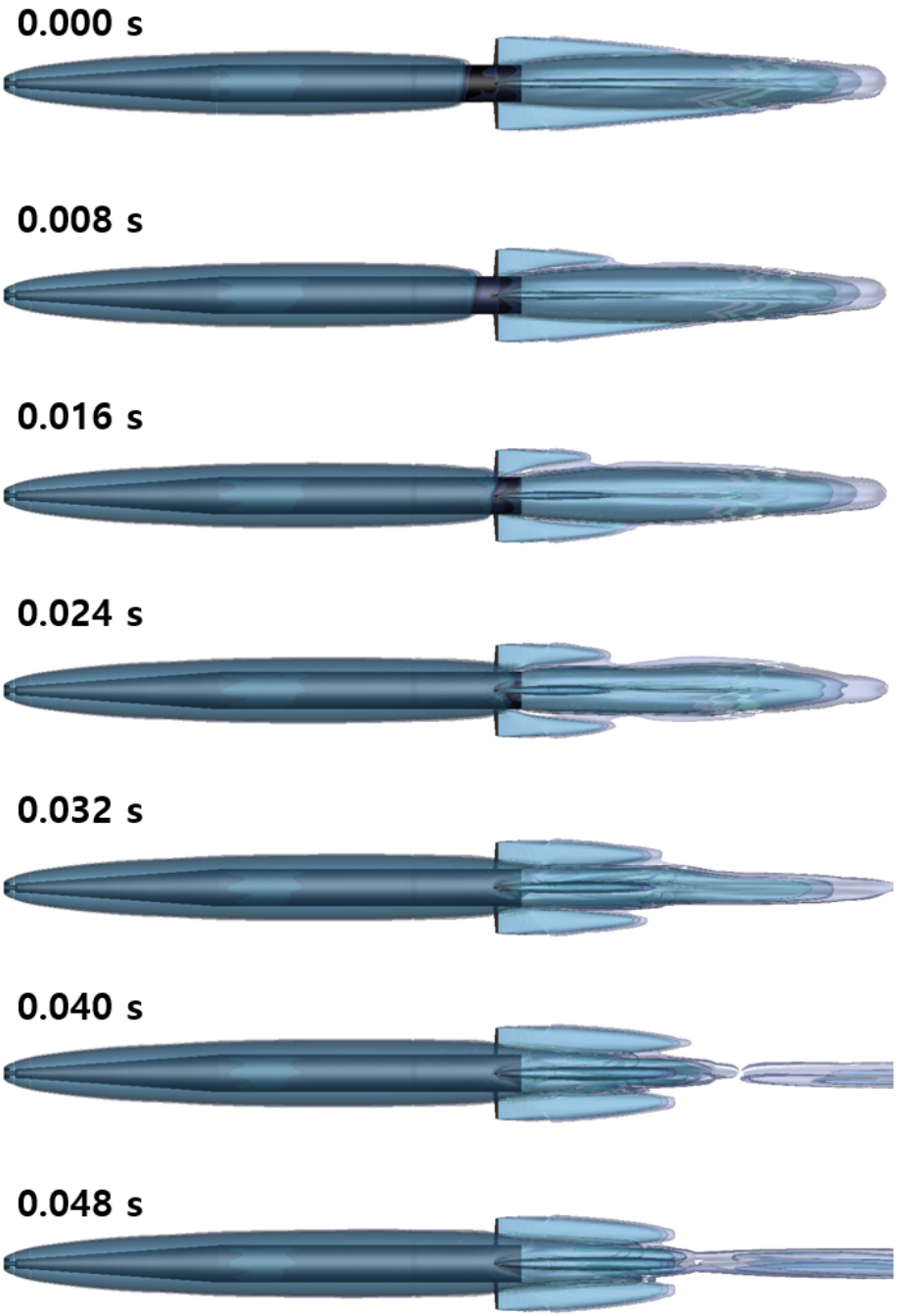

Figure 5.22: Evolution of supercavitation over time.

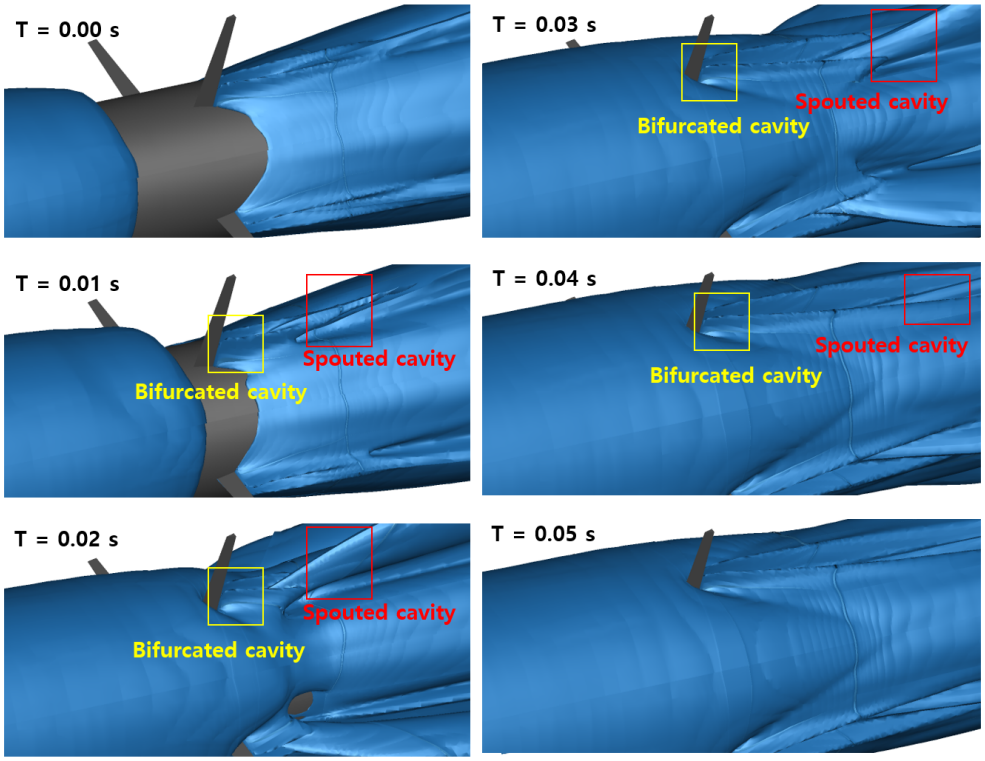

Figure 5.23: Evolution of ventilated cavity over time.

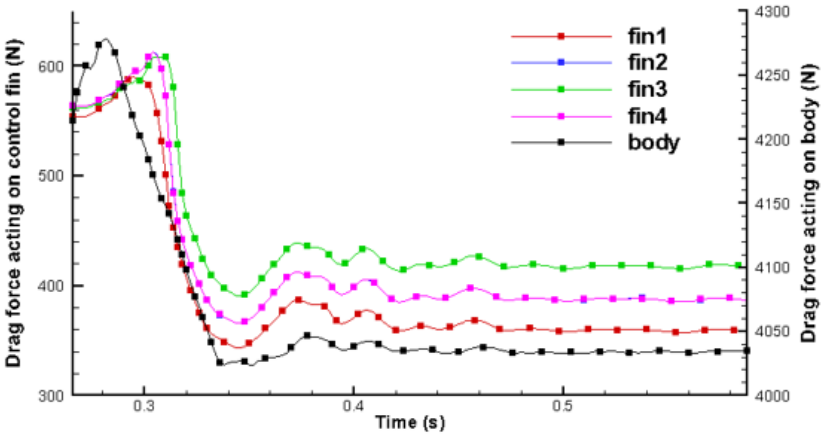

(a) Drag force

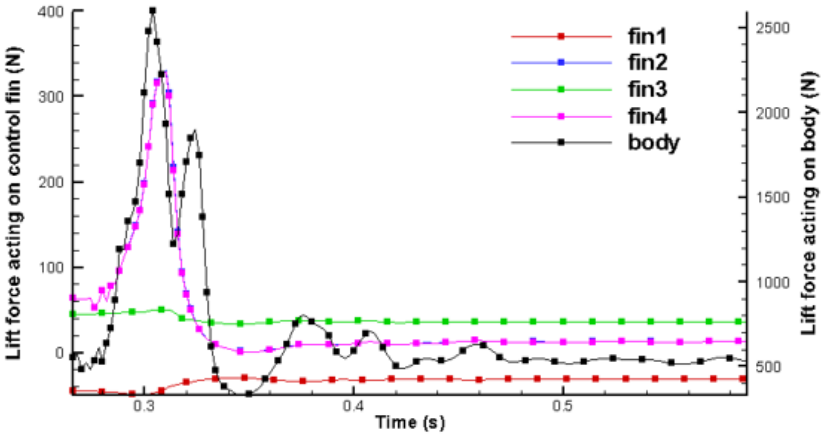

(b) Lift force

Figure 5.24: Drag and Lift forces acting on the control fins and the vehicle body.

5.4 Effects of attack angles

The effects of angle of attack are numerically investigated by conducting computations with AOA from 0° to 6° at $V_\infty = 70$ m/s. Figure 5.25 shows the cavities around the vehicle with different angles of attack. As shown in the figure, there is a drastic change in shape of the cavity for AOA $\geq 4°$. This a kind of transition in the cavity shape occurs since the cavity surrounds the maximum-diameter part of the body (AOA 1° - 3°) and the head part of the body (AOA 4° - 6°), as shown in Figs. 5.26 and 5.27.

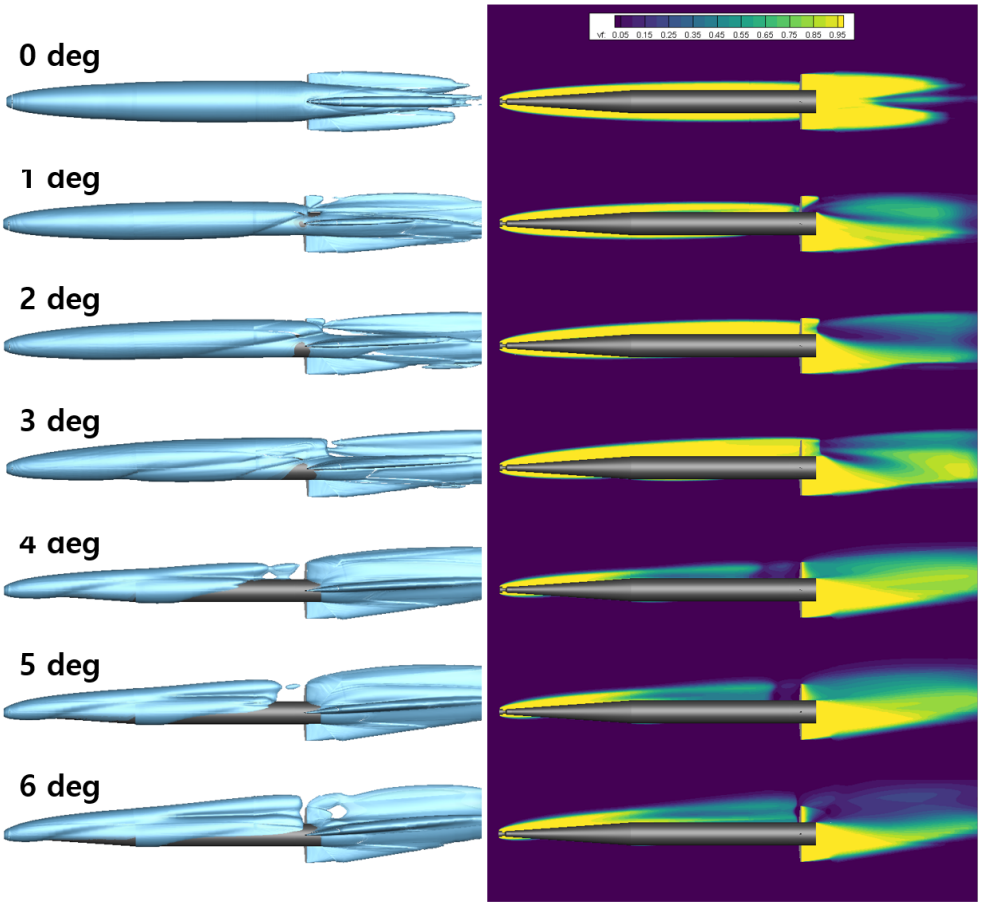

Figure 5.25: Supercavities around the vehicle with diefferent AOA (V_∞ = 70 m/s, C_Q=0.8).

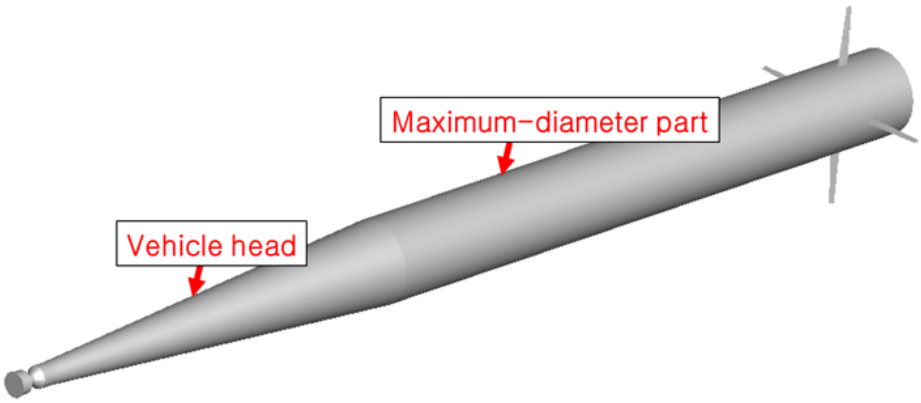

Figure 5.26: Head and body parts of the vehicle.

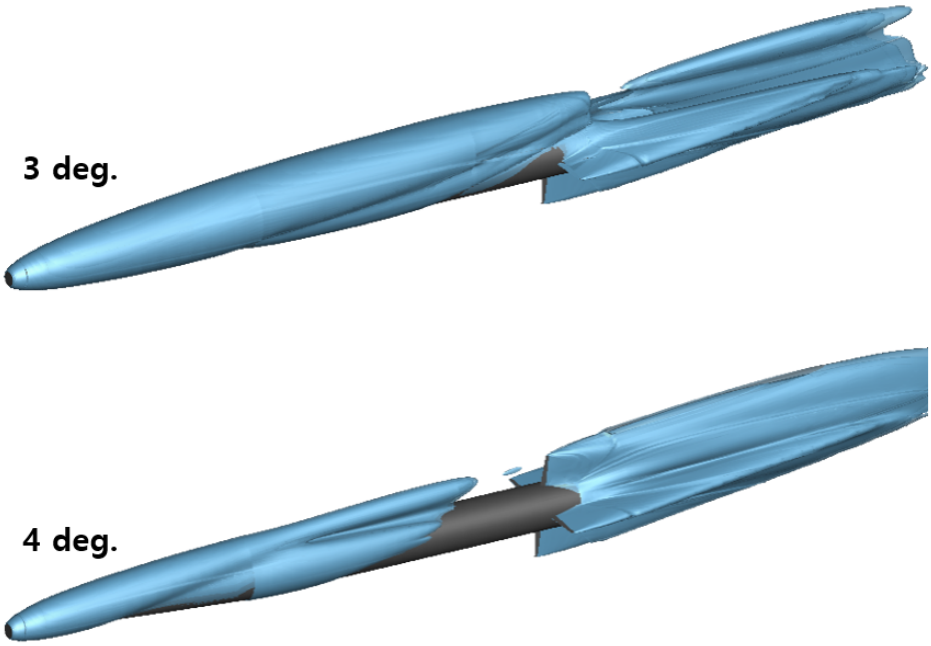

Figure 5.27: Transition of the cavity shape.

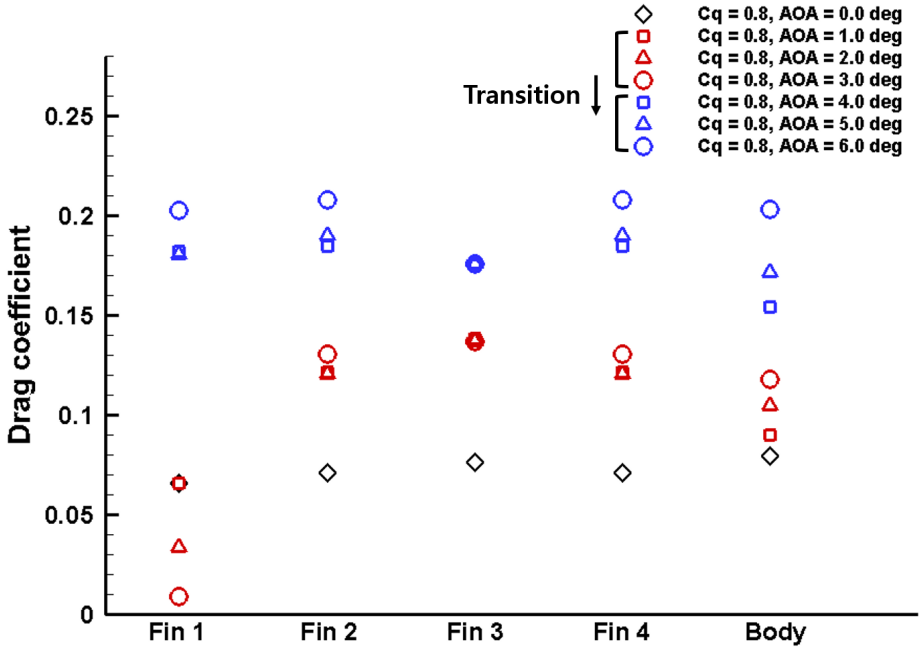

Figure 5.28: Drag coefficient with AOA.

5.4.1 Hydrodynamic characteristics: drag

Figure 5.28 shows the drag coefficient depending on the angles of attack. For the upper vertical fin (fin 1), the cavity covers a greater part of the fin as AOA increases, and thus the drag coefficient decreases. More than 3°, the cavity no longer covers the fin 1 and thus the drag coefficient drastically increases compared with the cases for AOA $\leq 3°$. For AOA $\geq 4°$, the cavity surrounds the head part as shown in Fig. 5.25, and a greater area of the vehicle body is exposed to water, not cavity (air). Moreover, a part of the head is also exposed to water, causing substantial drag as in Fig. 5.9. Hence, the drag coefficients drastically increase as the AOA changes from $3\leq 3°$ to $4\leq 3°$ (transition in cavity shape).

5.4.2 Hydrodynamic characteristics: lift

Figure 5.29 summarizes the lift coefficients with different AOA. The horizontal fins and the body generate substantial lift force with non-zero AOA. While the lift coefficnet increases drastically as the AOA changes from 0° to 1°, Fig. 5.29 shows that the increasing rate of the lift decreases for AOA $> 1°$. This situation results from natural cavitaties generated above and behind the horizontal fins, and is reported by many researchers [48, 49]. As mentioned earlier, vertical velocity component is induced by the cavity surrounding the vehicle body. For AOA $> 3°$, however, the effect of the induced velocity becomes insignificant since the cavity surrounds the head part as shown in Figs. 5.30 and 5.31. The local AOA in front of a horizontal fin is up to 10° as in Fig. 5.30b, but decreases up to 7° as in Fig. 5.31b although the freestream AOA increases from 3° to 4°. As a result, the lift coefficient decreases when AOA changes 3° to 4° and then gradually increases with AOA.

The results suggest that design of the head part is crusial for maneuverability of the vhicle. If the head length is too short, the drag acting on the head would be substantial since the normal velocity component of the impinging flow increases. But the maneuverability can be enhanced since the transition AOA (in the present result, between 3° and 4°) would increase. Therefore, proper shape of the head should be designed for both efficiency (low drag) and maneuverability. As the results in the previous sections, the non-linear features of hydrodynamic force are observed due to the characteristics of multi-phase flow. Again, the results confirm that the proper and accurate computation of the cavitating flow is necessary for predicting the vehicle's behavior.

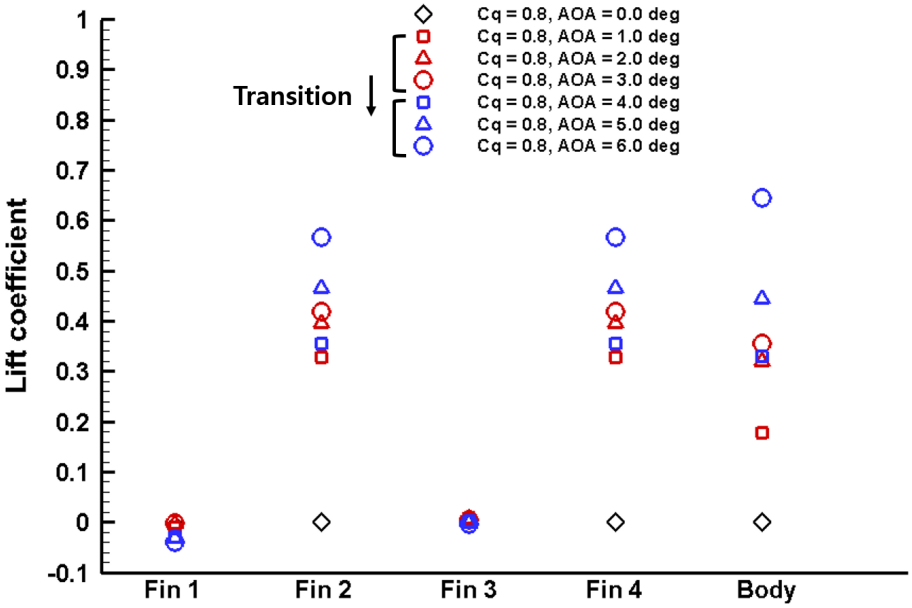

Figure 5.29: Drag coefficient with AOA.

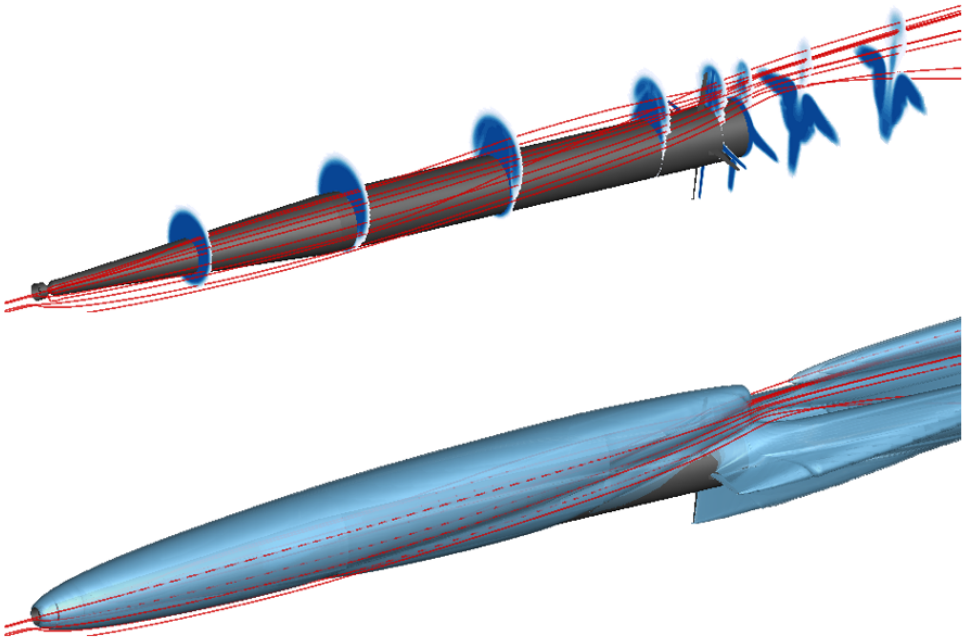

(a) Flow surrounding the vehicle

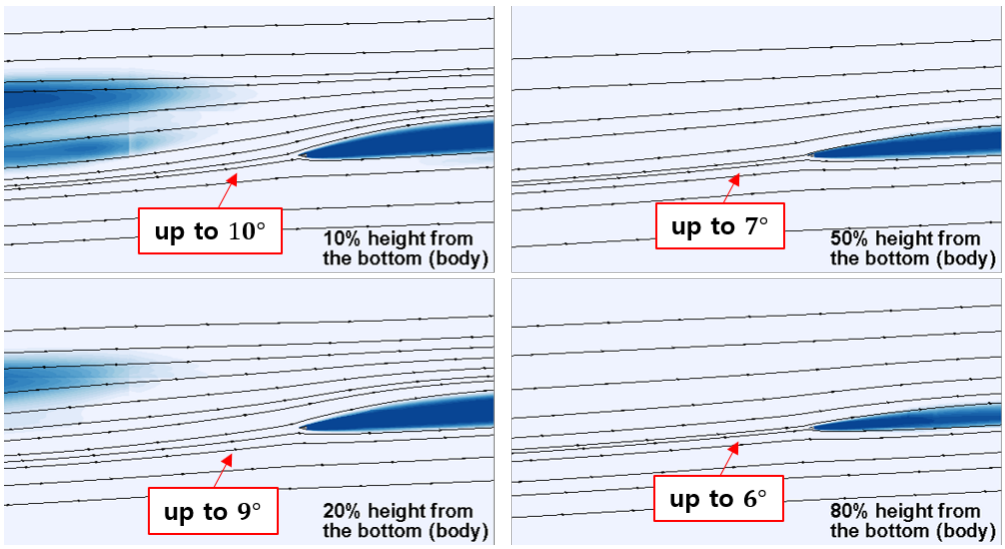

(b) Local flow directions for each height of the fin from the body.

Figure 5.30: Flow around the vehicle with streamlines (AOA = 3°).

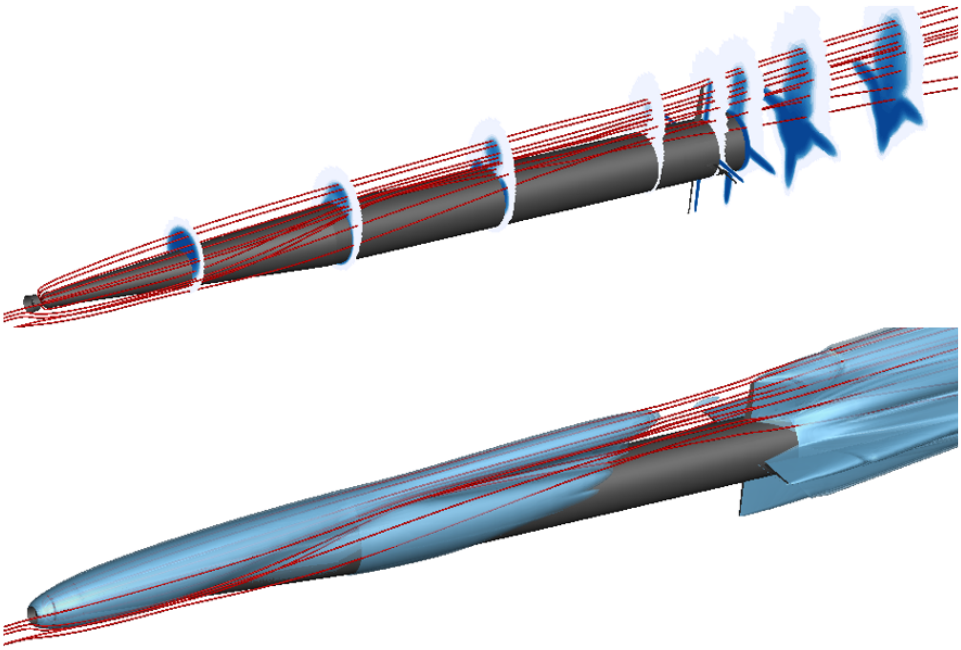

(a) Flow surrounding the vehicle

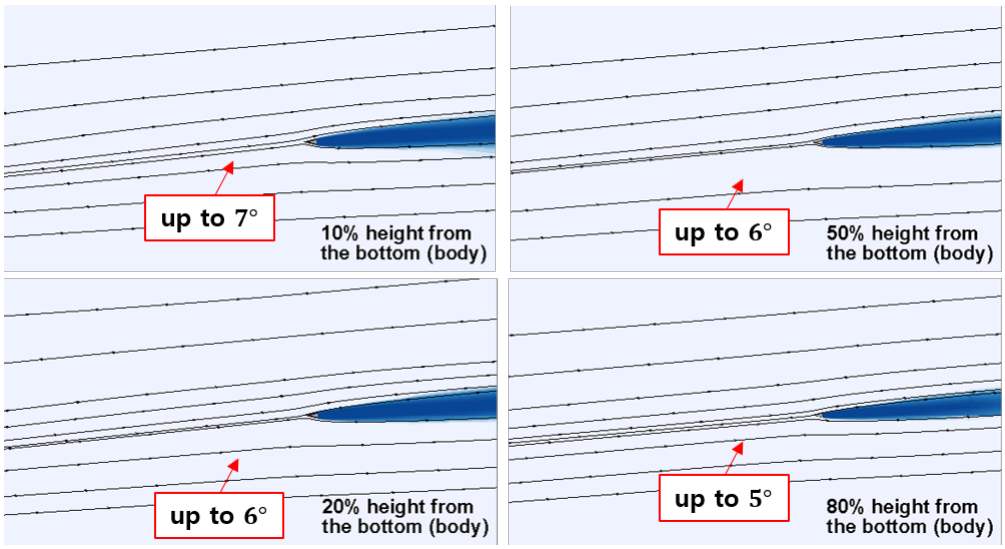

(b) Local flow directions for each height of the fin from the body.

Figure 5.31: Flow around the vehicle with streamlines (AOA = 4°).

5.4.3 Hydrodynamic characteristics: pitching moment

Figure 5.32 presents the pitching moment coefficient depending on the AOA. For AOA $\leq 3°$, the nose down moment (negative pitching moment) increases for both the horizontal fins and the body since the lift force acting on the after body increases with AOA. In the case of the vehicle body, the lift is mostly generated near the base for AOA $\leq 3°$ since the body part exposed to water is located near the base. For AOA $\geq 4°$ (After the transition in cavity shape), however, the pitching moment drastically increases and the nose up moment occurs except at AOA $= 6°$ for the entire vehicle. This is because the body part exposed to water is expanded to the head part located in front of the center of gravity. As the AOA increases further, the cavity moves downstream as shown in Fig. 5.25, causing the decreasing nose up moment. Although the lift force acting on the horizontal fins also moderate the nose up moment, the effect of the lift force is relatively insignificant compared with the body.

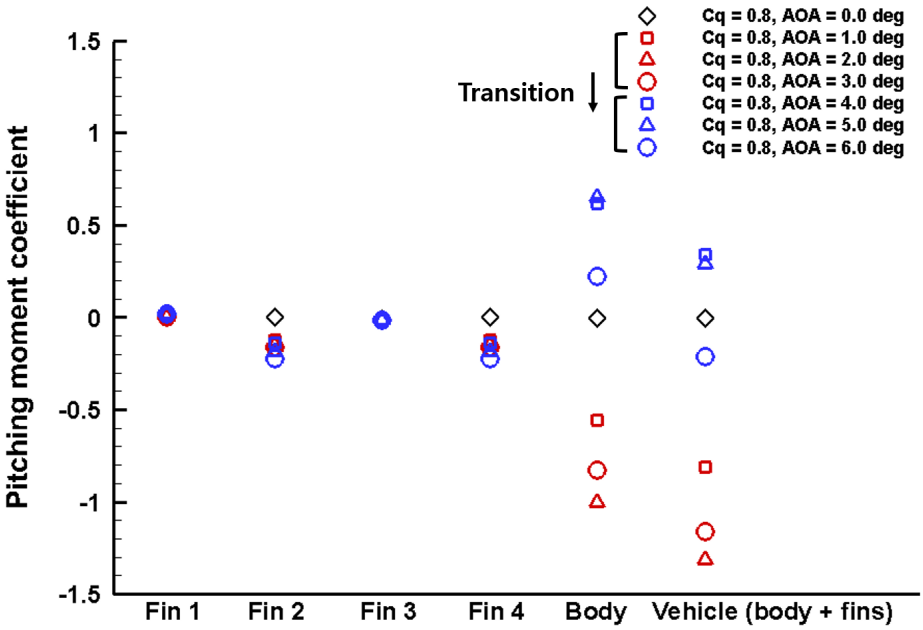

Figure 5.32: Pitching moment coefficients of the vehicle depending on the angle of attack.

Chapter 6

Conclusions

6.1 Summary

Numerical investigations on supercavitating flows around a high-speed underwater vehicle with control fins have been carried out under various conditions such as freestream velcotiy, ventilation rate, and angle of attack. Since the flow considered in this work consists of water, water vapor, and non-condensable air, we employ a homogeneous mixture model with mass fraction as the governing equations. The AUSMPW+_N and RoeM_N schemes are employed with proper system preconditioning for computations of multiphase flow at all speeds.

Firstly, we have conductd numerical simulation of experiments conducted by Chungnam National University Cavitation Tunnel (CNUCT) and Saint Anthony Falls Laboratory (SAFL) for validations of the flow solver used in this work. The former experiment deals with supercavitating flows around a cylindrical body connected with the cavitator. The computations are performed by altering the air-entrainment coefficient. The other experiment deals with

supercavitation in an unsteady gust flow. The geometric parameters of the supercaivty are compared between the computation and the experiment. All the computational results show good agreements with the experiments.

Next, we have carried out the 3-D computations of supercavitating flows around a high-speed underwater vehicle with control fin, and examine the hydrodynamic characteristics under various conditions such as freestream velocity (vehicle speed), air-entrainment coefficient (ventilation rate), and angle of attack. Overall computations suggest that the drag coefficient decrases as the freestream velocity and the ventilation rate increase, since the enlarged cavity encloses a greater part of the control fins and the vehicle body. Even though the angle of attack is zero, the horizontal fins generate lift force aided by buoyancy. As cavity evolves from subcavitation state to supercavitation state, the hydrodynamic forces change drastically in the transition state between the two states. The hydrodynamic behaviors are also influenced significantly with non-zero angle of attck. Particularly, when the cavity surrounds the head of the vehicle at high angle of attack, a sort of another transition occurs and the hydrodynamic coefficients change drastically.

We have also performed unstaedy computations of the cavitating flows around the vehicle. The results show that the lift force varies significantly (with amplitudes of 100 N for each horizontal fin and 300 N for the vehicle body) and periodically (about 20 Hz), although the cavity shows no distinct change in its shape. Also, as the cavity rapidly evolves from subcavitation to supercavitation state, the lift force substantially increases and then decreases (about 300 N for the horizontal fins and 2000 N for the vehicle body) for a very short time (less than 0.02 second) The results suggest that this drastic changes in hydrodynamic force for a very short time can lead to loss of controllability and/or structural damages.

All the results confirm that cavitating flows show non-linear features of the hydrodynamic forces. Hence, it is essential to understand and investigate supercavitating flows and hydrodynamic forces around an underwater vehicle for predicting the vehicle's behavior. The results provide some insight for the design of a supercavitating underwater vehicle, by substantially reducing the drag for safe acceleration at relatively low speed and securing controllability of a vehicle with the dataset of hydrodynamic forces.

6.2 Future works

Although this work covers extensive supercavitating flow physics and hydrodynamic characteristics, there is a room for further researches about detailed flow physics and dynamic characteristics of the vehicle.

At first, we conduct URANS simulation in this work for the supercavitating flows. However, the URANS simulations have significant limit in capturing vortex shedding characteristics. Recent researches [50, 51, 52] have reported that URANS equation cannot accurately predict the interation between turbulent vortex flow and cavitation. As addressed, control fins generate significant hydrodynamic forces when the cavity closure is close to the fins. Also, as shown in 5.3.4, the hydrodynamic forces can oscillate due to the cavity closure in front of the fin. The unsteady hydrodynamic characteristics can be explored more precisely with Detached Eddy Simulation (DES) or Large Eddy Simulation (LES). Therfore, this is one of the future works.

Another issue is the six degrees of freedom (6-DOF) analysis of the vehicle. In this work, we deal with supercavitating flows around an immovable vehicle. However, the vehicle moves as a result of the hydrodynamic forces acting on the control fins and the body. And this movement leads to a change of the local

flow conditions, such as freestream velcotiy (vehicle speed), angle of attack, and sideslip angle and so on. Particularly, when supercavitation is achieved, the vehicle is enclosed by the cavity. This causes the loss of buoyancy for the vehicle due to the lower fluid density than water. As a result, provided insufficient lift force by the horizontal fins, the vehicle falls due to the lack of buoyancy force and the supercavity is shifted upward due to the falling. Then, the vehicle is lifted up again when the aft body is contacted to water (planing force), and repeats this cycle. Hence, in order the examine the dynamic situation like this, we plan to conduct 6-DOF analyses based on the results from this work.

Bibliography

[1] S. L. Ceccio, "Friction Drag Reduction of External Flows with Bubble and Gas Injection," *Annu. Rev. Fluid Mech.*, vol. 42, pp. 183–203, 2010.

[2] M. W. Self and J. F. Ripken, "Steady-state cavity studies in a free-jet water tunnel," tech. rep., Saint Anthony Falls Hydraulic Laboratory, July 1955.

[3] C. S. Song, "Pulsation of Ventilated Cavities," tech. rep., Minneapolis, Minnesota, Feb. 1961.

[4] M. Wosnik, T. J. Schauer, and R. E. A. Arndt, "Experimental Study of a Ventilated Supercavitating Vehicle," in *CAV2003*, (Osaka, Japan), Aug. 2003.

[5] A. Karn and B. Rosiejka, "Air entrainment characteristics of artificial supercavities for free and constrained closure models," *Experimental Thermal and Fluid Science*, vol. 81, pp. 364–369, 2017.

[6] S. Shao, A. Karn, B.-K. Ahn, R. E. A. Arndt, and J. Hong, "A Comparative Study of Natural and Ventilated Supercavitation Across two Closed-Wall Water Tunnel Facilities," *Experimental Thermal and Fluid Science*, vol. 88, pp. 519–529, 2017.

[7] B.-K. Ahn, S.-W. Jeong, J.-H. Kim, S. Shao, J. Hong, and R. E. A. Arndt, "An Experimental Investigation of Artificial Supercavitation Generetaed by Air Injection Behind Disk-Shaped Cavitators," *International Journal of Naval Architecture and Ocean Engineering*, vol. 9, pp. 227–237, 2017.

[8] T. Liu, B. Huang, G. Wang, M. Zhang, and D. Gao, "Experimental investigation of the flow pattern for ventilated partial cavitating flows with effect of Froude number and gas entrainment," *Ocean Engineering*, vol. 129, pp. 343–351, 2017.

[9] J. Chung and Y. Cho, "Ventilated supercavitation around a moving body in a still fluid: observation and drag measurement," *Journal of Fluid Mechanics*, vol. 854, pp. 367–419, 2018.

[10] P. R. Garabedian, "Clculation of Axially Symmetric Cavities and Jets," *Pacific J. Math*, vol. 6, pp. 611–684, 1956.

[11] I. J. Campbell and D. V. Hilborne, "Air Entrainment Behind Artificially Inflated Cavities," in *The Second Symposium on Cavitation on Naval Hydrodynamics*, (Washington, USA), Aug. 1958.

[12] J. H. Kim and B. K. Ahn, "Numerical analysis of supercavitating flow around axisymmetric underwater objects using a viscous-potential method," *J Mar Sci Technol*, vol. 23, pp. 364–377, 2018.

[13] R. F. Kunz, D. A. Boger, T. S. Chyczewski, D. R. Stinebring, H. J. Gibeling, and T. R. Govindan, "Multi-phase CFD analysis of natural and ventilated cavitation about submerged bodies," in *FEDSM99*, (SF, California), July 1999.

[14] R. F. Kunz, J. W. Lindau, M. L. Billet, and D. R. Stinebring, "Multiphase CFD Modeling of Developed and Supercavitating Flows," tech. rep., University Park, PA, Feb. 2001.

[15] M. P. Kinzel, J. W. Lindau, and R. F. Kunz, "Air Entrainment Mechanisms from Artificial Supercavities: Insight based on numerical," in *CAV2009*, (Michigan, USA), Aug. 2009.

[16] I. Rashidi, M. P. Fard, M. P. Fard, and N. M. Nouri, "Numerical and Experimental Study of a Ventilated Supercavitating Vehicle," *Journal of Fluid Engineering*, vol. 136, p. 101301, 2014.

[17] I. N. Kirschner, D. C. Kring, A. W. Stokes, N. E. Fine, and J. S. Uhlman Jr, "Control Strategies for Supercavitating Vehicles," *Journal of Vibration and Control*, vol. 8, pp. 219–242, 2002.

[18] K.-p. Yu, G. Zhang, J.-j. Zhou, W. Zou, and Z.-w. Li, "Numerical Study of the Pitching Motions of Supercavitating Vehilces," *Journal of Hydrodynamics, Ser. B*, vol. 24, pp. 951–958, 2012.

[19] W. Zou, K.-p. Yu, and R. E. A. Arndt, "Modeling and Simulations of Supercavitating Vehicle with Planing Force in the Longitudinal Plane," *Applied Mathematical Modelling*, vol. 39, pp. 6008–6020, 2015.

[20] X. Yuan and T. Xing, "Hydrodynamic Characteristics of a Supercavitating Vehicle's aft body," *Ocean Engineering*, vol. 114, pp. 37–46, 2016.

[21] L. Cao, A. Karn, R. E. A. Arndt, Z. Wang, and J. Hong, "Numerical Investigations of Pressure Distribution Inside a Ventilated Supercavity," *Journal of Fluid Engineering*, vol. 139, pp. 1–8, 2017.

[22] W. Zou, L. Xue, B. Wang, and X. Xintao, "Gas Flows and Losses Inside High-Speed Ventilated Supercavitating Flows," *Ocean Engineering*, vol. 164, pp. 65–73, 2018.

[23] H.-T. Kim, E.-J. Choi, K.-T. Kang, and H.-G. Yoon, "Numerical Anlaysis of the Cavitation Around an Underwater Body with Control Fins," *Journal of the Society of Naval Architects of Korea*, vol. 56, pp. 298–307, 2019.

[24] H. Kim, H. Kim, and C. Kim, "Computations of Homogeneous Multiphase Real Fluid Flows at All Speeds," *AIAA Journal*, vol. 56, pp. 2623–2634, 2018.

[25] F. H. Harlow and A. A. Amsden, "Fluid Dynamics: A LASL Monograph," tech. rep., Los Alamos, New Mexico, Feb. 1971.

[26] W. Wagner, J. R. Cooper, A. Dittmann, J. Kijima, H. J. Kretzschmar, A. Kruse, R. Mareš, K. Oguchi, H. Sato, I. Stöcker, O. S. ifner, Y. Takaishi, I. Tanishita, J. Trübenbach, and T. Willkommen, "The IAPWS Industrial Formulation 1997 for the Thermodynamic Properties of Water and Steam," *Journal of Engineering for Gas Turbines and Power*, vol. 122, no. 1, pp. 150–184, 2000.

[27] J. Kestin, J. V. Sengers, B. Kamgar-Parsi, and J. M. H. L. Sengers, "Thermophysical Properties of Fluid H2O," *Journal of Physical and Chemical Reference Data*, vol. 13, no. 1, p. 175, 1984.

[28] C. L. Merkle, J. Z. Feng, and P. E. O. Buelow, "Computational modeling of the dynamics of sheet cavitation," in *3rd International Symposium on Cavitation*, (Grenoble, France), 1998.

[29] F. R. Menter, "Two-Equation Eddy-Viscosity Turbulence Models for Engineering Applications," *AIAA Journal*, vol. 32, no. 8, pp. 1598–1605, 1994.

[30] F. R. Menter, M. Kuntz, and R. Langtry, "Ten Years of Industrial Experience with the SST Turbulence Model," *Turbulence, Heat and Mass Transfer 4*, pp. 625–632, 2003.

[31] D. C. Wilcox, "Reassessment of the scale-determining equation for advanced turbulence models," *AIAA Journal*, vol. 26, pp. 1299–1310, Nov. 1988.

[32] F. R. Menter, "Influence of freestream values on k-omega turbulence model predictions," *AIAA Journal*, vol. 30, pp. 1657–1659, June 1992.

[33] J. M. Weiss and W. A. Smith, "Preconditioning applied to variable and constant density flows," *AIAA Journal*, vol. 33, no. 11, pp. 2050–2057, 1995.

[34] S. Venkateswaran and C. L. Merkle, "Dual time-stepping and preconditioning for unsteady computations," in *33rd Aerospace Sciences Meeting and Exhibit, Aerospace Sciences Meetings*, (Reno, Nevada), American Institute of Aeronautics and Astronautics, Jan. 1995.

[35] S.-W. Ihm and C. Kim, "Computations of Homogeneous-Equilibrium Two-phase Flows with Accurate and Efficient Shock-Stable Schemes," *AIAA Journal*, vol. 46, no. 12, pp. 3012–3037, 2008.

[36] J. R. Edwards and M.-S. Liou, "Low-Diffusion Flux-Splitting Methods for Flows at All Speeds," *AIAA Journal*, vol. 36, no. 9, pp. 1610–1617, 1998.

[37] H. Luo, J. D. Baum, and R. Lohner, "Extension of Harten-Lax-van Leer Scheme for Flows at All Speeds," *AIAA Journal*, vol. 43, no. 6, pp. 1160–1166, 2005.

[38] M. A. Potsdam, V. Sankaran, and S. A. Pandya, "Unsteady Low Mach Preconditioning with Application to Rotorcraft Flows," in *18th AIAA Computational Fluid Dynamics Conference, Fluid Dynamics and Co-located Conferences*, (Miami, Florida), American Institute of Aeronautics and Astronautics, June 2007.

[39] J. Sachdev, A. Hosangadi, and V. Sankaran, "Improved Flux Formulations for Unsteady Low Mach Number Flows," in *42nd AIAA Fluid Dynamics Conference and Exhibit, Fluid Dynamics and Co-located Conferences*, (New Orleans, Louisiana), American Institute of Aeronautics and Astronautics, June 2012.

[40] A. J. Katz, D. Folkner, and V. Sankaran, "An Unsteady Preconditioning Scheme Based on Convective-Upwind Split-Pressure (CUSP) Artificial Dissipation," in *52nd Aerospace Sciences Meeting, AIAA SciTech*, (National Harbor, Maryland), American Institute of Aeronautics and Astronautics, Jan. 2014.

[41] M.-S. Liou, "A sequel to AUSM, Part II: AUSM+-up for all speeds," *Journal of Computational Physics*, vol. 214, no. 1, pp. 137–170, 2006.

[42] K. H. Kim and C. Kim, "Accurate, efficient and monotonic numerical methods for multi-dimensional compressible flows: Part II: Multi-dimensional limiting process," *Journal of Computational Physics*, vol. 208, no. 2, pp. 570–615, 2005.

[43] S.-H. Yoon, C. Kim, and K. H. Kim, "Multi-dimensional limiting process for three-dimensional flow physics analyses," *Journal of Computational Physics*, vol. 227, no. 12, pp. 6001–6043, 2008.

[44] B.-K. Ahn, S.-W. Jeong, J.-H. Kim, S. Shao, A. Karn, J. Hong, and R. E. A. Arndt, "An Experimental Investigation of Artificial Supercavitation," in *31st Symposium on Naval Hydrodynamics*, (Montery, California), 2016.

[45] S. Shao, Y. Wu, J. Haynes, R. E. A. Arndt, and J. Hong, "Investigation into the Behaviors of Ventilated Supercavities in Unsteady Flow," *Physics of Fluids*, vol. 30, pp. 1–11, 2018.

[46] R. Huang, S. Shao, R. E. A. Arndt, X. Luo, Y. Wang, and J. Hong, "Numerical Study of the Behaviors of Ventilated Supercavities in a Periodic Gust Flow," *Journal of Fluids Engineering*, vol. 142, pp. 1–15, 2020.

[47] S.-J. Lee, E. Kawakami, and R. E. A. Arndt, "Investigation of the Behavior of Ventilated Supercavities in a Periodic Gust Flow," *Journal of Fluids Enginnering*, vol. 135, p. 081301, 2013.

[48] R. W. Kermeen, "Experimental Investigations of Three-Dimensional Effects on Cavitating Hydrofoils," in *Technology Report*, (Pasadena, CA), California Institute of Technology, 1960.

[49] G. Vernengo, L. Bonfiglio, and S. Brizzolara, "Supercavitating Three-Dimensional Hydrofoil Analysis by Viscous Lifting-Line Approach," *AIAA Journal*, vol. 55, pp. 4127–4141, 2017.

[50] R. F. Kunz, J. W. Lindau, T. A. Kaday, and L. J. Peltier, "Unsteady Rans and Detached Eddy Simulations of Cavitating Flow over a Hydrofoil," in

Fifth International Symposium on Cavitation (CAV2003), (Osaka, Japan), Nov. 2003.

[51] B. Huang, Y. Zhao, and G. Wang, "Large Eddy Simulation of Turbulent Vortex-Cavitation Interactions in Transient Sheet/Cloud Cavitating Flows," *Computers & Fluids*, vol. 92, pp. 113–124, 2014.

[52] M. Liu, L. Tan, and S. Cao, "Cavitation-Vortex-Turbulence Interaction and One-Dimensional Model Prediction of Pressure for Hydrofoil ALE15 by Large Eddy Simulation," *Journal of Fluids Engineering*, vol. 141, p. 021103, 2019.

초록

본 논문은 네 개의 제어판이 부착된 고속 수중운동체 주변의 정상/비정상 공동 유동을 수치적으로 해석하고, 수중운동체에 작용하는 유체력을 분석하는 연구를 다루고 있다. 본 연구에서 다루고자 하는 초공동 유동은 물과 증기, 그리고 비응축 기체인 공기로 이루어진 다상유동이며, 이를 해석할 수 있도록 균질혼합류 모델(Homogeneous mixture model)을 기반으로 한 URANS(Unsteady Reynolds Averaged Navier-Stokes) 방정식을 지배방정식으로 하여 수치해석을 수행하였다.

본 연구에 사용한 수치해석자의 검증을 위해 우선 충남대학교에서 수행된 분사공동 실험을 수치적으로 해석하여 이를 실험과 비교 및 검증하였다. 다음으로 Minnesota 대학에서 수행된 비정상 돌풍유동에서의 공동현상 실험을 수치적으로 해석하여 이 또한 실험 결과와 비교 및 검증하였다.

다음으로 3차원 수중운동체 주변의 정상/비정상 분사 초공동 유동에 대한 유동해석을 수행하였다. 수중운동체 주변의 공동유동 변화에 따라 동체 및 제어판에 작용하는 양력, 항력 및 피칭 모멘트가 어떠한 영향을 받는지를 분석하기 위해 전방류 유속, 분사유량, 동체 받음각 등을 변화시켜가며 수중운동체 주변의 초공동 유동해석을 수행하였다. 해석 결과 유동조건 변화에 따라 수중운동체 및 제어판에 작용하는 유체력이 복잡한 비선형성을 갖는 것을 확인하였으며, 이로 인해 단상유동을 가정했을 때 예상할 수 있던 유체력 결과와 상이한 결과를 확인할 수 있었다.

주요어: 서울대학교, 기계항공공학부, 졸업논문

학번: 2014-30359